University Library

MINERVA ACCESS

A gateway to Melbourne's research publications

Minerva Access is the Institutional Repository of The University of Melbourne

Author/s:
Di, Hongzhan

Title:
A fundamental study of membrane fouling using a novel microfluidic filtration system

Date:
2018

Persistent Link:
https://hdl.handle.net/11343/216171

Terms and Conditions:
Terms and Conditions: Copyright in works deposited in Minerva Access is retained by the copyright owner. The work may not be altered without permission from the copyright owner. Readers may only download, print and save electronic copies of whole works for their own personal non-commercial use. Any use that exceeds these limits requires permission from the copyright owner. Attribution is essential when quoting or paraphrasing from these works.

A Fundamental Study of Membrane Fouling using A Novel Microfluidic Filtration System

Hongzhan Di

Submitted in total fulfilment of the requirements of

the degree of

Doctor of Philosophy

Department of Chemical and Biomolecular Engineering

The University of Melbourne

February 2018

Copyright © 2018 Hongzhan Di

All rights reserved. No part of the publication may be reproduced in any form by print, photoprint, microfilm or any other means without written permission from the author.

Declaration

This is to certify that

1. The thesis comprises only my original work towards the PhD;
2. Due acknowledgement has been made in the text to all other material used;
3. The thesis is less than 100,000 words in length, exclusive of tables, figures, bibliographies and appendices.

Acknowledgement

I would like to express my sincerest gratitude to my supervisors, Prof. Dave Dunstan and Dr. Greg Martin. I appreciate all their contributions of time, supervisions, ideas, and funding to make my Ph.D. experience productive and stimulating. I would also like to thank my committee chair, Prof. Ray Dagastine, for his valuable comments and suggestions on the research.

I gratefully acknowledge the funding sources that made my Ph.D. work possible, Melbourne Interactional Research Scholarship and Melbourne International Fee Remission Scholarship issued from the University of Melbourne Scholarship Office.

This work was performed in part at the Melbourne Centre for Nanofabrication (MCN) in the Victorian Node of the Australian National Fabrication Facility (ANFF). My sincere thanks go to Mr. Dan Smith, Dr. John Zhou, and Dr. Ricky Tueng who provided me lots of support on the development of microfluidic system.

My thanks also go to my research fellows, Dr. Dylan Liu, Dr. Donglin, Xie, Dr. Firoozeh Babayekhorasani and Mr. Kenneth Ng, for their kind help and support in my Ph.D. research work. My time at Melbourne was made enjoyable in part due to my housemates and friends, with whom I spent memorable time traveling around Australia.

Lastly, I would like to especially thank my parents and my brother. They have cherished with me every great moment and supported me in all my pursuits throughout my life. Their unconditional love and support is more than I can express in words. Thank you.

Abstract

Membrane filtration has been widely employed in dairy manufacturing, wastewater treatment, and beverage clarification. However, the issue of membrane fouling significantly reduces the filtration performance by increasing the capital and operating costs. The mechanisms of membrane fouling during filtration processes are yet to be fully understood. This thesis details the development and application of a novel microfluidic filtration system for directly visualising and measuring membrane fouling. Detailed, real-time characterisations of particle deposition during crossflow filtration have been examined over a range of solution properties and operating conditions. An empirical model considering both effects of interactions and hydrodynamics has been developed for describing the dynamic deposition behaviour.

This thesis comprises three main sections of work. First is a description of the development of a novel microfluidic filtration system for studying membrane fouling. The system incorporates microfluidics, confocal microscopy, and a dual syringe flow control setup. Time-resolved, high-resolution images of particles on the membrane surface and three-dimensional images of the filtration channel can be obtained. The effectiveness of the system was demonstrated by using model particles. Analysis of images obtained from the system, enabled the particle deposition behaviour to be described in relation to dynamic surface coverage and particle deposition volume.

Secondly, the effect of solution properties on membrane fouling has been studied in order to assess the effect of the key fundamental physical parameters on membrane fouling. Detailed, real-time deposition processes during crossflow filtration of 0.4 μm model particles was investigated in relation to variations in pH, ionic strength, and particle feed concentration. The detailed structures and distributions of the deposited layer were reported. Experimental results were interpreted using DLVO theory, Van der Waals attraction energy, and a modified Hogg-Healy-Fuersteneau (HHF) formula combined to account for the interplay between membrane-particle interactions and particle-particle interactions to understand the overall deposition behaviour. Overall, solution properties significantly influence the dynamic deposition process. The initial deposition behaviour was primarily governed by membrane-particle interactions, while long-term deposition was largely determined by particle-particle interactions.

Thirdly, the role of operating conditions on membrane fouling during crossflow filtration was investigated by varying permeate flux/velocity and crossflow velocity. Their influence on membrane fouling was characterized by the deposition probability, which can be determined from hydrodynamic forces exerted on particles in the crossflow. Building on the experimental results obtained from various solution properties and operating conditions, an empirical correlation was developed for describing the dynamic deposition volume in terms of interaction energies,

deposition probability, and filtration time. Greater amount of deposition was observed with greater permeate flux and lower crossflow velocity. A critical crossflow velocity was observed, over which, particle deposition significantly decreased as velocity increased. A correlation between the deposition behaviour and both the solution properties and operating conditions was developed.

In conclusion, the novel microfluidic filtration system developed in this work, is used in a comprehensive experimental program to provide detailed measurements of membrane fouling over a range of solution properties and operating conditions that revealed new insights into particle deposition. The overall deposition behaviour is found to be governed by the fundamental interactions of membrane-particle and particle-particle (primarily influenced by varying pH and ionic strength), and hydrodynamic forces acting on particles (primarily influenced by varying crossflow velocity and permeate flux). Membrane-particle interactions had more impact on the initial deposition behaviour, since for short-time filtration, particles directly deposit on the membrane surface. As filtration time increased, the membrane surface occupied by deposited particles increases. New arriving particles tent to deposit on the already-deposited-particles, thus particle-particle interactions affected the long-term deposition behaviour. The influence of hydrodynamic forces on particle deposition is characterized by the deposition probability. An empirical correlation was developed and the predictions shown to be in good experimental results. It has been the first time for a correlation to describe the dynamic deposition behaviour integrating both the influence of interaction energies and hydrodynamic forces, which can be used for setting up filtration parameters and better predicting the fouling process over a range of conditions.

Research Outputs

CHAPTER 2

"Literature review of microstructural measurements of membrane fouling during filtration processes"

Manuscript in preparation for submission to a membrane science journal.

Hongzhan Di, Gregory J. O. Martin, Dave E. Dunstan*

CHAPTER 3

"A microfluidic system for studying particle deposition during ultrafiltration"

Published in the Journal of Membrane Science 532 (2017) 68–75

Hongzhan Di, Gregory J. O. Martin, Dave E. Dunstan*

CHAPTER 5

"Detailed, real-time characterization of particle deposition during crossflow filtration as influenced by solution properties"

Published in the Journal of Membrane Science 555 (2018): 115-124.

Hongzhan Di, Gregory J. O. Martin, Qiang Sun, Donglin Xie, Dave E. Dunstan*

CHAPTER 6

"Effect of operation conditions on particle deposition and development of an empirical correlation describing the dynamic deposition behaviour"

Manuscript in preparation for submission to a membrane science journal.

Hongzhan Di, Gregory J. O. Martin, Yong Wang, Dave E. Dunstan*

Contents

Chapter 1 Introduction ..... - 1 -
1.1 Membrane filtration ..... - 1 -
1.1.1 Membrane Technologies ..... - 1 -
1.1.2 Membrane configurations ..... - 2 -
1.2 Concentration polarization and Membrane fouling ..... - 4 -
1.3 Theoretical models of membrane filtration ..... - 5 -
1.3.1 Film theory model ..... - 5 -
1.3.2 Resistance-in-series model ..... - 5 -
1.3.3 Osmotic pressure model ..... - 6 -
1.3.4 Pore blocking model ..... - 7 -
1.4 Factors affecting membrane fouling ..... - 8 -
1.4.1 Solution properties ..... - 8 -
1.4.2 Operating conditions ..... - 9 -
1.4.3 Membrane and particle properties ..... - 10 -
1.5 Characterisation methods ..... - 11 -
1.6 Project aim and overview of thesis ..... - 12 -
Chapter 2 A Review of Microstructural Measurements of Membrane Fouling during Filtration Processes ..... - 14 -
2.1 Techniques for determining concentration profiles ..... - 14 -
2.1.1 Shadowgraph ..... - 16 -
2.1.2 Refractometry ..... - 18 -
2.1.3 Electro diode array microscope (EDAM) ..... - 19 -
2.1.4 Holographic interferometry ..... - 20 -
2.1.5 Small-angle X-ray scattering ..... - 21 -
2.2 Techniques for determining the boundary layer thickness ..... - 23 -
2.2.1 Nuclear magnetic resonance (NMR) micro-imaging ..... - 25 -
2.2.3 Optical laser sensor ..... - 26 -
2.2.4 Photointerrupter sensor ..... - 27 -
2.2.5 Ultrasonic time-domain refractometry (UTDR) ..... - 28 -
2.2.6 Direct microscopic observation ..... - 29 -
2.2.7 Microfluidic membrane chip ..... - 30 -
2.3 Techniques for visualising the membrane surface ..... - 31 -
2.3.1 Direct observation through the membrane (DOTM) ..... - 31 -

2.3.2 Direct visual observation (DVO) ..... - 34 -
2.3.3 Confocal scanning laser microscopy (CSLM) ..... - 34 -
2.3.4 Microfluidic channels and sieves ..... - 35 -
2.4 Effects of influencing factors on microstructural measurements of the boundary layer ... - 36 -
2.4.1 Effect of transmembrane pressure ..... - 39 -
2.4.2 Effect of feed concentration ..... - 40 -
2.4.3 Effect of crossflow velocity ..... - 41 -
2.4.4 Effect of *p*H ..... - 41 -
2.4.5 Effect of ionic strength ..... - 42 -
2.5 Conclusions ..... - 42 -
Chapter 3 Development of A Novel Microfluidic System for Studying Particle Deposition during Ultrafiltration ..... - 44 -
3.1 System design ..... - 44 -
3.2 Materials and methods ..... - 45 -
3.2.1 Materials ..... - 45 -
3.2.2 Membrane filtration processes ..... - 46 -
3.2.3 Characterisation method ..... - 46 -
3.3 Microfluidic filtration device fabrication ..... - 47 -
3.3.1 Channel-patterned PDMS layer ..... - 47 -
3.3.2 Device assembly ..... - 49 -
3.4 Results and discussions ..... - 51 -
3.4.1 Particle deposition on the membrane surface ..... - 51 -
3.4.2 Boundary layer profiles ..... - 54 -
3.5 Conclusions ..... - 56 -
Chapter 4 Membrane-Particle and Particle-Particle Interactions as Influenced by Solution pH and Ionic Strength ..... - 57 -
4.1 Introduction ..... - 57 -
4.2 Interaction energies ..... - 58 -
4.2.1 Electrostatic interaction energy ..... - 59 -
4.2.2 Van der Waals attraction energy ..... - 60 -
4.3 Materials and Methods ..... - 61 -
4.3.1 Materials ..... - 61 -
4.3.2 Measurements of zeta potential of latex particles ..... - 61 -
4.3.3 Measurements of the zeta potential of membranes ..... - 61 -
4.4 Results and Discussions ..... - 63 -
4.4.1 Zeta potential and particle size of the latex particles ..... - 63 -

4.4.2 Membrane zeta potential ..... - 65 -
4.4.3 Interaction energies ..... - 66 -
4.5 Conclusions ..... - 68 -
Chapter 5 Detailed, Real-time Characterisation of Particle Deposition during Crossflow Filtration as Influenced by Solution Properties ..... - 69 -
5.1 Introduction ..... - 69 -
5.2 Materials and Methods ..... - 70 -
5.3 Results and discussions ..... - 71 -
5.3.1 Effect of pH ..... - 71 -
5.3.2 Effect of ionic strength ..... - 77 -
5.3.3 Effect of feed concentration ..... - 81 -
5.4 Summary for all conditions ..... - 85 -
5.5 Conclusions ..... - 85 -
Chapter 6 Effect of Operating Conditions on Particle Deposition and Development of an Empirical Correlation Describing the Dynamic Deposition Behaviour ..... - 87 -
6.1 Introduction ..... - 87 -
6.2 Theory ..... - 88 -
6.2.1 Hydrodynamic force determination ..... - 89 -
6.2.2 Particle deposition probability ..... - 90 -
6.3 Materials and Methods ..... - 92 -
6.4 Results ..... - 92 -
6.4.1 Effect of permeate flow rate ..... - 92 -
6.4.2 Effect of cross-flow velocity ..... - 95 -
6.4.3 Correlation for all conditions ..... - 100 -
6.5 Conclusions ..... - 102 -
Chapter 7 Conclusions and Future Perspectives ..... - 104 -
7.1 Conclusions ..... - 104 -
7.2 Future perspectives ..... - 105 -
Reference ..... - 106 -

List of Figures

Figure 1-1 Passed and rejected components based on membrane pore size. From microfiltration to reverse osmosis, membrane pore size decreases and more components are rejected. Image is reproduced from the website of Koch Membrane Systems Inc. (http://www.kochmembrane.com).

Figure 1-2 Schematics of membrane configurations. a) Tubular membrane comprising of tube-like structures with porous walls; b) Spiral membrane comprising of layers of flat sheet membrane rolling around a permeate tube; c) Hollow fiber membrane comprising of numerous porous hollow fibres. Images are reproduced from the website of Koch Membrane Systems In (http://www.kochmembrane.com).

Figure 1-3 Schematic of membrane filtration processes during crossflow filtration of monodisperse solution. An irreversible fouling layer forms on the membrane surface and a reversible concentration polarization layer forms between the bulk flow and the fouling layer during the membrane filtration process.

Figure 1-4 Schematic of fouling models, a) Complete pore blocking: membrane pores are completed blocked by particles, the size of which is the same as or larger than the membrane pore size; ; b) Internal pore blocking: smaller particles deposited on the pore walls; c) Intermediate pore blocking: particles deposited on particles that already blocked membrane pores or deposited on the non-porous area of the membrane surface; and d) Cake filtration: an additional cake layer formed on the membrane surface.

Figure 1-5 Schematic of a) dead-end filtration, and b) crossflow filtration of bidisperse solution. The feed flow is push towards the membrane in dead-end filtration, while the flow direction is parallel with the membrane in crossflow filtration.

Figure 1-6 Schematic of interaction energies of membrane-particle (*Vm-p*), particle-particle (*Vp-p*), and hydrodynamic forces exerted on particles during crossflow filtration of particle suspensions. *Fx* is drag force due to the crossflow, F_{yP} is drag force caused by the permeate flow, F_{yL} is lateral lift force caused by the crossflow, and F_{yB} is buoyancy force of the particle.

Figure 2-1 Concentration profiles C (d, t), concentration as a function of distance away the membrane surface and filtration time, obtained by electro diode array microscope (EDAM) under different cross flow rate (Re=0, and Re=10) by Mc Donogh et al [92].

Figure 2-2 Schematic diagram of the light paths (solid line) and refractive index gradient (dashed line) of shadowgraph technique. Laser light is deflected and bends out its original path due to the variations in the refractive index in a fluid. The changes of illumination positions are captured by the image plate. Adapted from Vilker et al [88].

Figure 2-3 Cross-section of the flow cell used for refractometry. A is the reference side, and B is the biopolymer side. The beam travelling through B is deflected to the new position due to the varied refractive index [90].

Figure 2-4 Schematic of holographic interferometry. The laser beam is divided in two by means of a varable beam splitter (BS). The direction of two beams is modified by two mirrors, M2 and M3, respectively. One of the beams illuminates the RO module and the light spread out is recorded by the holographic plate (HP). The other beam acts as a reference and is also recorded by HP. All of this image information is collected by video camera (VC) [96].

Figure 2-5 Picture of the SAXS cross-flow filtration cell. X-ray beams travel through a cross section of a crossflow filtration cell. Scattering patterns caused by the presence of particles in the flow are recorded [101].

Figure 2-6 Schematic of the principle of laser triangulometry. Object 1 refers to the cake layer thickness, and object 2 refers to the membrane surface. The reflected laser beams are captured by CCD camera [110].

Figure 2-7 Schematic diagram of cake layer thickness measurement by a photointerrupter sensor. The emitted light is reflected by the surface of the membrane or the cake layer, and then detected by the sensor [113].

Figure 2-8 Schematic principle of Ultrasonic time-domain refrectometry technique. In a crossflow filtration cell, ultrasonic waves encounter the surfaces of the fouling layer and the membrane and are reflected at different distances with different amplitude and arrivals times [114].

Figure 2-9 Picture of the direct observation experimental setup comprising of a hollow fiber membrane module, a microscope, and a video camera. The upper right corner of the image shows that the dark area is the observed hollow fiber [75].

Figure 2-10 Chip showing channels and flow directions. The active membrane is between the retentate channel and the permeate channel [46].

Figure 2-11 Schematic of direct observation through the membrane (DOTM) apparatus. Microscope lens locates on the permeate side of a transparent membrane in a cross-filtration cell to observe the fouling process on the membrane, and visualization information is recorded by a video camera [127].

Figure 2-12 Schematic of direct visual observation (DVO) apparatus. Microscope is mounted on the retentate side of the membrane in a crossflow filtration cell. The fouling process is recorded by a camera [77].

Figure 2-13 Schematic diagram of the distance-dependent concentration profile. Region I is the fouling layer with gradual concentration change. Region II is the concentration polarisation layer with a relatively dramatic concentration change. Region III is the bulk flow with the feed concentration. Cm = concentration at the membrane surface. C0 = feed concentration. d = distance from the membrane surface. δ = boundary layer thickness.

Figure 2-14 Effects of variable conditions on microstructural measurements of the boundary layer. C_m = concentration at the membrane surface. C_0 = feed concentration. d = distance from the membrane surface. Solid curve stands for the reference curve. Dashed curve 1 (higher C_m, higher δ), curve 2 (higher C_m, lower δ), and curve 3 (lower C_m, lower δ) stands for three different cases under variable conditions.

Figure 3-1 a) Schematic diagram of the microfluidic membrane filtration system. b) Schematic diagram of particle deposition on the membrane surface inside the device during cross-flow filtration. ΔP_V is the pressure drop across the microchannel to drive the fluid flow. ΔP_T is the transmembrane pressure. The magnitude of infusion velocity v_1 and withdraw velocity v_2 can be controlled to vary ΔP_V and ΔP_T independently.

Figure 3-2 The principle steps in the procedure for fabricating the master mould using lithography. (a) wafer pre-treat (baked and dehydrated), (b) SU-8 photoresist coat, (c) soft bake by putting wafer on a hot plate, (d) UV exposure, (e) post exposure bake by putting wafer on a hot plate, (f) develop the pattern using SU-8 photoresist developer, and (e) rinse and dry to get the final master mould with patterns standing on the wafer. The thickness of the patterned SU-8 photoresist is 25 μm ± 2 μm. Only one channel structure is shown, while there were six channels on one mask and wafer.

Figure 3-3 Schematic diagram of the casting-patterned PDMS layer. The thickness is 50 ±2 μm, and the channel depth is 25 ± 2 μm. (a) coat silane layer on the mould, (b) cast uncured PDMS on the mould, (c) bake the wafer and PDMS in an oven, (d) peel patterned PDMS layer off the mould. Only one channel structure is shown, while there were six channels on one wafer and PDMS layer.

Figure 3-4 Chemical mechanisms of the bonding of the PDMS and PES layers. The step included: (a) replacement of the alkoxy groups of APTES with hydroxyl groups, (b) creation of hydroxyl groups on the PES membrane surface, (c) formation of C-O-Si bonds to coat APTES onto the PES membrane surface, (d) introduction of hydroxyl groups onto PDMS surfaces, (e) introduction of hydroxyl groups onto functionalised PES surfaces, (f) formation C-O-Si bonds between PES and PDMS.

Figure 3-5 a) Schematic diagram of the cross section of the inlet/outlet, and b) final appearance of the device. From the bottom to the top are cover glass, patterned PDMS layer, PES membrane, silicone pad, and silicone tubing respectively.

Figure 3-6 Images of the membrane surfaces at different times during filtration of latex suspensions. (a) 0.01 M KCl suspension. (b) 1 M KCl suspension. More deposition is observed as filtration time increases, and more aggregates are found with the presence of 1M KCl in suspension. The dimensions were 100 μm by 50 μm for the temporal images, and 18 μm by 17 μm for the 3x magnified images.

Figure 3-7 Percentage of the deposition layer occupied by isolated particles (blue diamonds), aggregates of two particles (red squares), and aggregates of more than two particles (green triangles) as a function of filtration time in (a) 0.01 M KCl and (b) 1M KCl suspensions.

Figure 3-8 Covered area fraction φ as a function of filtration time t. Red markers stand for 0.01 M KCl suspension. Blue markers stand for 1 M KCl suspension.

Figure 3-9 Three-dimensional images of the microfluidic filtration device at different time during filtration of latex suspensions. (a) 0.01 M KCl concentrated suspension. (b) 1 M KCl suspension.

Figure 3-10 Boundary layer profiles. Covered area fraction φ as a function of the distance from the membrane surface z at different filtration time. Red lines stand for latex suspensions with 0.01 M KCl. Blue lines stand for latex suspensions with 1 M KCl. Dotted lines are obtained at 6 minutes, dashed lines are obtained at 25 minutes, and solid lines are obtained at 45 minutes.

Figure 4-1 Diagrammatic representation of the interaction energies relevant to membrane-particle and particle-particle interactions during cross-flow filtration. V_{m-p} = Interaction energy between membrane and particle; V_{p-p} = Interaction energy between particle and particle; edl = electric double layer.

Figure 4-2 Schematic representation of the clamping cell of the SurPass instrument. The clamping cell comprising two layers of membrane and a flow channel in sandwich form. The downstream convection of ions via pressure-driven flow induces a streaming potential which can be related to the zeta potential of the membrane [149].

Figure 4-3 Zeta potential of latex particles as a function of pH, KCl concentration and latex volume fraction. pH varies from 3 to 8, KCl concentration varies from 0.01 to 1 M, and latex volume fraction varies from 5×10^{-6} to 8×10^{-5}. Latex particles are negatively charged for all tested conditions. The magnitude of the zeta potential increases as pH increases and as KCl concentration decreases. Latex volume fraction shows less influence on the zeta potential of latex particles.

Figure 4-4 Particle sizes as a function of pH, KCl concentration and latex volume fraction. pH varies from 3 to 8, KCl concentration varies from 0.01 to 1 M, and latex volume fraction varies from 5×10^{-6} to 8×10^{-5}. The size of latex particles are barely affected by pH, latex volume fraction and lower KCl concentration (0.01M and 0.1M). Aggregates are found at 1M KCl.

Figure 4-5 Zeta potential of the membrane surface a) as function of pH when the KCl concentration is 0.01M and b) as a function of KCl concentration at pH 5.6. The membrane surface is positively charged and zeta potential decreases as pH increases with the presence of 0.01M KCl in solution. As KCl concentration increased from 0.005 to 1 M, the charge of the membrane surface converts from being positive to being negative.

Figure 4-6 Interaction energies of particle-particle as a function of a) pH with the presence of 0.01M KCl and b) KCl concentration at pH 5.6. Interaction energies of particle-membrane as function of c) pH with the presence of 0.01M KCl and b) KCl concentration at pH 5.6. As pH increases, both the repulsion between particles and the attraction between the membrane and particles increase. As KCl concentration increases, the repulsion between particles converts to be attraction and the attraction between the membrane and particles converts to be repulsion.

Figure 5-1 Images of the membrane surface, side view, and 3D view of the channel after 50 minutes filtration at a) pH 3, b) pH 4, c) pH 5.6, and d) pH 8. The field of view of the membrane is around 100 μm long and 50 μm wide, and the depth of the channel shown is around 20 μm. The KCl concentration was 0.01M and the volume fraction of latex particle was 2×10^{-5}.

Figure 5-2 a) Surface coverage by deposition and b) volume of deposition per membrane area as a function of filtration time and pH values. c) Percentages of isolated particles and aggregates in the deposition at pH 5.6 (blue diamond symbols) and pH 8 (red square symbols) as a function of filtration time. d) Normalised deposition volume (cumulative volume of deposition normalised by cumulative volume of solute towards the membrane) as a function of filtration time and pH values. The KCl concentration was 0.01M and the volume fraction of latex particle was 2×10^{-5}.

Figure 5-3 Interaction energies between the membrane and particles at a Debye length of 3 nm, and between particles as a function of pH. Red square symbols represent the energy barrier between particles (p-p). Blue diamond symbols represent the interaction energy between particles and the membrane (m-p). The KCl concentration was 0.01M and the volume fraction of latex particles was 2×10^{-5}. As pH increases, both the repulsive energy between individual particles and attractive energy between the membrane and particles increase.

Figure 5-4 Images of the membrane surface, side view, and 3D view of channel after 50 minutes filtration when the KCl concentration was a) 0.01M, b) 0.1M, and c) 1M in the feed solution (Fig.7a is the same with Fig.3c). Less deposition and more aggregates are found at higher KCl concentration. The field of view of the membrane is around 100 μm long and 50 μm wide, and the depth of the channel shown is around 20 μm. The pH was 5.6 and the volume fraction of latex particle was 2×10^{-5}.

Figure 5-5 a) Surface coverage by deposition, b) volume of deposition per membrane area, and c) normalised deposition volume (cumulative volume of deposition normalised by cumulative

volume of solute towards the membrane) as a function of filtration time and KCl concentration. The pH was 5.6 and the volume fraction of latex particle was 2×10^{-5}. Increasing KCl concentration decreases surface coverage, deposition volume and normalised deposition volume.

Figure 5-6 Images of the membrane surface, side view, and 3D view of channel after 50 minutes filtration with particle volume fraction of a) 5×10^{-6}, b) 2×10^{-5}, and c) 8×10^{-5} (Fig.8b is the same with Fig.3c). The field of view of the membrane is around 100 µm long and 50 µm wide, and the depth of the channel shown is around 20 µm. The pH was 5.6 and he KCl concentration was 0.01M.

Figure 5-7 a) Surface coverage by deposition, b) volume of deposition per membrane area, and c) normalised deposition volume (cumulative volume of deposition normalised by cumulative volume of solute towards the membrane) as a function of filtration time and volume fraction of particles in the feed. The pH was 5.6 and KCl concentration was 0.01M. As filtration time increases, surface coverage and deposition volume increase, while normalised deposition volume decreases. Increasing volume fraction increases surface coverage and deposition volume while barely affects normalised deposition volume.

Figure 6-1 Image showing the forces acting upon a spherical particle in contact with a protrusion of height *h*. The particle is subjected to forces along the x-direction (main flow direction) and y-direction (permeate flow direction).

Figure 6-2 Images of the membrane surface, side view, and 3D view of channel after 50 minutes filtration with a permeate flux of a) 12.5 L/h/m2, b) 25 L/h/m2, and c) 75 L/h/m2. The crossflow velocity is 20 m/h. The field of view of the membrane is around 100 µm long and 50 µm wide, and the depth of the channel shown in is around 20 µm. As permeate flux increases, more deposition is observed as well as more dense deposit layer.

Figure 6-3 a) Surface coverage by deposition, and b) volume of deposition per membrane area as a function of filtration time and permeate flux. The crossflow velocity is 20 m/h. Both of surface coverage and deposition volume increase with increasing filtration time and increasing permeate flux.

Figure 6-4 Images of the membrane surface, side view, and 3D view of channel after 50 minutes filtration at crossflow velocity of a) 10m/h, b) 15 m/h, and c) 30m/h, d) 40 m/h. Images at crossflow velocity of 20 m/h is presented in Fig.2b. The permeate flux is 25 L/h/m^2. The field of view of the membrane is around 100 µm long and 50 µm wide, and the depth of the channel shown in is around 20 µm.

Figure 6-5 a) Surface coverage by deposition and b) deposition volume as a function of filtration time and crossflow velocity. Both of surface coverage and deposition volume increase with increasing filtration time and decreasing crossflow velocity.

Figure 6-6 Surface coverage by deposition (blue diamond symbols) and volume of deposition per membrane area (red square symbols) after 50 minutes filtration as a function of crossflow velocity. The permeate flux is 25L/h/m^2.

Figure 6-7 Normalised deposition volume (cumulative volume of deposition normalised by cumulative volume of solute towards the membrane) as a function of filtration time and crossflow velocity. The permeate flux is 25L/h/m^2.

Definitions of Terms and Symbols Used in the Text

r_p	Particle radius (m)
A	Cross-sectional area (m^2)
A_H	Hamaker coefficient (J)
AARD	Average absolute value of the relative deviation
D	Distance of closest approach between two surfaces (m)
C_0	Initial feed concentration
$C(d, t)$	Concentration profiles
C_m	Concentration at/near the membrane surface
c_i	Concentration of ion i
D_H	Hydraulic diameter (m)
d_p	Diameter of particles (m)
e	Proton charge (1.6×10^{-19} C)
f	Friction factor correlation
f_c	Dimensionless coefficient of force acting on a particle in contact with a plane
F	Hydrodynamic force (N)
F_x	Drag force along crossflow direction due to the cross flow
F_y	Net drag force along permeate flow direction
F_{yB}	Buoyant force of the particle
F_{yP}	Drag force along permeate flow direction due to the permeate flow
F_{yL}	Lift force along permeate flow direction due to the cross flow
J	Permeate flux ($m \cdot s^{-1}$)
J_0	Initial permeate flux ($m \cdot s^{-1}$)
J_∞	Limit/stable flux ($m \cdot s^{-1}$)
h	Protrusion height (m)
k_B	Boltzmann's constant (1.38×10^{-23} $J \cdot K^{-1}$)
Ke	Dielectric constant
M_w	Molecular weight cut-off
n_i	Refractive index of the medium i
n/V	Total number of moles of molecules in volume V
P	Wetted perimeter of channel walls (m)
ΔP	Transmembrane pressure (Pa)
R	Gas constant (8.314 $J \cdot mol \cdot K^{-1}$)
R_e	Reynolds number
S	Distance between the centers of two particles (m)
S^*	Distance between the particle surface and the membrane surface (m)
T	Absolute temperature (K)

U_x	Crossflow velocity ($m \cdot s^{-1}$)
v	Transmembrane velocity ($m \cdot s^{-1}$)
V_e	Electrostatic interaction energy (J)
$V_{m\text{-}p}$	Total interaction energy of membrane-particle (J)
V_{hyd}	Net hydrodynamic energy driving particles to membrane (J)
$V_{p\text{-}p}$	Total interaction energy of particle-particle (J)
V_T	Total interaction energy (J)
V_{vdW}	Van der Waals interaction energy (J)
ψ	Reduced surface potential
$\psi(h)$	Effective surface potential that varies with separation distance h
z_i	Charge number of ion i

Greek letters

ε	Solution permittivity ($C \cdot V^{-1} \cdot m^{-1}$)
ε_0	Vacuum permittivity ($C \cdot V^{-1} \cdot m^{-1}$)
ε_i	Dielectric permittivity of the medium i ($C \cdot V^{-1} \cdot m^{-1}$)
η	Dynamic viscosity ($Pa \cdot s$)
κ	Inverse Debye length (m^{-1})
λ	Debye length (m)
δ	Boundary layer thickness (m)
ρ	Liquid density ($kg \cdot m^{-3)}$
ρ_P	Particle density ($kg \cdot m^{-3}$)
τ_w	Wall shear stress (Pa)
Π	Osmotic pressure ($N \cdot m^{-2}$)
φ_V	Overall volume of deposited particles per membrane area ($\mu m^3 \cdot \mu m^{-2}$)
γ	Deposition probability

Chapter 1 Introduction

1.1 Membrane filtration

Membrane filtration is a pressure-driven separation technology that has been employed in a wide range of industries including dairy[1, 2], water purification[3-5], wastewater treatment [6-8], and beverage manufacture [2, 9, 10]. Membranes are thin sheets of semi-permeable material that separate substances in a fluid when a driving force (e.g. pressure difference) is applied across the membrane [11]. The pore size and membrane surface properties can be precisely tailored to the specific requirements of the finished products. The range of commercially available membrane pore sizes now covers the size range from 0.1 to 10^4 nm [12]. Compared to other traditional separation technologies such as thermal processes, decantation, centrifugation, and chromatography, membrane filtration has advantages including low operation temperature, less energy consumption, and higher separation efficiency [13, 14].

1.1.1 Membrane Technologies

Membrane technologies can be broadly categorised based on the pore size, as microfiltration (MF), ultrafiltration (UF), nanofiltration (NF), and reverse osmosis (RO) (Figure 1-1). These technologies have been employed for numerous applications from removing salt to filtering large particulates in viscous fluids. Microfiltration has the largest pore size and is commonly used to separate suspended solids with diameters between 0.1 and 10 μm [15]. For example, microfiltration has been employed in clarification of dextrose and coloured fruit juices [14, 16] and for sterilization of wine and beer by removing bacteria [17]. Ultrafiltration membranes have smaller pores between 1 and 100 nm to separate water and microsolutes from macromolecules and colloids. They are widely used to concentrate milk solids for cheese productions by removing water and selected non-protein components from milk [18]. Compared to microfiltration and ultrafiltration, nanofiltration and reverse osmosis offer finer separation with membrane pores >1 nm. They are generally targeted to remove ions, for instance in desalting process streams [19].

Membrane technologies can also be used in combination, such as ultrafiltration followed by reverse osmosis for seawater desalination processes.

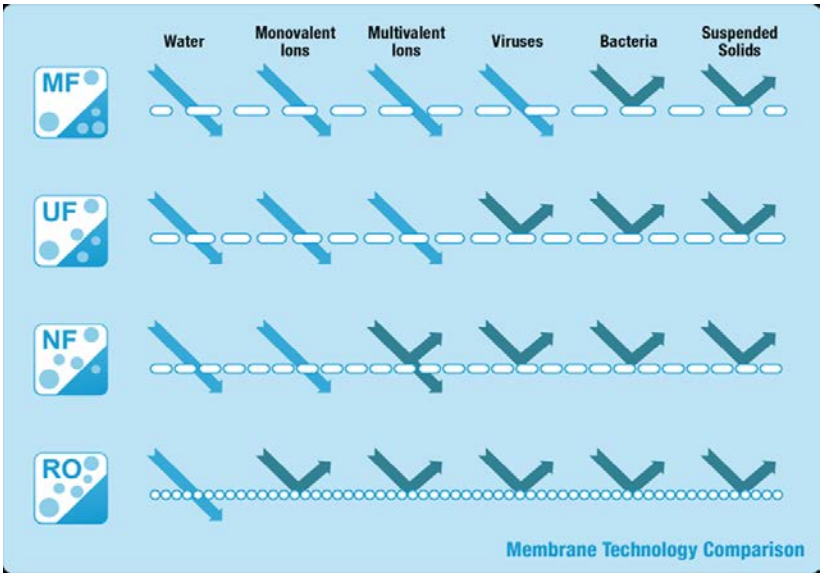

Figure 1-1 Passed and rejected components based on membrane pore size. From microfiltration to reverse osmosis, membrane pore size decreases and more components are rejected. Image is reproduced from the website of Koch Membrane Systems Inc. (http://www.kochmembrane.com).

1.1.2 Membrane configurations

Membranes can be fabricated in four basic configurations - flat sheet, tubular, spiral, and hollow fibre. Each configuration differs in terms of the packaging, types of materials used, and applications. For bench-scale membrane filtration research, flat sheet membranes are more commonly used, as the equipment is simple to fabricate, the shear rate at the membrane surface can be easily controlled, interpretation of fouling data is straightforward, and microscopy analyses on flat sheet membranes are more easily accessible [20]. Commercial membranes, on the other hand, usually use the other three configurations. Tubular membranes are tube-like structures with porous walls, which are suited to processing difficult feed solutions with high dissolved/suspended solids (Figure 1-2a). Spiral membranes are made from layers of flat sheet membranes, feed spacers, permeate spacers and a permeate tube. The feed solution travels through the flow channels tangentially across the length of the element, and permeate exits through the permeate tube. This configuration provides the highest membrane-packing area with the smallest

footprint (Figure 1-2b). Hollow fibre membranes modules utilise numerous long porous hollow fibres packed inside a housing, offering a compact, cost-effective solution for filtering large volumes of liquids using minimal space (Figure 1-2c). According to the filtration process needs, specific membrane configurations can be selected for effective operation.

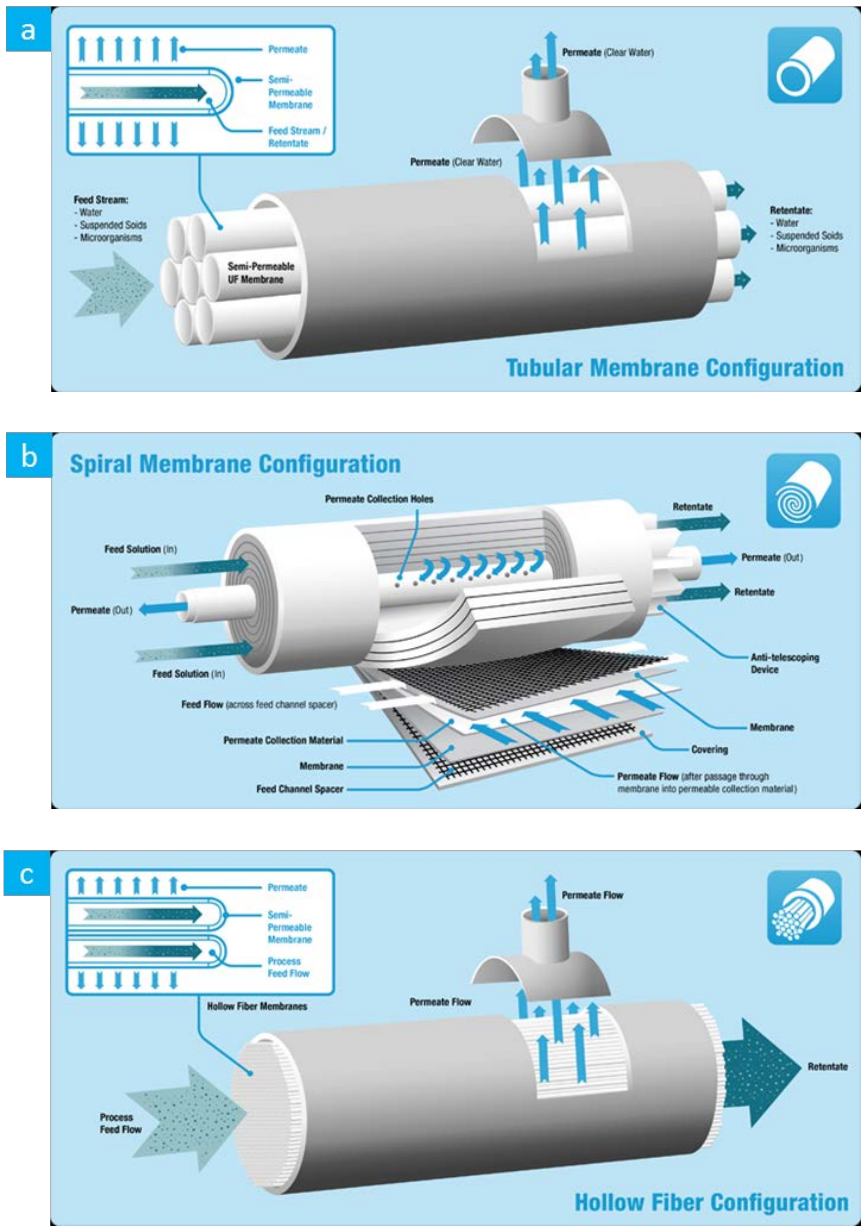

Figure 1-2 Schematics of membrane configurations. a) Tubular membrane comprising of tube-like structures with porous walls; b) Spiral membrane comprising of layers of flat sheet membrane rolling around a permeate tube; c) Hollow fiber membrane comprising of numerous porous hollow fibres. Images are reproduced from the website of Koch Membrane Systems Inc. (http://www.kochmembrane.com).

1.2 Concentration polarization and Membrane fouling

During membrane filtration processes, smaller particles and solvent pass through the membrane, while larger particles are retained, resulting in the higher concentration of solutes near the membrane surface compared to the bulk (Figure 1-3). “Concentration polarisation” is the term used to describe the concentration gradient from the membrane surface to the bulk which is independent of the membrane properties. On the other hand, the deposition and adsorption of particles on the membrane surface or inside the membrane pores is termed “membrane fouling” [21, 22]. Both concentration polarisation and membrane fouling are responsible for the flux decline that occurs during filtration processes [13, 22, 23]. Concentration polarisation is considered to be reversible and transient. It appears immediately upon application of a transmembrane pressure (TMP) and disappears once the filtration process stops. Membrane fouling, however, develops more gradually and is more likely to be irreversible, and can significantly reduce the separation performance [13, 22, 24].

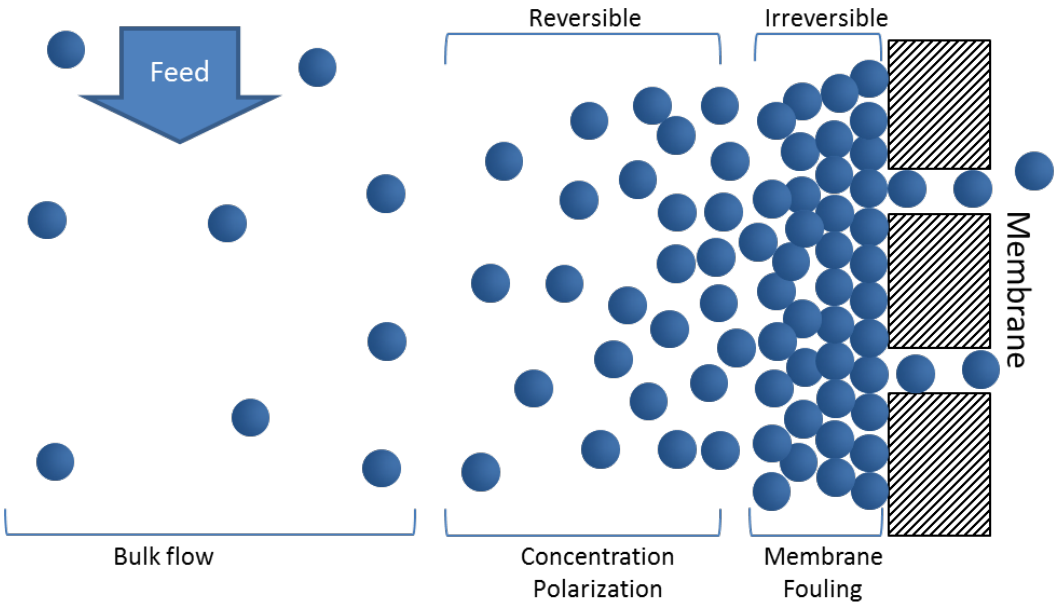

Figure 1-3 Schematic of membrane filtration processes during crossflow filtration of monodisperse solution. An irreversible fouling layer forms on the membrane surface due to the interactions of membrane-particle and particle-particle and a reversible concentration polarization

layer forms due to the compressed concentration between the bulk flow and the fouling layer during the membrane filtration process.

1.3 Theoretical models of membrane filtration

1.3.1 Film theory model

A film theory model was developed by Michaels and others to describe the relationship between concentration polarisation and the permeate flux [25-28]. In this model, the complex membrane transport problem is simplified as a convection-diffusion mass balance from the membrane surface out to a finite mass boundary (film) layer near the membrane surface, where the convective transport of solute to the film layer is equal to the diffusive transport of solute to the bulk flow and convective transport of solute to the permeate side. The equation is

$$J = \frac{D_s}{\delta} \cdot \ln\left(\frac{C_w - C_p}{C_b - C_p}\right) \tag{1-1}$$

where J is the permeate flux, D_s is the solute diffusion coefficient, δ is the boundary (film) layer thickness, C_w is solute concentration at the membrane surface, C_b and C_p are the bulk and permeate solute concentrations, respectively. This model is valid only in the presence of concentration polarisation, while the impact of membrane fouling is not considered.

1.3.2 Resistance-in-series model

Membrane filtration is usually a pressure-driven separation process. A number of mathematical models have been developed to describe the permeate flux in a relationship of applied transmembrane pressure. One of the popular models is the resistance-in-series model. Based on the Darcy's Law, permeate flux through a clean membrane is related to the applied transmembrane pressure [23, 29]:

$$J = \frac{\Delta P}{\eta \cdot R_m} \tag{1-2}$$

where ΔP is applied transmembrane pressure, η is liquid viscosity, and R_m is membrane resistance during filtration of water, which depends on the membrane properties and morphologies. In reality, the occurance of concentration polarisation and membrane fouling give rise to another two resistances, R_{cp} and R_f, respectively. For filtration of colloidal substances solutions or protein-containing liquids, a cross-linked gel layer may form when the concentration reaches a specific high value, resulting in a gel layer resistance, R_{gel}. Equation 1-2 can then be modified as [30, 31]

$$J = \frac{\Delta P}{\eta \cdot \left(R_m + R_{cp} + R_f + R_{gel}\right)} \tag{1-3}$$

which can be used for filtration processes operated in a constant pressure mode, and a range of resistance concentration polarisation, membrane fouling, gel formation, and other potential resistance can be included in this resistance-in-series model.

1.3.3 Osmotic pressure model

Similar to the resistance-in-series model, the osmotic pressure model is also derived from Darcy's law. The effect of membrane fouling on the permeate flux is still characterised as an additional resistance, R_f, in series with the membrane resistance, R_m. Whereas the concentration polarisation is expressed as a resistance term in the resistance-in-series model, it is considered as an osmotic pressure Π in this model. Separation of a solute by the membrane gives rise to an increase in the concentration on the retention side, resulting in the concentration difference between the retention side and the permeate side of the membrane. When this difference increases, an osmotic pressure opposite to the transmembrane pressure arises, resulting in the reduction of the net driving force as following [32]:

$$J = \frac{\Delta P - \Pi}{\eta \cdot \left(R_m + R_f\right)} \tag{1-4}$$

1.3.4 Pore blocking model

Hermia et al. [32] proposed an empirical pore blocking model to describe membrane fouling. The schematic of particle deposition is shown in Figure 1-4. Figure1-4a shows the complete pore blocking, where the size of particles is the same as, or slightly larger than that of membrane pores. Each particle arriving at the membrane completely blocks a pore, leading to a severe decrease of permeate flux. In internal pore blocking, the size of particles is smaller than that of the membrane pores. Each particle arriving at the membrane is deposited onto the internal pore walls, resulting in a decreased pore volume (Figure 1-4b). As the filtration time increases, the number of open pores decreases. Particles newly reaching the membrane may deposit onto the particles that already blocked certain pores, or onto the membrane (non-porous areas), which is the so called 'intermediate blocking' phenomenon. The size of particle can be either larger or similar than the size of membrane pores (Figure1-4c). In the case of cake filtration, particles are larger than the membrane pores. A cake layer forms on the membrane surface as particles accumulate on top of each other, thereby reducing the flow into the pores (Figure1-4d). A general mathematical form of the different fouling models can be expressed as following [33-36]:

$$\frac{d^2t}{dV^2} = \mathrm{k}\left(\frac{dt}{dV}\right)^n \tag{1-5}$$

where t is filtration time, and V is volume filtered. k is the filtration constant. The component n characterises the fouling models, which takes the values of 2, 3/2, 1, or 0, corresponding to complete blocking, standard pore blocking, intermediate pore blocking, and cake filtration, respectively.

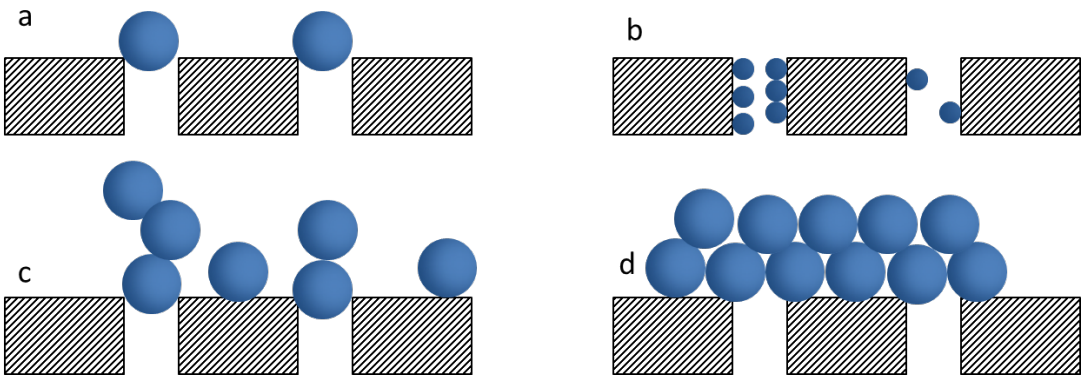

Figure 1-4 Schematic of fouling models, a) Complete pore blocking: membrane pores are completed blocked by particles, the size of which is the same as or larger than the membrane pore size; ; b) Internal pore blocking: smaller particles deposited on the pore walls; c) Intermediate pore blocking: particles deposited on particles that already blocked membrane pores or deposited on the non-porous area of the membrane surface; and d) Cake filtration: an additional cake layer formed on the membrane surface.

1.4 Factors affecting membrane fouling

1.4.1 Solution properties

Membrane fouling has been reported to be significantly influenced by solution properties, including pH [37-39], ionic strength [39-41], and feed concentrations [42-44]. Both of pH and ionic strength can affect the interactions of membrane-particle and particle-particle by varying the charge properties of membranes and particles. For example, during the filtration of the milk protein bovine serum albumin (BSA), the severest fouling and lowest flux occurred at a pH equal to the iso-electric point (IEP) of BSA, where the intermolecular repulsion between BSA molecules is at a minimum, allowing aggregate formation to occur [22, 37, 39, 40, 42, 45-47]. The fouling in these systems is related to the intermediate pore blocking and cake filtration models shown in Figure 1-4c and 4d, where particle-particle interactions are involved Ionic strength can influence on membrane fouling as it affects the charge properties of the membrane surface and particles, which in turn affects membrane-particle and particle-particle interactions [37, 39, 47, 48]. Feed concentration has no effect on the charge properties of membranes and particles, and long-term flux tends to be independent of feed concentration [43, 44, 49]. However, increasing

feed concentration generally results in increased fouling and a decrease in the permeate flux due to a greater number of particles being brought to the membrane and greater collision frequency between particles for any unit time [42]. The former may cause rapid complete pore blocking (Figure 1-4a) and internal pore blocking (Figure 1-4b), while the latter affects the in intermediate pore blocking (Figure 1-4c) and cake filtration (Figure 1-4d) models where aggregates form due to particle-particle interactions.

1.4.2 Operating conditions

Membrane filtration is normally operated in a constant TMP mode [11, 50-53]. In this case, increasing the TMP initially results in an increase in the permeate flux, while also resulting in increased fouling due to the greater throughput. Membrane filtration can be operated as dead-end (Figure 1-5a) [54-56] or crossflow filtration (Figure 1-5b) [57-60]. In crossflow filtration, the suspension flows tangentially to the membrane surface, resulting in shear forces that reduce the deposition of particles on the membrane surface. Thus, increasing the crossflow velocity generally reduces membrane fouling.

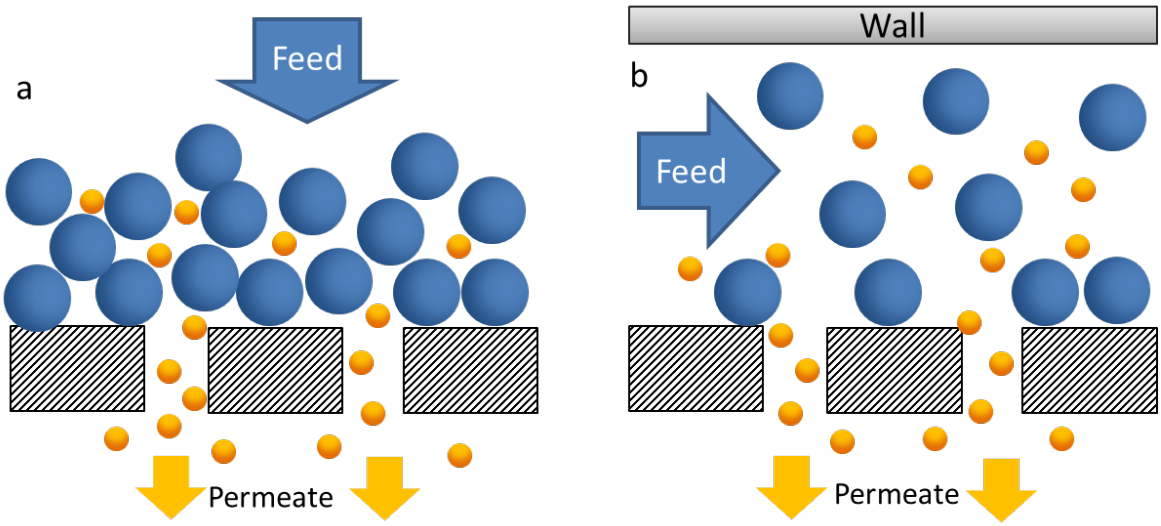

Figure 1-5 Schematic of a) dead-end filtration, and b) crossflow filtration of bidisperse solution. The feed flow is push towards the membrane in dead-end filtration, while the flow direction is parallel with the membrane in crossflow filtration.

1.4.3 Membrane and particle properties

Membrane properties such as pore size distribution, porosity, and surface morphology are important for the separation performance [61-63]. A membrane with a wide ranging pore size distribution generally has poor selectivity. Other physico-chemical properties of membranes, including membrane materials, surface charge, and hydrophobicity/hydrophilicity also have important effects on membrane fouling [46, 64-70]. Similarly, the changes of particle properties can affect membrane fouling by varying membrane-particle interactions and particle-particle interactions. For example, severe fouling occurs when the membrane and particles are charged oppositely due to the attraction energy between the membrane and particles [71].

The above factors can influence membrane fouling through their effects on the membrane-particle and particle-particle interactions, or the hydrodynamic forces exerted on the particles in the feed flow (Figure 1-6). Solution properties such as pH, ionic strength and particle concentration primarily influence the interactions of membrane-particle ($V_{m\text{-}p}$), particle-particle ($V_{p\text{-}p}$). The operating conditions such as cross-flow velocity and TMP mainly affect the hydrodynamic forces. Membrane/particle properties can affect both the interaction energies and the hydrodynamic forces. During crossflow filtration, there is a drag force F_x exerted on the particle along the x-direction (feed dirction), which is caused by the crossflow. Along the y-direction (permeate direction), there are three forces acting on the particles: F_{yP} (drag force caused by the permeate flow), F_{yL} (lateral lift force caused by the crossflow), and F_{yB} (buoyancy force of the particle).

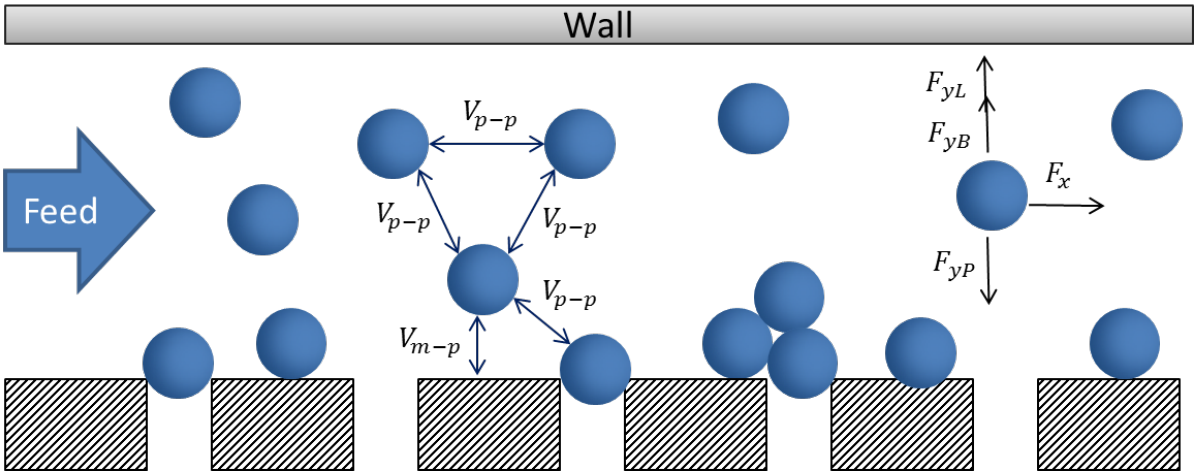

Figure 1-6 Schematic of interaction energies of membrane-particle ($V_{m\text{-}p}$), particle-particle ($V_{p\text{-}p}$), and hydrodynamic forces exerted on particles during crossflow filtration of particle suspensions. F_x is drag force due to the crossflow, F_{yP} is drag force caused by the permeate flow, F_{yL} is lateral lift force caused by the crossflow, and F_{yB} is buoyancy force of the particle.

1.5 Characterisation methods

A large number of studies have used macroscopic measurements like flux-time behaviour and pressure-time behaviour to characterise membrane fouling under various filtration conditions [37, 39, 40, 42, 43, 45, 46, 48, 67, 72, 73]. These measurements have successfully demonstrated the influence of variable conditions on the macroscopic filtration behaviours. However, the actual fouling process which governs the filtration performances can only be inferred, and the fundamental mechanism of membrane fouling has yet been fully understood.

For direct measurements of membrane fouling processes, a variety of visualisation methods have been developed involving microscopy [74-78] and microfluidic technologies [71, 79-85]. By visualising the deposition process of particles and analysing the structure and distribution of the deposited layers, fundamental information has been obtained for better understanding of fouling mechanisms. Chapter 2 provides a thorough review of these techniques, the information obtained to date through their application, and the current limits to our understanding of the mechanisms of particle deposition and membrane fouling.

1.6 Project aim and overview of thesis

This project aims to develop a new fundamental understanding of membrane fouling through the development and application of a microfluidic filtration system. This purpose of the device is to provide detailed microscopic structures of the deposit layer and deposition distributions over a wide range of solution properties and operating conditions. These observations are then used in combination with theoretical considerations to help develop the fouling mechanisms.

Chapter 2 reviews the state-of-the-art techniques that are available for microstructural measurement of deposit layers present during membrane filtration. These methods are examined with respect to their abilities to perform measurements such as characterising particle concentration profiles, determining the deposit layer thickness, and visualising the membrane surface. The current state of knowledge of the effects of various operational conditions on concentration profiles and layer thickness are summarised in relation to macroscopic flux measurements. Additionally, the techniques are categorised based on their applicability to different filtration modes (crossflow or dead-end), membrane types (flat, hollow fibre, or special cells), and their measurement limits.

Chapter 3 describes the development of a novel microfluidic filtration system which can be used for direct measurements of membrane fouling. This system is developed by incorporating membrane filtration with microfluidic technology, confocal microscopy, and a two-syringe flow control system. It is capable of direct visualisation of the deposition process of submicron particles on the membrane surface. Time dependent and high-resolution images of the membrane surface and three-dimensional images of the filtration channel are presented. These images were analysed with respect to particle deposition behaviour as characterised by deposition coverage as a function of filtration time and distance from the membrane surface.

Chapter 4 uses the microfluidic membrane system to investigate the effect of membrane-particle and particle-particle interaction energies on particle deposition over a range of pH and ionic strength conditions. The zeta potential of 0.4 μm latex particles and 10 kDa PES ultrafiltration membranes are measured at each condition. Using the measured zeta potential, an approach to determine the interaction energies of membrane-particle and particle-particle was developed by

incorporating DLVO theory, Van der Waals attraction energy, and modified Hogg-Healy-Fuersteneau (HHF) formula.

The influence of solution properties including pH, ionic strength, and feed concentration on membrane fouling during crossflow filtration is investigated in **Chapter 5**. Using the system developed in chapter 3, the deposition process could be visualised in real time. Differences in the microstructural characteristics of the deposit layers formed over a range of solution properties were revealed. Dynamic deposition behaviours were characterised in terms of surface coverage, deposition volume, and normalised deposition volume. The experimental results are interpreted in terms of the interplay of membrane-particle and particle-particle interactions to reveal the key mechanisms of membrane fouling by considering both interactions and the key roles of solution properties affecting on membrane fouling.

In **Chapter 6**, the microfluidic membrane system was used to investigate the influence of permeate flux and crossflow velocity on the deposition process during crossflow filtration. The direct visualisations of the deposition process and derived quantifications of deposition were obtained to better understand the fouling mechanisms as influenced by hydrodynamics. Building on the experimental results obtained from **Chapter 4**, **5**, and **6**, an empirical correlation describing the dynamic deposition volume was developed in terms of the membrane-particle and particle-particle interaction energies (governed by solution properties) and deposition probability (governed by hydrodynamic forces).

The entire work opens up new approaches for further research, and this is discussed in **Chapter 7** alongside conclusions drawn from this work. Future perspectives are stated in this chapter as well.

Chapter 2 A Review of Microstructural Measurements of Membrane Fouling during Filtration Processes

One of the challenges in the application of membrane filtration is the phenomenon of flux decline caused by concentration polarisation and membrane fouling, however, the underlying mechanisms has not yet been fully explained. In this chapter, the state-of-art techniques available for microstructural measurement of the particle deposition during membrane filtration are critically reviewed. The results from existing microstructural measurements are then discussed in relation to macroscopic flux measurements. The limitation of the current state of the art is identified. This establishes the increased capabilities and potential new applications of the method developed in this thesis.

This chapter is adapted from a manuscript in preparation for submission to a membrane science journal. Hongzhan Di, Gregory J. O. Martin, Dave E. Dunstan* "A review of microstructural measurements of membrane fouling during filtration processes".

2.1 Techniques for determining concentration profiles

Although the study of macroscopic flux performance has yielded significant insight into flux decline [42, 46, 72], it is important to develop microstructural measurements of the boundary layer to examine membrane fouling from a microscopic level [86, 87]. These measurements are categorised into three groups according to their ability to i) characterise concentration profiles, ii) determine the deposit layer thickness, and iii) visualising the membrane surface. The concentration profile refers to the variation in particle concentration as a function of the distance from the membrane surface (d) and the filtration time (t). This information is useful for understanding the microscopic structure of the boundary layer and to validate the predictions of theoretical models. Techniques for determining concentration profiles C (d, t) during membrane filtration have been summarised in Table 2-1 .

Table 2-1 Techniques for determining concentration profiles, *C* (*d, t)*

Technique	Principle	Filtration process	Membrane Type (pore size)	Applying solution	Distance to surface	Resolution	Variable conditions
Shadowgraph [88]	Light deflection	Dead-end UF	F-Cellulosic	BSA (M_W=10kDa)	200 µm	-	ΔP, pH
Refractometry [89-91]	Light deflection	Dead-end UF	F-PC (0.015 µm)	HA (M_W=605kDa)	20 µm	5 µm	C_0, v, IS
Electro diode array microscope (EDAM) [92, 93]	Light adsorption	Dead-end/Cross-flow MF/UF	F-PS, CA (0.01-1.0 µm)	DB,BSA (M_W=330kDa)	20 µm	2 µm	ΔP, C_0, v
Holographic interferometry[94-99]	Electromagnetic wave refraction	Dead-end/Cross-flow UF/RO	F-PES, CA	BSA PEG	0 µm	-	ΔP, C_0
Small-angle X-ray scattering (SAXS) [100-103]	Light scattering	Dead-end/Cross-flow UF	F-PS, PES (M_W=100kDa)	CM, Lp, SM	20 µm	20 µm	Ultrasonic

- UF = Ultrafiltration, MF = Microfiltration, RO = Reverse Osmosis;
- F = Flat sheet membrane; HF = Hollow fiber membrane; T = Tubular membrane;
- PC=polycarbonate membrane, CA=cellulose acetate membrane, PP=polypropylene, PA=polyamide membrane, PVDF= polyvinylidene fluoride membrane;
- M_W=molecular weight cut-off; BSA = bovine serum albumin; HA = hyaluronic acid; DB = dextran blue; CM = casein micelles; Lp = Laponite; SM = skim milk; OW = oil-water emulsions; Si = silica; PMMA = Poly (methyl methacrylate); Latex = polystyrene; SW8= submicron bacteria;
- ΔP = Transmembrane pressure/Transmembrane pressure; C_0 = Feed concentration; v = flow velocity; IS = ionic strength.

Figure 2-3 shows one example of concentration profiles measured using a system incorporating an electrodiode array microscope [92]. Generally, the concentration was shown to increase with increasing filtration time and decreasing distance from the membrane surface. Five techniques have been reported to be capable of determining concentration profiles: shadowgraph, refractometry, electro diode array microscope (EDAM), holographic interferometry, and small-angle X-ray scattering (SAXS).

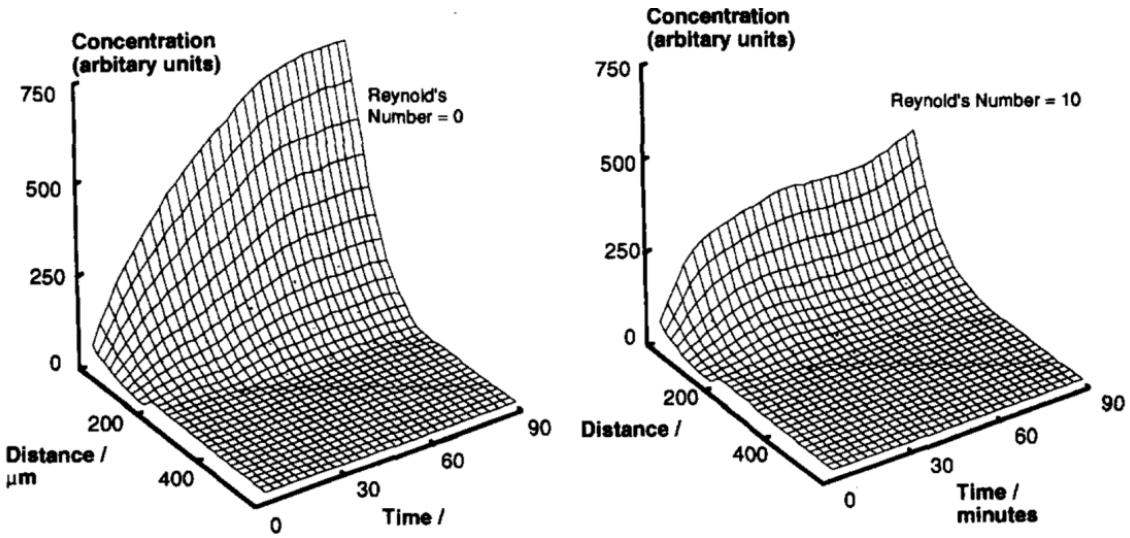

Figure 2-1 Concentration profiles C (d, t), concentration as a function of distance away the membrane surface and filtration time, obtained by electro diode array microscope (EDAM) under different cross flow rate (Re=0, and Re=10) by Mc Donogh et al. Increasing concentration is found with increasing time and decreasing distance [92].

2.1.1 Shadowgraph

Shadowgraph has been widely used in experimental fluid mechanics and heat transfer using a light source and a recording plane[104]. The density of a fluid varies with many factors, like temperature, and the index of refraction changes with fluid density. A light ray that travels through a fluid with variations in the refractive index will be deflected and bent out its original path, so that the position on the recording plane where the undeflected ray would arrive remains dark while the position where the deflected ray arrives appears bright. The resulted pattern of variations of

the illumination is thereby produced in the recording plane, which is proportional to the second derivative of the refractive index of the fluid.

Vilker et al. [88] used this technique to determine the concentration gradient of bovine serum albumin (BSA) during dead-end ultrafiltration (weight cut-off of the membrane was 10 kDa). During the filtration process, a refractive index gradient occurred in the concentration polarization layer, which deflected the lights passing through the fluid and resulted in the visible pattern on the recording plane (Figure 2-2). By measuring the extent of light deflection, the refractive index could be obtained and used to determine the concentration profiles. A linear correlation between the concentration of BSA and its refractive index was derived. This correlation was valid up to 580 g/L, which limited the minimum distance from membrane surface to 200 μm. Concentration values at distance less than 200 μm were obtained by extrapolation of the concentration profiles.

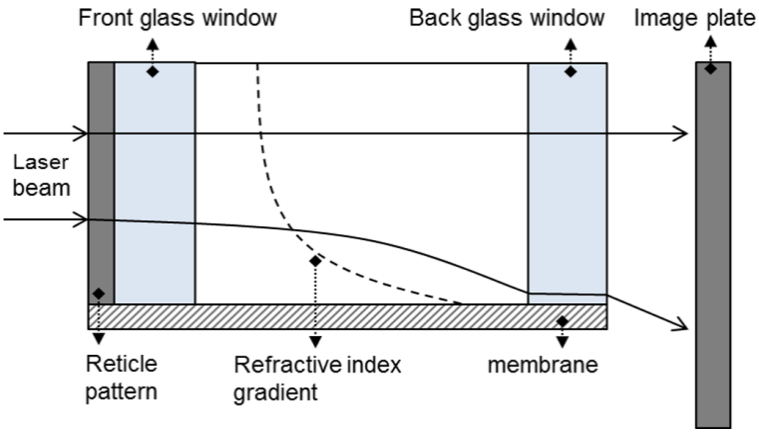

Figure 2-2 Schematic diagram of the light paths (solid line) and refractive index gradient (dashed line) of shadowgraph technique. Laser light is deflected and bends out its original path due to the variations in the refractive index in a fluid. The changes of illumination positions are captured by the image plate. Adapted from Vilker et al [88].

Using shadowgraphy, Vilker et al. obtained the concentration profiles of BSA at different distances from membrane surface during dead-end ultrafiltration. Their results provided direct evidence to study the effects of transmembrane pressure and pH on the boundary layer (see further elaborate in section 2.4). Additionally, the experimental data was used to verify theoretical predictions they proposed. However, there are some limitations in their work. The minimum

distance from the membrane surface at which the concentration could be obtained was 200 µm. The deflection of light near the membrane surface is bent towards the membrane surface, resulting in no deflection on the image plate. Thus, the concentration values at distances less than 200 µm are extrapolated from the profile data rather than experimental results. Additionally, although the experimental data fitted well with the theoretical predictions they proposed, it should be noted that the diffusivity values are chosen manually to get a good fit, and were greater than the calculated diffusivity values.

2.1.2 Refractometry

The Refractometry was developed to study the concentration profiles during dead-end ultrafiltration of a biopolymer, hyaluronic acid (HA) by Ethier and Lin [89], and later improved by Gowman and Ethier [90, 91]. Membranes with a pore size of 0.015 µm and hyaluronic acid with a molecular weight cut-offof 605 kDa were used. Similar to the shadowgraph technique, refractometry is also based on the light reflection caused by a refractive index gradient. The difference is that the concentration profile is determined from calibration with known samples.. The details of the experimental apparatus are provided by Gowman and Ethier [90]. Two hydraulically independent chambers were used. The left side is a reference, and the right side contains the biopolymer. Both sides were initially filled with solvent only (water) to determine the laser beam reference position, and then the biopolymer side was replaced by HA solution. The new deflection position caused by the increased refractive index was used to determine the concentration (Figure 2-3).

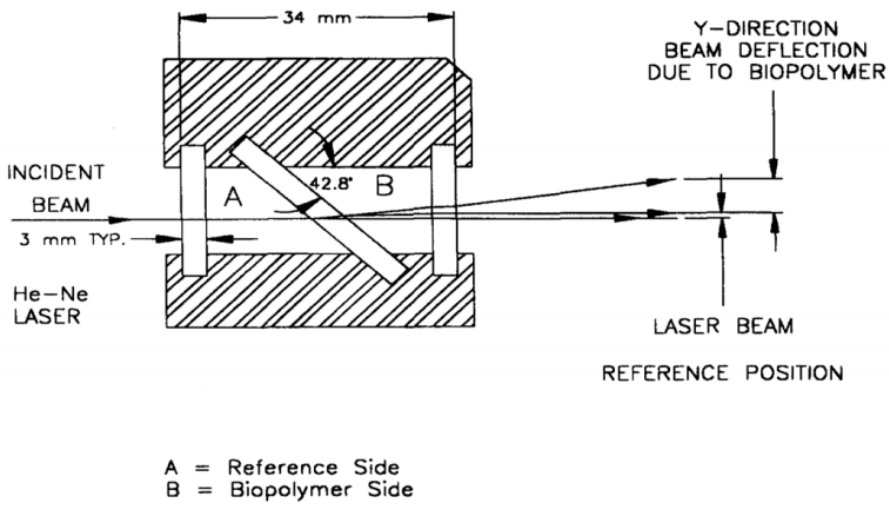

Figure 2-3 Cross-section of the flow cell used for refractometry. A is the reference side, and B is the biopolymer side. The beam travelling through B is deflected to the new position due to the varied refractive index [90].

The method showed an increase in the concentration with decreasing distance from the membrane in studies of the effects of feed concentration, flow velocity, and ionic strength on the concentration polarisation layer (see section 2.4 for further elaboration). However, some restrictions also exist for this technique. Firstly, the minimum distance from membrane is 200 µm due to the finite thickness of the laser beam, the necessity of a sealing gasket, and a slight bevel on the flow cell. In their results, the concentration at the membrane surface C_m is actually the concentration at a distance of 200 µm from the membrane surface. This limits the study of the deposition of sub-micron sized particles. Additionally, this technique requires that the concentration polarisation layer is quite thick (around 4 mm) to allow detailed spatial resolution. As such, this technique can only be used for dead-end filtration and crossflow filtration at low velocity, for which the polarisation layer is sufficiently thick.

2.1.3 Electro diode array microscope (EDAM)

Mc Donogh et al. [92, 93] utilised an electro diode array microscope (EDAM) technique to observe concentration polarisation during the ultrafiltration and microfiltration of dextran blue and BSA solutions. The principle is that infrared light is partially adsorbed when passed through

a concentration polarisation layer. The light passing out of the filtration device is detected by an array of micro-diodes, each of which registers a slice of the transmitted light. Quantifications can be made by determining the typical signals from the micro-diode detectors in response to the channel being filled by the solute at known concentrations prior to filtration. Through this calibration, the signal from each diode gives the concentration of species in the sampled slice. Their results showed that higher concentrations could be observed closer to the membrane surface, and that the concentration increased with time and reached a limiting value at a given distance. The effects of transmembrane pressure, feed concentration, and crossflow velocity were tested in their works (see section 2.4 for further elaboration). The minimum measurement distance from membrane was improved over shadowgraph and refractometery methods described above, however it was still limited to 20 µm.

2.1.4 Holographic interferometry

The principle of holographic interferometry is that that electromagnetic waves (632.8nm) emitted from the He-Ne laser beam will bend in the optical path due to changes in the refractive index of a medium. Changes in the optical path can be visualised as interference fringe patterns. In the case of the appearance of concentration polarization layer or fouling layer during filtration process, the changes in the concentration distribution resulting in the changes of refractive index can be obtained as an interference fringe pattern [96].

A schematic of a setup for investigating ultrafiltration using holographic interferometry is shown in Figure 2-4. The gradient of the refractive index of the solution can be obtained by following the evolution of the interference fringes, and a linear relation between the refractive index and the solution concentration can be experimentally obtained. Fernandez-Torres and Fernández-Sempere et al. [94-99] carried out a series of studies of the boundary layer under various conditions, including different feed solutions (bovine serum albumin BSA and polyethylene glycol PEG), membrane materials (polyethersulfone PES and cellulose acetate CA), filtration modes (dead-end and crossflow), and filtration processes (ultrafiltration UF and reverse osmosis RO) using this technique. Their results allowed visualisation of the membrane surface, measurements of concentration profiles, and determination of the effects of different

transmembrane pressures and feed concentrations (see section 2.4 for further elaboration). The scale of resolution of an observation of interference fringes depends on the wave length of the applied signal. The approximate resolution of holographic interferometry technique is limited to be 20 µm. The other drawback of the technique is the complexity to set up and assemble the holographic interferometry system.

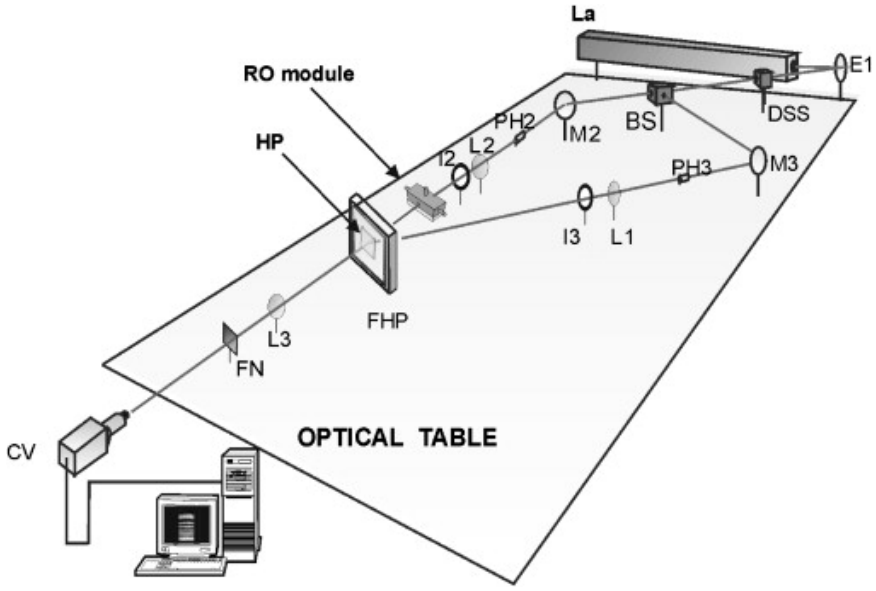

Figure 2-4 Schematic of holographic interferometry. The laser beam is divided in two by means of a varable beam splitter (BS). The direction of two beams is modified by two mirrors, M2 and M3, respectively. One of the beams illuminates the RO module and the light spread out is recorded by the holographic plate (HP). The other beam acts as a reference and is also recorded by HP. All of this image information is collected by video camera (VC) [96].

2.1.5 Small-angle X-ray scattering

David et al. [100-103] introduced a small-angle X-ray scattering (SAXS) technique to study the concentration profiles during dead end ultrafiltration of casein micelle (50-200 nm protein aggregates in milk) suspensions. A specific SAXS filtration cell was made of transparent polycarbonate and embedded into a flat polysulfone ultrafiltration membrane (Figure 2-5). The principle of SAXS is that when x-ray beams pass through samples, the scattering caused by the presence of particles can be measured at very low angles. By analysing the 2D scattering patterns as a function of distance from the membrane surface, the scattering intensities I(q) in absolute

units can be obtained and then used to deduce the concentration of particles (e.g. casein micelles). In order to ensure that the scattering intensity only corresponded to the casein micelles, the minimum distance from membrane surface was determined to be 280 µm, at distance at which the scattering and adsorption signal were not influenced by the membrane or polycarbonate support [100]. The temporal evolution of concentration profiles at different distances from the membrane surface during dead-end filtration of casein micelles was reported. The values were deduced from azimuthally averaged scattering intensities in absolute units, and presented as the mean concentration in a layer of ± 50 µm around the measured height (H).

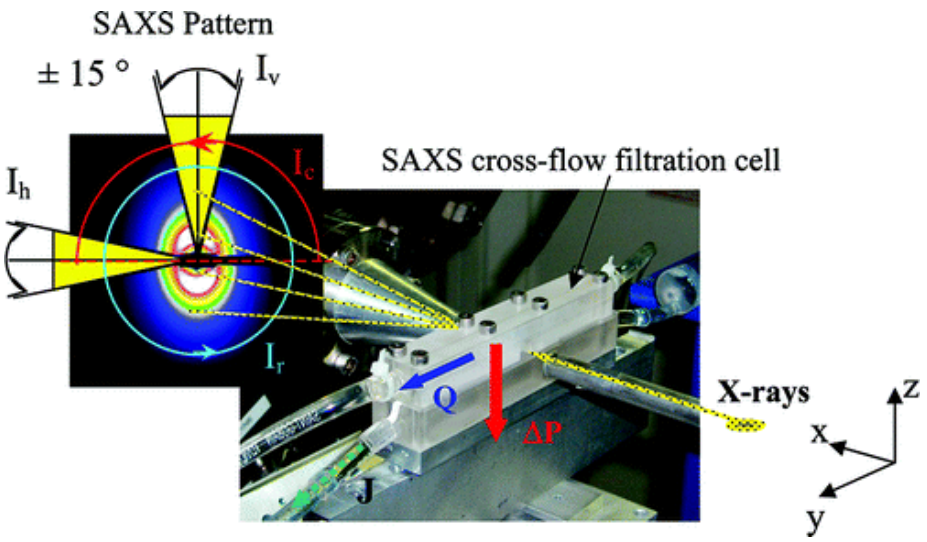

Figure 2-5 Picture of the SAXS cross-flow filtration cell. X-ray beams travel through a cross section of a crossflow filtration cell. Scattering patterns caused by the presence of particles in the flow are recorded [101].

The same research group continued investigating the concentration profiles during crossflow ultrafiltration of laptonite dispersions [101]. The minimum measurement distance from the membrane surface was reduced to 100 µm through the use of an angular motion stage. Their results of concentration profiles C (*d*) were used to verify an osmotic pressure model proposed by Bouchoux et al. [105]. The model was able to predict the filtration performances in relation with operating conditions. The effects of ultrasound on ultrafiltration of laptonite dispersions [102] and skim milk [103] during crossflow filtration were also reported using this technique. The minimum

distance above the membrane surface was further reduced to 20 by 80 µm. The ultrasonication was proposed to act as an additional disaggregation force that prevented accumulation in the concentration polarisation layer near the membrane surface, leading to a complete removal of deposit layer.

The SAXS technique has been demonstrated capable of achieving in-situ characterisation of concentration profiles near the membrane surface. This has provided a new connection between macroscopic measurements, like permeate flux, and micro-characteristics (see section 2.4 for further elaboration). The concentration profiles are important for the verification of model predictions [105]. However, the minimum distance from membrane surface is still limited to 20 µm because the scattering is influenced by the other parts of the filtration cell below this distance. The absence of concentration information closer to the membrane surface (i.e. less than 20µm) reduces the ability to fully validate theoretical predictions.

2.2 Techniques for determining the boundary layer thickness

Many researchers have reported techniques for determining the thickness of the deposit layer, concentration polarisation layer, or cake layer during membrane filtration [35-53]. Although the definitions of the measured layer are seemingly different, in fact the “layer” can be simply considered as the boundary layer between the membrane surface and the bulk. In this discussion, all references to these layers are referred to as the boundary layer. Details of techniques that have been reported for determining the boundary layer thickness have been summarised in Table 2-2.

Table 2-2 Techniques for determining boundary layer thickness

Technique	Principle	Filtration process	Membrane Type (pore size)	Applying solution	Distance to surface	Resolution	Variable conditions
Nuclear magnetic resonance (NMR) [106-109]	Chemical shift	Cross-flow MF	HF-PP (0.2 µm), T-PP(0.2-0.4 µm)	Silica (12 nm)	0 µm	-	ΔP, C_0, v
Laser triangulometry[110, 111]	Light reflection	Cross-flow MF	F-PA (0.2 µm), F-PS (M_W=100kDa)	Earth (1-40 µm) Silica, Clay	20 µm	3 µm	-
Optical laser sensor [112]	Light adsorption	Cross-flow MF	T-(0.2 µm)	Bentonite (2.45 µm)	0 µm	-	ΔP, C_0, v
Photointerrupter sensor [113]	Light reflection	Cross-flow	F	PMMA (5.15 µm)	10 µm	10 µm	-
Ultrasonic time-domain refractometry (UTDR) [114-117]	Acoustic reflection	Cross-flow MF	F-Nylon(0.2 µm) F-PS (M_W=35kDa)	Kaolin (2 µm), Paper-mill, BSA	0 µm	-	*p*H
Direct observation (DO) [74, 75, 118-120]	optical	Cross-flow MF	HF-PVDF (0.1, 0.22 µm)	Bentonite (2.5, 2.8 µm)	0 µm	-	v
Microfluidic membrane chip [83, 84]	optical	Cross-flow MF	Membrane chip (1.5-8 µm)	Latex particles (6, 3.3, 5.7 µm)	0 µm	-	-

- MF = Microfiltration;
- F = Flat sheet membrane; HF = Hollow fiber membrane; T = Tubular membrane;
- PP=Polypropylene, PA=Polyamide membrane, PS= Polystyrene, PVDF= polyvinylidene fluoride membrane;
- M_W=molecular weight cut-off; BSA = bovine serum albumin; PMMA = Poly (methyl methacrylate);
- ΔP = Transmembrane pressure/Transmembrane pressure; C_0 = Feed concentration; v = flow velocity.

2.2.1 Nuclear magnetic resonance (NMR) micro-imaging

Nuclear magnetic resonance (NMR) is commonly used in medical and clinical radiology applications for non-invasive measurements, which involves the excitation and relaxation of protons in a specimen under the influence of an external magnetic field.When the fluid sample is placed in a powerful, static magnetic field, magnetized protons within the sample behave as magnets aligning parallel or anti-paralle with the magnetic field. By adding a radio frequency magnetic filed perpendicular to the main field, protons absorb energy and change their alignment with the magnetic field. As the protons return from excitation to the equilibrium state, a signal induced in the receiver coil of the instrument by the nuclear magnetization can then be transformed by a series of algorithms into diagnostic images. The detailed principles of NMR imaging can be found in a number of papers [121-123]. Yao et al. [106, 107] introduced this technique to the study of concentration polarisation layer thicknesses during the filtration of oil-water emulsions in hollow fiber membranes. Using the same technique, quantative measurements during the filtration of oil-water emulsions and colloidal silica particles in single tubular membranes were obtained by Pope et al. [108] and Airey et al. [109] respectively. Pope et al. studied the effects of transmembrane pressure and crossflow velocity while Airey et al. reported the measurements of the fluidity of the polarisation layers, which were obtained from 2D cross sectional velocity distribution maps using the q-space imaging or dynamic NMR microscopy. According to their results, the discernible particle motion was only observed from approximately half the layer thickness to bulk solutions. This could be explained by the presence of a stagnant layer and dynamic layer, similar to the results from Marselina et al. [74, 75] (further elaborated in section 2.4). There is also a resolution limit for the NMR technique which is around 10 μm.

2.2.2 Laser triangulometry

Triangulation has been used to measure the deposit layer thickness based on shifts in the reflection of laser beam, when it is directed onto a surface of varying elevation, a developing cake layer for instance. The reflected laser beam off the surface is then captured by a charge coupled

device (CCD camera), and the location where the reflected beam arrives shift as the cake layer surface changes, which can be used to estimate the thickness of the cake layer (Figure 2-6). Using this method, Altmann and Ripperger [110] monitored the build-up of a cake layer during crossflow microfiltration of diatomaceous earth and silica particles. A similar method was reported by Mendret et al. [111]. A laser sheet instead of a single laser beam was used to enable measurements of layer growth at several locations along the membrane. The layer thickness could be determined from 10 microns to hundreds of microns at a resolution of 3 μm during dead-end ultrafiltration of clay suspensions in inside-out hollow fibre membranes. They could show an increase in the thickness as a function of filtration time, and that the cake thickness was inhomogeneous along the channel. The resolution for this technique is around 5 μm, thus the accuracy for thin cake layer (<5 μm) is restricted.

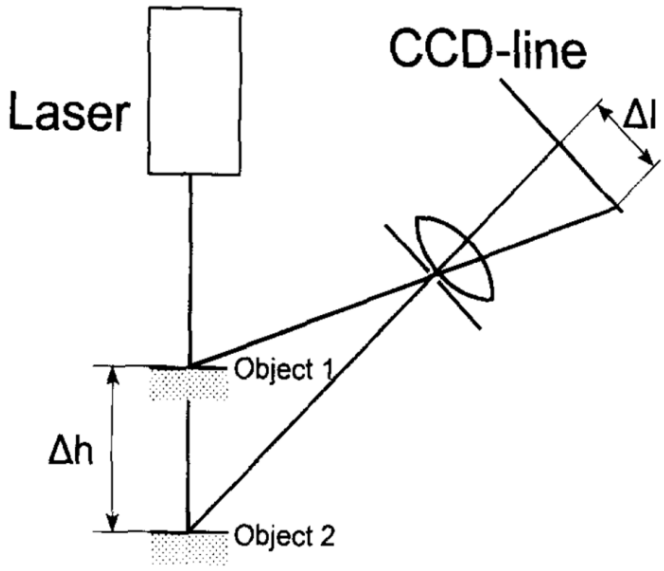

Figure 2-6 Schematic of the principle of laser triangulometry. Object 1 refers to the cake layer thickness, and object 2 refers to the membrane surface. The reflected laser beams are captured by CCD camera [110].

2.2.3 Optical laser sensor

The principle of optical laser sensor technique is based on the light absorption by the cake layer. When a laser beam passes through a tested region, the formation of the cake layer will absorb light and the variation of the signal intensity detected corresponds to the layer thickness. A

calibration curve with known values of cake layer thickness is performed to extract the correlation. Hamachi et al. [112] used this technique to study the deposit thickness during crossflow microfiltration of bentonite. The time-dependent deposit thicknesses under various transmembrane pressure, feed concentration, and crossflow velocities were reported (see section 2.4 for further elaboration). Consistent with the results from Mendret et al. [111], they found the deposit was not homogeneous along the length of the membrane. One limitation of this technique is the solution concentration that a laser with higher power rating is required for working with a higher concentration.

2.2.4 Photointerrupter sensor

Tung et al. [113] used a photointerrupter sensor to determine the boundary layer thickness of a PMMA suspension (particle size of approximately 5 μm) during crossflow microfiltration. A high sensitivity reflective type sub-miniature photo interrupter sensor was located on the top of the membrane surface. The light from the emitter was reflected by the surface of the membrane/deposit layer, and detected by the sensor (Figure 2-7). Decreasing the distance between the object and sensor induces an increase in the reflective current, allowing measurement of the boundary layer thickness. The upper plate was made from transparent plexiglass. The effects of slurry colour, slurry concentration, slurry transport rate, and background light on the accuracy of the technique were determined. Slurry colour was found to be the most continual problem, but the effect could be eliminated after calibration. The slurry transport rate and background light were found to have little effect on the accuracy of the system. This technique allowed measurement of the layer thickness between 10 μm to 5 mm at a resolution of 10 μm.

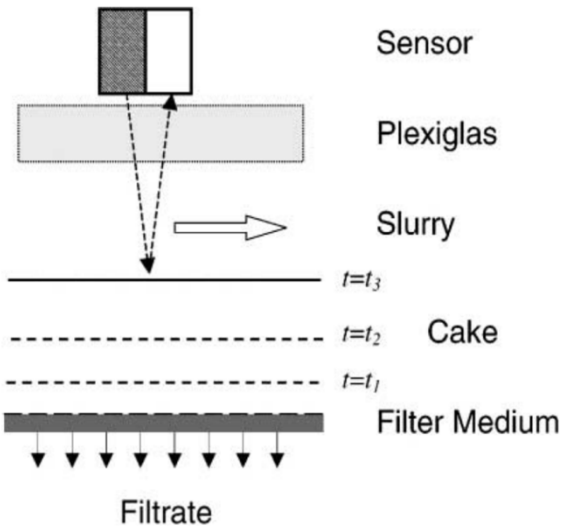

Figure 2-7 Schematic diagram of cake layer thickness measurement by a photointerrupter sensor. The emitted light is reflected by the surface of the membrane or the cake layer, and then detected by the sensor [113].

2.2.5 Ultrasonic time-domain refractometry (UTDR)

The ultrasonic time-domain refractometry (UTDR) technique is based on the principle that a partial reflection of an acoustic wave occurs when ultrasonic waves encounter an interface between two different media. Based on the difference in the amplitude and arrival times at different distances, each reflection wave can be distinguished by an ultrasonic transducer (Figure 2-8). The UTDR technique has been used to study the membrane fouling during reverse osmosis of calcium sulfate solutions [124] and the effects of membrane compaction on flux decline during gas separation [125]. Li et al. used this technique to study the deposit growth during crossflow filtration of Kaolin suspensions [115], paper-mill effluent[114, 117], and BSA solutions [116] using various membranes. A rectangular flat-bed filtration module with a flow channel of 100 mm × 20 mm × 2.5 mm was used in their works. This technique allowed detection of the dynamic growth of the fouling-layer under variable pH [116], and monitoring of the efficiency of different cleaning methods [114, 115]. This technique is limited to measure thick deposit layer since the layer has to be thick enough for the ultrasonic signals to present a new echo at the interface between the bulk flow and deposit layer.

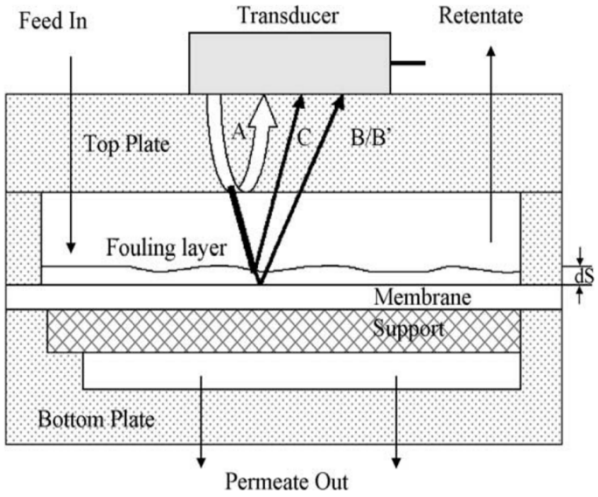

Figure 2-8 Schematic principle of Ultrasonic time-domain refrectometry technique. In a crossflow filtration cell, ultrasonic waves encounter the surfaces of the fouling layer and the membrane, and are reflected at different distances with different amplitude and arrivals times [114].

2.2.6 Direct microscopic observation

Marselina et al. [74, 75] used a microscope and a video camera to directly visualise the deposit growth and removal in real time during crossflow filtration of bentonite in inside-out hollow fibre membranes. Their setup consisted of a modified crossflow membrane module, a microscope and a video camera, as showen in Figure 2-9. The top part of the filtration module had a glass window (65 mm× 20 mm) as a viewing port. The distance from the viewing port to the center of the membrane was 1.3 mm. A 10-times magnification objective lens was used to monitor the layer growth. A polyvinylidene fluoride (PVDF) hollow fiber membrane with an outside diameter of 0.65 mm and a length of 155 mm was used in their works. The normal pore size was 0.1 and 0.22 μm for the bentonite solutions with particle size of 2.5 and 2.8 μm, respectively. This technique provided direct observation of the layer formation and thickness. Similar direct observation techniques have been reported by other researchers. Romero et al. used a cathetometer to measure the boundary layer thickness in a rectangular glass-walled filter during the crossflow microfiltration of polystyrene suspensions with a size range of 48-150 μm. The membranes used were polycarbonate sheets with pore sizes between 0.2 and 1.0 μm [118]. Mackley et al. used a

15-times magnification video camera to observe and measure the layer formation and growth during crossflow microfiltration. The polystyrene suspensions with a size range of 125-180 μm and a stainless steel filter mesh (90 × 90 μm) were used in their studies [119]. Wakeman et al. used a high-speed camera with high-magnification zoom lens to observe the layer growth during crossflow microfiltration of suspensions with a particle size of 2.6 μm [120]. All of these research groups were able to observe an increase in the deposit layer thickness as a function of filtration time. Marselina et al. also studied the effect of crossflow velocity on fouling layer thickness [48]. Thinner fouling layers were obtained at higher flow velocities (further elaborated in section 2.4). They also investigated two cleaning methods, crossflow shear and backwashing. The latter method only took half the time of the former to clean the membrane.

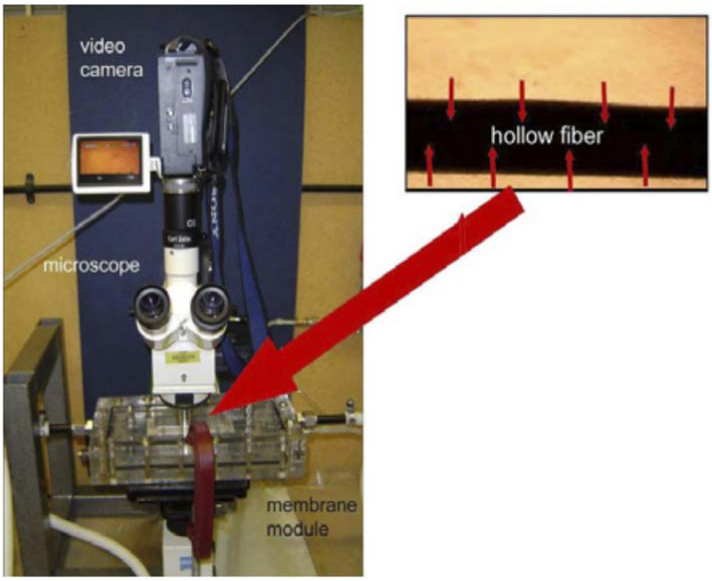

Figure 2-9 Picture of the direct observation experimental setup comprising of a hollow fiber membrane module, a microscope, and a video camera. The upper right corner of the image shows that the dark area is the observed hollow fiber [75].

2.2.7 Microfluidic membrane chip

Ngene et al. used another direct observation method to characterise the fouling process during microfiltration of polystyrene solutions [83, 84]. A specific microfluidic membrane chip with embedded channels separated by a porous structure (active membrane) was fabricated in their

works. Polyetherimide (PEI), polyvinylpyrrolidone (PVP), N-methylpyrrolidone (NMP), and square-shaped fused silica capillaries were used to fabricate the membrane with embedded channels. A camera attached to the magnifying lenses was used for observation. The pore size of the fabricated membranes was observed to be 3-8 μm and 1.5 μm. The filtration length was around 2 mm. An image of the channels on the microfluidic chip is shown in Figure 2-10. Ngene et al. operated filtration experiments using both mono disperse polystyrene particles (6 μm) and bi-disperse suspensions (3.3 and 5.7 μm). An increase in the cake thickness was observed during filtration time, as well as an increase in the proportion of the larger particles (5.7 μm) in the cake. They also investigated the average cake porosity and specific cake resistance as a function of larger particle fraction. The theoretical cake porosity was determined by Tokumistsu method [79]. And the experimental data showed good agreement to that of theoretical predictions. This technique is limited to the fabricated specific membranes and experimental measurements produced on commercial filtration membranes cannot be accessed.

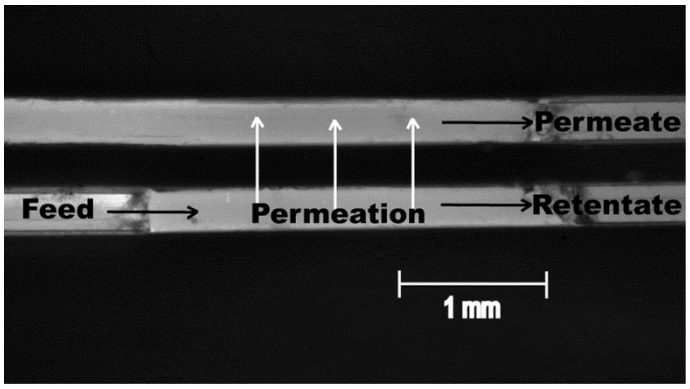

Figure 2-10 Chip showing channels and flow directions. The active membrane is between the retentate channel (lower bright rectangle area) and the permeate channel (upper bright rectangle area) [46].

2.3 Techniques for visualising the membrane surface

In addition to those developed techniques determining the concentration profiles and cake layer thickness, techniques using optical microscopy for visualizing the membrane surface have also been developed (Table 2-3).

2.3.1 Direct observation through the membrane (DOTM)

Direct observation through the membrane (DOTM) is a technique that allows the membrane surface to be visualised during the filtration processes that was initially developed by Hodgson et al. [134]. A microscope was mounted on the permeate side of a transparent membrane (Anopore anodised-alumina membrane with pore size of 0.02 μm) to observe fouling as it occurred on the membrane surface (Figure 2-11). Li et al. [76, 126, 127] continued DOTM investigations on the crossflow microfiltration of suspensions of yeast, latex beads, and submicron-sized bacteria. Images obtained by DOTM, revealed that more particles continued to be deposited on the membrane surface during filtration. Also, particles were seen to tend to deposit on the membrane surface where other particles had already been deposited. Additionally, the critical flux determined from the images was found to have a positive correlation with particle size and crossflow velocity. As this technique used a microscope to visualize the membrane surface, the resolution limitation of optical microscopy existed and restricted high-resolution observations on smaller particles.

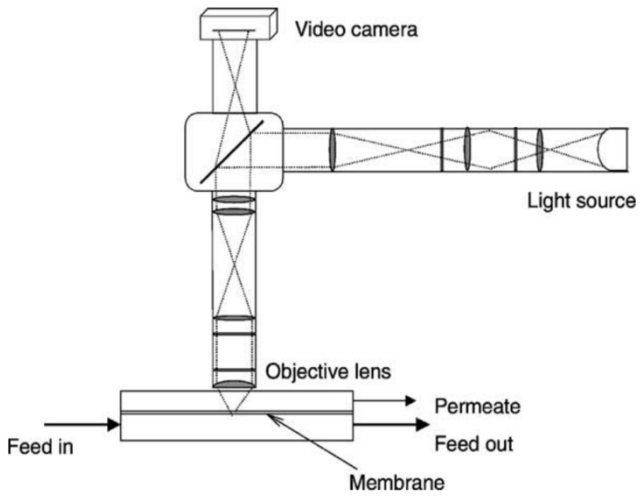

Figure 2-11 Schematic of direct observation through the membrane (DOTM) apparatus. Microscope lens locates on the permeate side of a transparent membrane in a cross filtration cell to observe the fouling process on the membrane, and visualization information is recorded by a video camera [127].

Table 2-3 Techniques for visualising the membrane surface

Technique	Principle	Filtration process	Membrane Type (pore size)	Applying solution	Distance to the surface	Resol ution	Variable conditions
Direct observation through the membrane (DOTM)[76, 126, 127]	Optical Microscopy	Cross-flow MF	F-AN (0.02 µm)	Yeast(5 µm) Latex (3-12 µm) SW8 (0.6 µm)	0 µm	-	-
Direct visual observation (DVO) [77]	Optical Microscopy	Cross-flow MF	F-CA(0.22 µm) F-AN(0.2 µm)	Yeast	0 µm	-	-
Confocal scanning laser microscopy (CSLM) [78, 128-131]	Optical Microscopy	Cross-flow MF/UF	F-PC(0.22 µm)	BSA, Latex particles	0 µm	-	-
Microfluidic channels and sieves [79-82, 132, 133]	Optical microscopy, Microfluidics	Cross-flow/ Dead-end, MF	Mimic membranes (PDMS, 5-20 µm)	Latex particles Microgels (2-8 µm)	0 µm	-	Ionic Strength, Pore geometry, Crossflow velocity.

- UF = Ultrafiltration, MF = Microfiltration, NF = Nanofiltration, RO = Reverse Osmosis;
- F = Flat sheet membrane;
- CA=cellulose acetate membrane, PC , AN;
- BSA = bovine serum albumin; SW8= submicron bacteria

2.3.2 Direct visual observation (DVO)

Mores et al. [77] developed the so-called direct visual observation (DVO) technique to observe the microfiltration of yeast using cellulose-acetate (CA, pore size 0.22 μm) and anopore anodised-alumina (AN, pore size 0.2 μm) membranes. Different to the DOTM, a microscope was mounted on the feed side of the membrane (Figure 2-12). During filtration, particles deposited on the AN membranes were more uniformly distributed than those on the CA membranes. After cleaning however, most of the AN membranes remained covered in a monolayer (70% flux recovery), whereas cleaning removed most of the initial deposit from the CA membranes (90% flux recovery). This method was used to show that yeast cells exhibited greater adhesion to the AN membranes than the CA membranes. Similar to DOTM technique, the resolution limitation of the microscope also existed in DVO techniques.

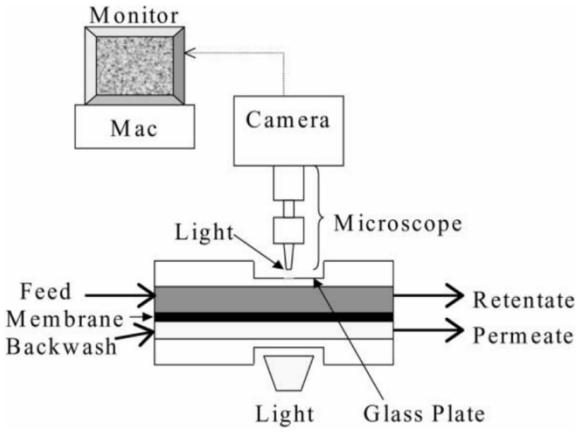

Figure 2-12 Schematic of direct visual observation (DVO) apparatus. Microscope is mounted on the retentate side of the membrane in a crossflow filtration cell. The fouling process is recorded by a camera [77].

2.3.3 Confocal scanning laser microscopy (CSLM)

The technique of confocal scanning laser microscopy (CSLM) has been developed and applied to the characterisation of membrane fouling in the last two decades. Compared to normal microscopy, CSLM has many advantages such as higher resolution imaging and 3D reconstructions. In a laser scanning confocal microscope, a laser beam illuminates a pinhole and is then focused through the objective lens into a fluorescent specimen. The background

information away from the focal plane is weakly transmitted through the detector pinhole, which enhances the detected signal from the exact focal plane. The specimen is scanned pixel by pixel and the light is collected to produce an image of the specimen.

CSLM technique has been applied to visualize the deposition on the membrane surface in different filtration modes, including microfiltration [78, 128], ultrafiltration [129], and reverse/forward osmosis [130, 131]. However, most of literatures only provided images of the membrane surface, further characterizations of the deposit layer such as the layer structure and deposition distribution, and other analyses of the deposition behaviours as influenced by factors pH for instance have not been addressed.

2.3.4 Microfluidic channels and sieves

More recently, microfluidic technology has been combined with optical microscopy to study particle deposition and fouling during membrane filtration. Microfluidics provides the ability to create well-defined and customised geometries that can mimic the pore structures of microfiltration membranes. Using micro-sieves to mimic a flat membrane surface structure, the top view of the 'membrane' surface could be obtained [132]. Using parallel micro-channels to mimic pore walls, particle clogging at the pore entrance could be visualised. Van De Laar et al. investigated the influence of pore geometry and particle interactions on the clogging behaviour [133]. The group of Weitz found that the clogging depended on the ratio of the pore size to particle size [80]. In later work, they reported that the particle clogging behaviour was influenced by the channel geometry and shear stress[82]. Using similar parallel micro-channels, Linkhorst et al. studied fast jamming of colloidal particles as well as particle translocation at the single particle level [79]. By varying the ionic strength in the feed latex solutions, Bacchin et al. studied the influence of colloidal interactions on the clogging behaviour. Latex particles were observed to form dendrites at the pore entrance in solutions containing 0.1 M KCl, whereas more gradual obstruction was found when the latex particles were suspended in ultrapure water [81].

In summary, the use of the microfluidic channels and sieves has enabled visualisation and detailed investigation into particle clogging at the scale of microfiltration pores (pore entrance size 5-20

μm). However, these reported works are limited to the study of particles with a diameter of at least several microns. A major limitation to the work done to date is that submicron particles in the ultrafiltration range cannot be examined. In addition, all the above research was done using microfluidic channels as membrane mimics, and the study of deposition on real commercial porous membranes cannot be performed.

2.4 Effects of influencing factors on microstructural measurements of the boundary layer

In the filtration channel, three regions can be distinguished with respect to distance from the membrane surface: the fouling layer, the concentration polarisation layer, and the bulk flow. Combined, the fouling and CP layers are defined as the boundary layer. Using the techniques summarised in the section above, the boundary layer has be observed and studied, providing some understanding of the microstructural characteristics. The fouling layer can be considered to have a relatively compact structure, and can also be referred to as the cake layer, gel layer or stagnant layer in different reports. The distance-dependent concentration is supposed to change slowly due to the compact structure of the fouling layer, and the concentration at the membrane surface C_m is much higher compared to the feed concentration C_0. Above this region is the concentration polarisation layer, which has been referred to as a dynamic layer or fluidised layer. In comparison to the fouling layer, the concentration varies strongly as a function of distance away from the membrane. This can be explained by the relatively free movement of the particles. The third region is the bulk flow, that has the same concentration as the original feed, C_0 (Figure 2-13).

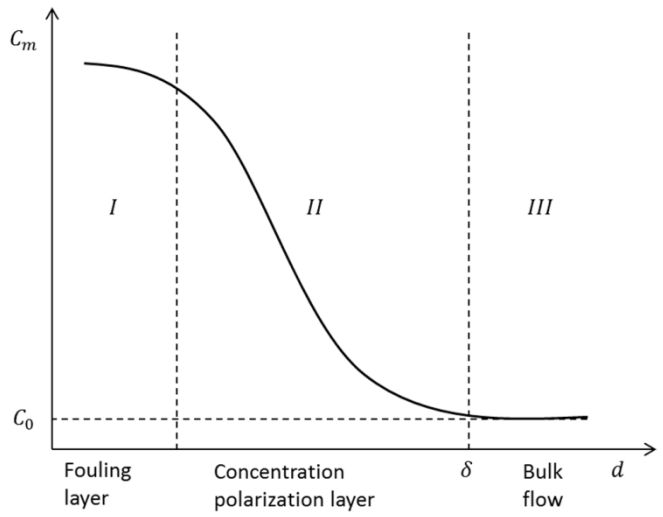

Figure 2-13 Schematic diagram of the distance-dependent concentration profile. Region I is the fouling layer with gradual concentration change. Region II is the concentration polarisation layer with a relatively dramatic concentration change. Region III is the bulk flow with the feed concentration. C_m = concentration at the membrane surface. C_0 = feed concentration. d = distance from the membrane surface. δ = boundary layer thickness.

This section reviews the current knowledge of the effects of filtration variables on microstructural measurements of the boundary layer. Concentration at the membrane surface C_m and the boundary layer thickness δ are the representative parameters. To better understand how the variable conditions influence the filtration processes, both microstructural measurements (C_m, δ) and macroscopic flux performance (rate of flux decline and limiting flux J_∞) have been summarised in Table 2-5.

Table 2-4 Effects of variable conditions on the microstructural and macroscopic measurements

Variable conditions		**Microstructural measurements**		**Effect on macroscopic flux performance**
		Concentration at the membrane surface, C_m	**The boundary layer thickness, δ**	
Transmembrane pressure ΔP	Higher	Higher [88, 92]	Thicker [92, 108, 112]	Higher J_∞, slow drop [135-138]
Feed concentration C_0	Higher	Higher [91] Slightly higher [92]	Thicker [91, 109, 112] Thinner [92]	Lower (little effect) J_∞ [42-44, 49]; Rapid drop [42-44, 49]
Flow velocity v	Higher	Higher [91] Lower [92]	Thinner [91, 92] Thinner [74, 108, 112]	Higher J_∞, slow drop [42, 43, 139]
Ionic strength IS	Higher	Higher [91]	Thinner [91]	Lower J_∞, rapid drop [37, 41, 47, 140]
***p*H**	IEP	Highest [88]	Thinnest [116]	Lowest J_∞, rapid drop [40, 45]

- IEP= isoelectric point
- J_∞ = the limit flux

2.4.1 Effect of transmembrane pressure

Using shadowgraph and EDAM techniques, the concentration at the membrane surface (C_m) has been observed to increase with increasing transmembrane pressure during the dead-end ultrafiltration by Vilker et al. [88] and Mc Donogh et al. [92]. Due to the 200 μm limitation in the minimum distance from the membrane surface using this technique, C_m was extrapolated from the concentration profiles [88]. While in the work of Mc Donogh et al., C_m represented the concentration at a distance of 20 μm from the membrane surface. Mc Donogh et al. [108, 112] also found that the boundary layer thickness (δ) increased with increasing TMP, which was consistent with other studies [19, 35, 38]. The effect of transmembrane pressure on the microstructural measurements is shown in the dashed curve 1 of Figure 2-14, where greater concentration at the membrane surface and thicker deposit layer were observed as transmembrane pressure increased. This trend could be explained by that higher transmembrane pressure induced a greater amount of solute particles to be brought towards the membrane surface per unit time. Thus, proportionally more particles were rejected by the membrane (higher C_m), which caused the higher concentration polarisation near the membrane surface (higher δ) [43, 136-138]. Increasing the applied pressure also resulted in an increased convective force, which might be the reason for the increasing initial flux (J_0) and limiting flux (J_∞) [72, 73].

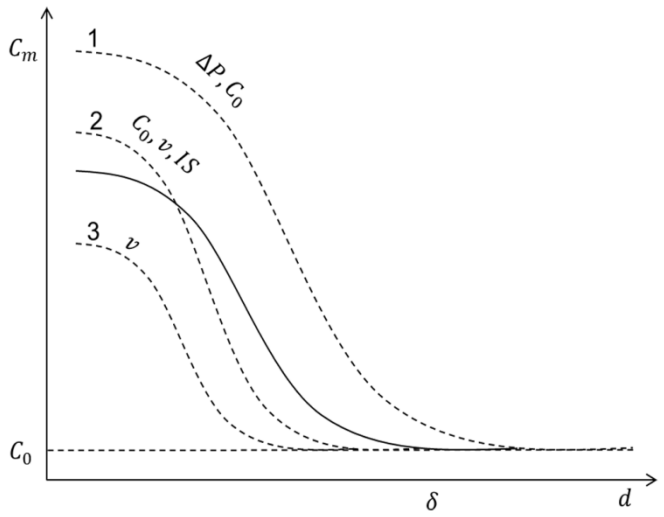

Figure 2-14 Effects of variable conditions on microstructural measurements of the boundary layer. C_m = concentration at the membrane surface. C_0 = feed concentration. d = distance from the membrane surface. Solid curve stands for the reference curve. Dashed curve 1 (higher C_m, higher δ), curve 2 (higher C_m, lower δ), and curve 3 (lower C_m, lower δ) stands for three different cases under variable conditions.

2.4.2 Effect of feed concentration

Gowman et al. [91] studied the concentration profiles and boundary layer thickness during dead-end ultrafiltration of HA solutions using refractometry technique. The value of C_m represented the concentration at a distance of 200 μm from the membrane surface. Higher C_m and δ were obtained at higher feed concentrations (dashed curve 1 in Figure 2-14). Airey et al. [109] also observed higher δ at higher feed concentrations during crossflow microfiltration of bentonite solutions using NMR technique. However, Mc Donogh et al. [92] obtained opposite results during dead-end filtration of dextran blue solution using EDAM technique. Increasing the feed concentration had only a slight effect on C_m and decreased the layer thickness (dashed curve 2 in Figure 2-14). The effect of feed concentration on macroscopic flux performance has been studied by many groups [42-44, 49]. Generally, the flux drops more quickly at higher feed concentrations, which is at least in part due to the greater amount of solute that is brought to the membrane surface per unit time, increasing collision frequency between the solute particles and the membrane

surface. On the other hand, more particles are also rejected and accumulated near the membrane, resulting in severe concentration polarisation. The limiting flux was independent on the feed concentration, which might because that limit flux was reached at long-term filtration time, where the initial difference of feed concentration was weakened [135].

2.4.3 Effect of crossflow velocity

Generally, higher crossflow velocity results in thinner boundary layers [74, 91, 92, 108, 112]. However, there is conflict about the influence of crossflow velocity on C_m. Gowman et al. [90] reported higher C_m at higher crossflow velocities during gentle crossflow (velocity= 1 μL/min and 0.7 μL/min) filtration of HA (dashed curve 2 in Figure 2-14) by using refractometry technique. Mc Donogh et al. [92, 93], however, obtained opposite results using EDAM technique, in which increasing velocity (R_e = 0, 5, 15) decreased C_m during filtration of dextran blue solutions (dashed curve 3 in Figure 2-14). It is important to note that C_m represented the concentration at a distance of 200 μm or 20 μm from the membrane surface, respectively. For the macroscopic flux measurements, the rate and extent of flux decline were reduced, while the limiting flux was higher at increased crossflow velocities [42, 43, 139]. This could be explained by the higher crossflow velocity producing the greater shear forces along membrane surface that sweep away the deposit thereby reducing the concentration polarisation [138]. This is consistent with the microscopic measurements showing lower δ at higher crossflow velocity.

2.4.4 Effect of *p*H

The effect of *p*H on C_m has been reported by Vilker et al. using shadowgraph technique [88]. A higher C_m was obtained at *p*H 4.5 near the isoelectric point than at pH X during dead-end ultrafiltration of BSA solutions (dashed curve 2 in Figure 2-14. The value of C_m was extrapolated from the concentration profile curves. The effect of *p*H on δ was reported by Li et al. [116], who showed that δ was lower at *p*H 4.9 (isoelectric point, IEP) than 6.9 during crossflow ultrafiltration of BSA solutions using UTDR technique. However, the flux was also lower at *p*H 4.9, which means that the deposit thickness could not be simply related to the flux performance. Li et al. also found high turbidity, low rejection and high fouling resistance at pH 4.9, stating that even though

the deposit was thinner at pH 4.9, the deposit was more compressed, resulting in less permeability. This suggested that the flux decline was mainly controlled by the density of the deposit layer rather than the thickness. Huisman et al. [45] compared macroscopic filtration performance at different pH values during ultrafiltration of BSA solutions. They found that both the initial flux and final flux were at minimum values at the isoelectric point (pH 5), consistent with other reports [40, 42, 46, 135]. Two possible factors have been proposed. One is that the aggregates formed at the isoelectric point, where the electrostatic repulsion force between molecules reached the lowest, accentuate fouling. The alternative is that as protein molecules are in their most compact state at the isoelectric point, they can form a more densely packed layer. The results from more detailed microscopic measurements (higher C_m at IEP) could help to distinguish between these two reasons.

2.4.5 Effect of ionic strength

It was previously shown that increasing the ionic strength of the feed solution increased C_m and decreased δ (dashed curve 2 in Figure 2-14). In addition, lower limiting flux has been observed at increased ionic strength [37, 41, 47, 140, 141], which could be explained by the reduced electrostatic repulsion resulting from compression of the electric double layer (EDL) [42, 43, 47, 136, 137, 140, 142, 143]. However, other researchers have reported opposite results for BSA, showing an increased limiting flux at higher ionic strengths [39, 42, 48]. They proposed that a higher ionic strength induced greater BSA solubility. She et al. [42] found that lower retention was observed at higher ionic strength, which was consistent with the smaller molecular size of BSA at same conditions. By using the microfluidic channels and the digital video microscopy, Bacchin et al. found that ionic strength significantly affected the microstructure of the deposit layer. With the presence of KCl in the feed solution, dendrites of latex particles formed at the surface of the mimic membrane, while ultrapure water led to a more gradual obstruction of the microchannels [81].

2.5 Conclusions

This chapter reviewed and categorised the currently available techniques for microstructural measurements of filtration boundary layers. Techniques for determining concentration profiles C

(d, t) and determining the boundary layer thickness δ offer the ability to quantify particle concentrations as a function of the distance from membrane surface and filtration time. Techniques for visualising the membranes provide direct images of the fouled surface.

Additionally, this chapter summarised how these techniques have been applied to understand the effect of filtration conditions (transmembrane pressure, feed concentration, flow velocity, ionic strength, and pH) on the development of the boundary layer concentration profiles C_m and thickness δ. This microstructural information has been used to explain the flux decline in relation to macroscopic measurement of flux (initial flux, limit flux, and the rate of flux decline), which provides a better understanding of membrane fouling.

In summary, techniques based on optical microscopy, especially confocal microscopy system, show more advantages in the microstructural measurements of membrane fouling, which enables the direct examination of the membrane surface without distance limitation. More recently, microfluidic techniques have been used to study membrane fouling, providing more detailed information relating to particle clogging, jamming, and translocation at the single particle level. However, these techniques used to date have only allowed investigations on mimic membranes with pore sizes at the scale of microfiltration membranes (5-20 μm), and the diameter of tested model particles is at least several micron. Thus, for detailed investigations of membrane fouling during ultrafiltration of smaller scale particles (i.e. submicron), a new system combining the advantages of confocal microscopy and microfluidic technology must be developed.

The overall aim of this thesis was to develop a novel technique for investigating the deposition of individual sub-micron sized particles in real time during membrane filtration, and to apply this method to the development of new fundamental insights into the mechanisms of fouling.

Chapter 3 Development of A Novel Microfluidic System for Studying Particle Deposition during Ultrafiltration

The review of the state of art technologies for microstructural measurements of membrane fouling revealed a limitation in the ability to study the deposition of submicron particles. Here, the combination of confocal microscopy and microfluidics is investigated for detailed characterisations of particle deposition on ultrafiltration membranes. In this chapter, the development and initial application of a novel microfluidic filtration system was described that incorporates membrane filtration, microfluidics, confocal scanning laser microscopy, and a dual syringe pump flow control setup. The ability to successfully visualise the deposition of 0.4 μm model latex particles on PES membranes during crossflow filtration has been demonstrated. Preliminary experiments conducted using latex suspension was presented.

This chapter is adapted from a published paper:

Hongzhan Di, Gregory JO Martin, and Dave E. Dunstan. "A microfluidic system for studying particle deposition during ultrafiltration." *Journal of Membrane Science* 532 (2017): 68-75.

3.1 System design

The microfluidic system was designed to visualise the particle deposition process in real time (Fig. 3.1). Membrane properties (composition and pore size), particle properties (size and surface charge), and operating conditions (flow rate, temperature, transmembrane pressure and particle concentration) can be varied. The microfiltration device, confocal microscopy, and flow control setup are shown in Figure 3-1a. The microfluidic membrane filtration device was designed for upward filtration so that the active membrane surface could be visualised using an inverted microscope. The thickness of the bottom channel layer is 50 μm (channel depth is 25 μm) to satisfy the short working distance (100 μm) of the inverted high resolution objective lens. The microscope system, equipped with a high speed scanner and high resolution objectives, was used to visualise the continuous motion of the particles. Two syringe pumps were connected to the

inlet and outlet during filtration. The use of the two syringe pumps enables the cross flow velocity and the trans-membrane pressure to be varied independently, with the pump connected to the outlet tubing varied to control the flow rate and pressure drop in the micro channel. Alternatively, the outlet could be closed off to operate in dead end filtration mode.

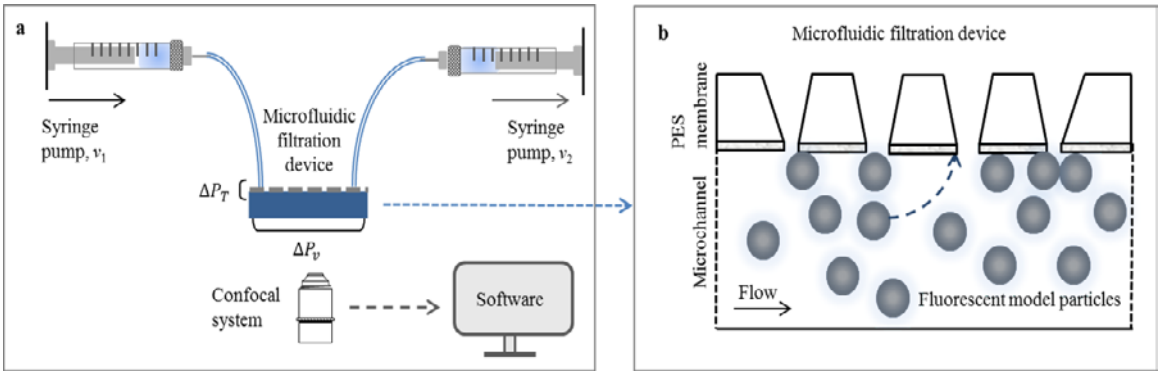

Figure 3-1 a) Schematic diagram of the microfluidic membrane filtration system. b) Schematic diagram of particle deposition on the membrane surface inside the device during cross-flow filtration. ΔP_V is the pressure drop across the microchannel to drive the fluid flow. ΔP_T is the transmembrane pressure. The magnitude of infusion velocity v_1 and withdraw velocity v_2 can be controlled to vary ΔP_V and ΔP_T independently.

3.2 Materials and methods

3.2.1 Materials

Polyethersulfone (PES) membranes (10 kDa, Koch membrane system Inc.) and model fluorescent polystyrene latex particles (0.4 μm, Thermo Scientific Inc.) were used in the filtration process. Potassium chloride (KCl, Chem Supply Inc.) was used to control the ionic strength of the latex suspensions. A ZetaSizer Nano (Malvern Instruments Ltd.) was used to measure the zeta potential of the latex particles. Silicon wafer, SU-8 2025 photoresist (MicroChem Corp.), and a UV flood light source (ABM, Inc.) were used to make the master mould. Profilometer XP 200 (AMbios Technology, Inc.) was used to measure the channel height. Trichloro (1H, 1H, 2H, 2H - perfluorooctyl) silane, (FTS, Sigma Aldrich Corp.) was used to coat an adhesive reduction layer on the master mould. Polydimethylsiloxane (PDMS, Sylgard® 184 silicone elastomer kit, Dow Corning Corp.) was used to make the channel patterned layer. 3-aminopropyltriethoxysilane

(APTES, Sigma Aldrich Corp.) was used as a chemical crosslinking agent between the PES membrane and the PDMS layer. Silicone tubing was affixed to a silicone pad, which was in turn affixed to the membrane device using epoxy glue. Fixed Luer Lock syringes (1 mL, SGE Analytical Science, Inc.) and PHD 2000 syringe pumps (Harvard Bioscience, Inc.) were used as to infuse and withdraw particulate solutions to and from the system.

3.2.2 Membrane filtration processes

Latex particle suspensions were prepared by diluting original stock latex suspensions in different KCl concentrated solutions to 5×10^{-6} solids concentration. The KCl concentration was varied in the range 10^{-4} to 1 M. The measured pH of the prepared latex suspensions was 5.6 ± 0.2. All prepared suspensions were put in an ultrasonic bath for 15 minutes before starting filtration processes to disperse the latex particles.

A polyethersulfone (PES) membrane with a nominal cut-off of 10 kDa was used in the microfluidic filtration device. The filtration process was operated in constant flux mode (5 L/hr/m^2) for 45 minutes. Permeate flow rate was 10 μL/h with an infusion flow rate of 110 μL/h and withdrawal flow rate of 100 μL/h.

3.2.3 Characterisation method

Three-dimensional, time-sequenced images of the microfluidic filtration channel were observed and recorded using a Nikon A1R+ resonant scanning confocal system. The dimensions of the field of view were 100 μm in length, 50 μm in width, and 25 μm in depth. A water immersion objective with 60x magnification was used to obtain high-resolution images. To characterise particle deposition on the membrane surface, the time-sequenced images of the membrane surface were analysed using Fiji software [144]. Original images were converted into binary 8 bit images and the occupied area fraction was calculated. To obtain particle deposition layer profiles, three-dimensional images obtained at different filtration times were analysed as a function of distance from the membrane surface.

3.3 Microfluidic filtration device fabrication

3.3.1 Channel-patterned PDMS layer

Preparation of the microfluidic device was undertaken using a master mould constructed using soft lithography as shown in Figure 3-2.

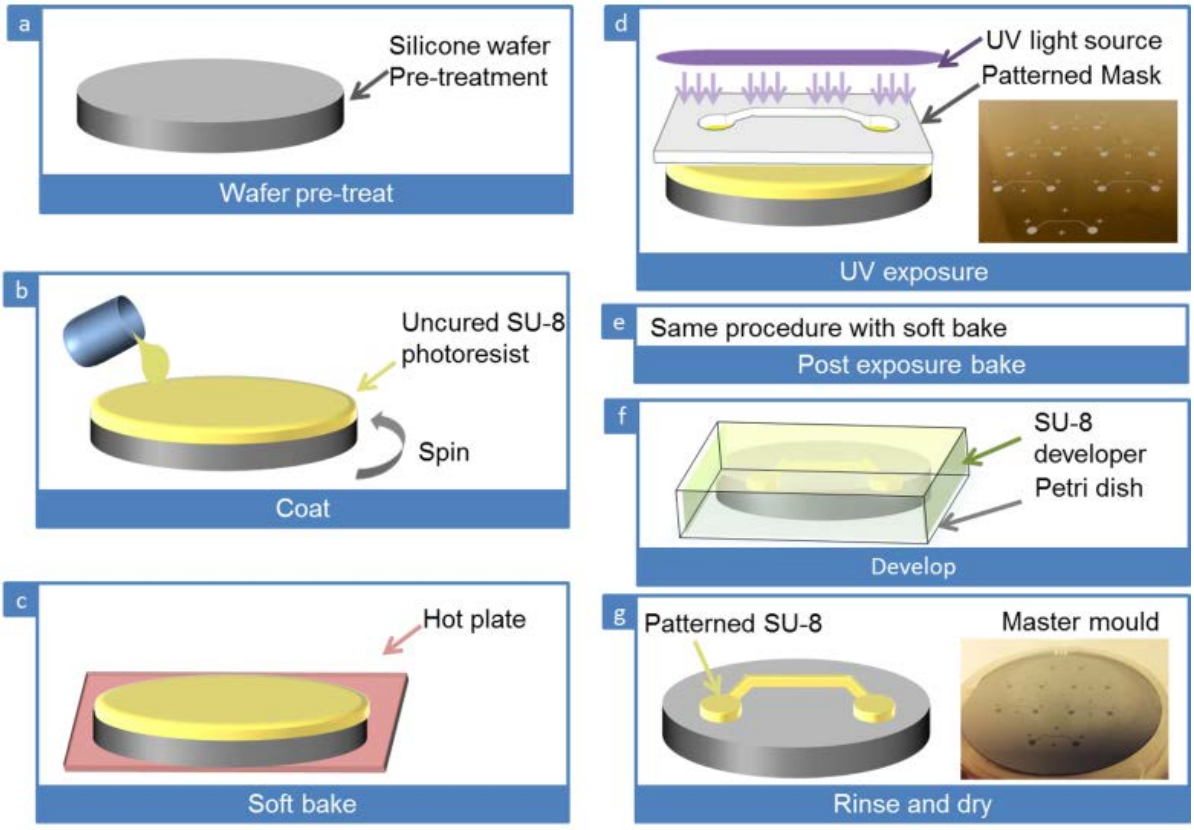

Figure 3-2 The principle steps in the procedure for fabricating the master mould using lithography. (a) wafer pre-treat (baked and dehydrated), (b) SU-8 photoresist coat, (c) soft bake by putting wafer on a hot plate, (d) UV exposure, (e) post exposure bake by putting wafer on a hot plate, (f) develop the pattern using SU-8 photoresist developer, and (e) rinse and dry to get the final master mould with patterns standing on the wafer. The thickness of the patterned SU-8 photoresist is 25 μm ± 2 μm. Only one channel structure is shown, while there were six channels on one mask and wafer.

The silicon wafer was baked and dehydrated at 170 °C for 5 minutes. A small volume of SU-8 2025 photoresist was spun on the silicon wafer at 2000 rpm for 30 seconds in a Laurell WS-650

spin coater. The wafer was then soft-baked at 65 °C for 1 minute, and 95 °C for 3 minutes on a hot plate. After soft-baking, the wafer coated with the SU-8 layer was set using UV light (Figure 3-2d). The patterned mask was designed with MEMSpro software. The energy of UV light was set at 160 mJ/cm^2 for 6 seconds to make 25 μm thin SU-8. After assembly, the device was hard-baked using the same procedure used for soft-baking. The wafer was then immersed in SU-8 developer for 3 minutes, rinsed with isopropyl alcohol for 10 seconds, Milli-Q water for 10 seconds, and finally dried using a stream of compressed nitrogen. The thickness of patterned SU-8 was 25 μm ±2 μm, as measured using a profilometer.

Before casting the PDMS, a thin layer of FTS was coated on the master mould to reduce the adhesion between the PDMS and the mould. A glass slide and the mould were placed into a desiccator. 20 μL of FTS was then placed on the glass slide. The desiccator was then held under vacuum for 2 hours, see Figure 3-4a. The thickness of the patterned PDMS layer was designed to be 50 μm to satisfy the short working distance of confocal microscope. The standard ratio of PDMS base to curing agent was varied from 10:1 to 5:1 to produce a more rigid film that could be more readily removed from the mould without folding. The PDMS mixture was then spun on the mould at 900 rpm for 1 minute. The mould coated with PDMS was then placed in the oven at 65 °C for 1 hour. The thin PDMS layer was then peeled off the mould and cut into individual pieces carefully. The principal procedures are shown in Figure 3-3. The thickness of PDMS layer was 50 μm (±2 μm), and the depth of channel was 25 μm ±2 μm, as measured using a profilometer.

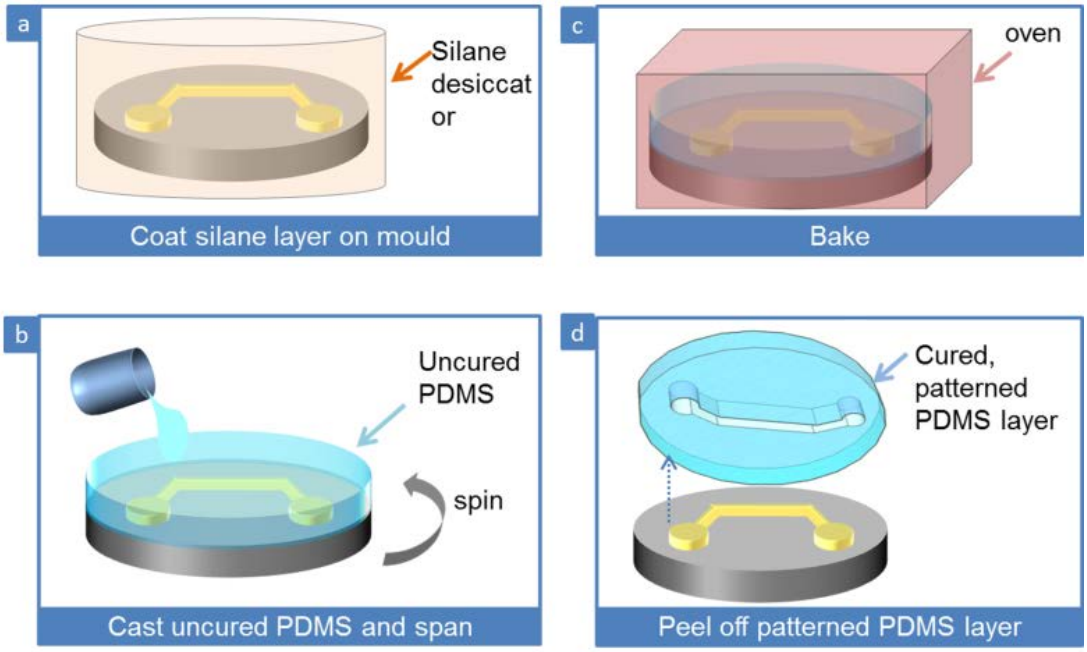

Figure 3-3 Schematic diagram of the casting-patterned PDMS layer. The thickness is 50 ±2 μm, and the channel depth is 25 ± 2 μm. (a) coat silane layer on the mould, (b) cast uncured PDMS on the mould, (c) bake the wafer and PDMS in an oven, (d) peel patterned PDMS layer off the mould. Only one channel structure is shown, while there were six channels on one wafer and PDMS layer.

3.3.2 Device assembly

The commercial PES membrane in our device consisted of two layers; the effective PES layer and the support polyester layer. In order to get reliable bonding between the PES layer and the PDMS layer, APTES was used as the chemical crosslinking agent [29].

Step 1: To induce the hydrolysis reaction to replace the alkoxy groups of APTES with hydroxyl groups, the APTES was diluted by Milli-Q water to 5 % concentration by volume, and placed on a level hot plate of 80 °C (Figure 3-4a). Step 2: To create hydroxyl groups on the PES membrane surface, the PES membrane was put into an air plasma apparatus (600 mTorr, high energy) for 1 minute (Figure 3-4b). Step 3: To react the hydroxyl groups with each other to form C-O-Si bonds to coat APTES onto the PES membrane surface, the plasma treated membrane was immersed in the APTES solution prepared in step 1 for 20 minutes (Figure 3-4c). The container was covered to avoid vapour escape. Step 4: To introduce hydroxyl groups onto their surfaces, the channel patterned PDMS layer and the APTES coated PES membrane were then placed in the air plasma

apparatus (600 mTorr, high energy) for 1 minute (Figure 3-4d and e). Step 5: Finally the treated PDMS layer and PES layer were pressed tightly into contact to form C-O-Si bonds (Figure 3-4f).

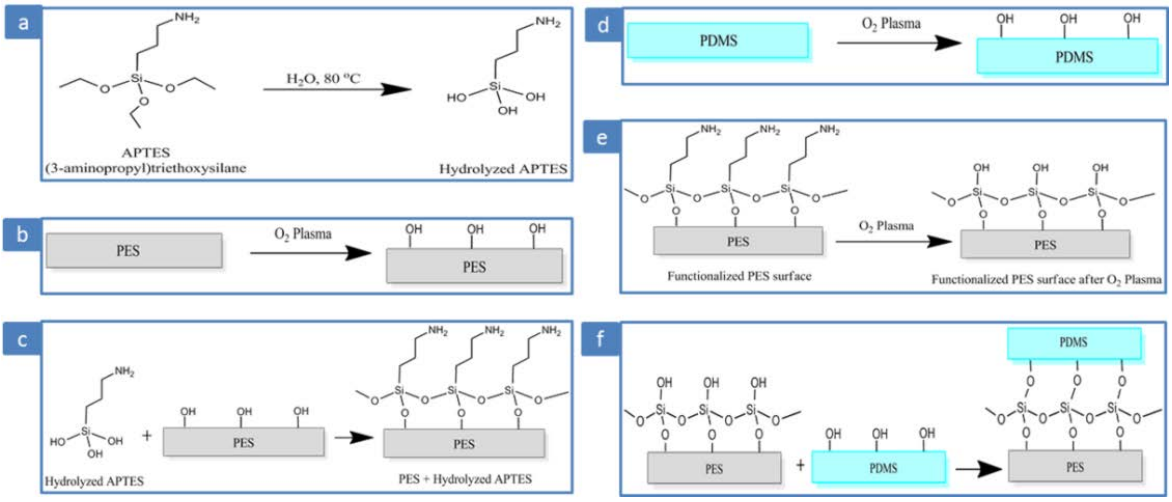

Figure 3-4 Chemical mechanisms of the bonding of the PDMS and PES layers. The step included: (a) replacement of the alkoxy groups of APTES with hydroxyl groups, (b) creation of hydroxyl groups on the PES membrane surface, (c) formation of C-O-Si bonds to coat APTES onto the PES membrane surface, (d) introduction of hydroxyl groups onto PDMS surfaces, (e) introduction of hydroxyl groups onto functionalised PES surfaces, (f) formation C-O-Si bonds between PES and PDMS.

A 1.5 mm diameter hole was drilled in the middle of a round silicone pad with thickness of 1.5 mm. A section of silicone tubing (OD, 1.5 mm) was inserted into the hole, and bonded to the silicon pad by epoxy glue. The laminate was left for 1 hour to ensure good bonding. The epoxy glue was then used to bond the other side of the silicon pad to the membrane support layer. More epoxy glue was added to surround the silicone pad to enhance the bonding strength. The whole device (Figure 3-5) was left for another 1 hour to achieve optimal bonding.

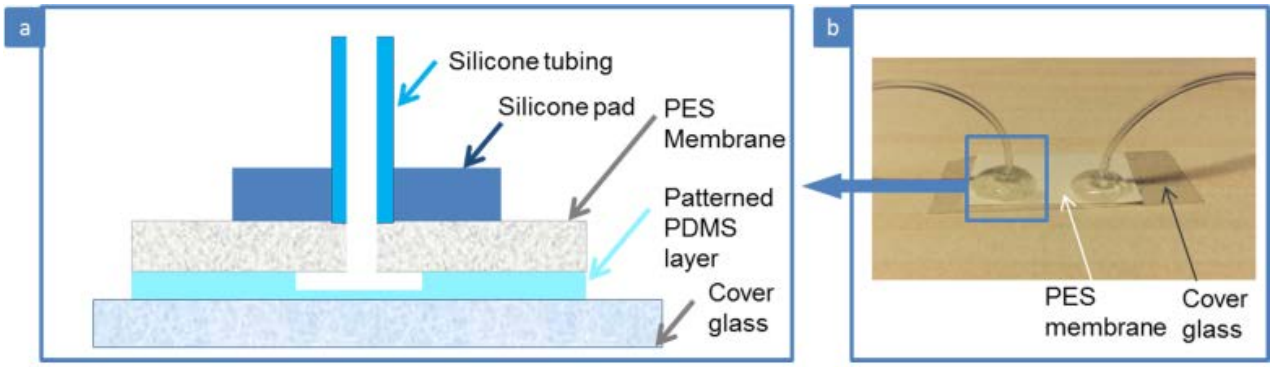

Figure 3-5 a) Schematic diagram of the cross section of the inlet/outlet, and b) final appearance of the device. From the bottom to the top are cover glass, patterned PDMS layer, PES membrane, silicone pad, and silicone tubing respectively.

3.4 Results and discussions

3.4.1 Particle deposition on the membrane surface

To study the influence of ionic strength on the particle deposition process, latex suspensions in 0.01 M KCl and 1 M KCl were used. Temporal development of the membrane surface during filtration is shown in Figure 3-6 below. It appears that the particles were deposited heterogeneously and incompletely on the membrane surface for both latex suspensions. For the 0.01 M KCl suspension, the particles show more isolated deposition on the membrane surface for the whole filtration process (Figure 3-6a, 3x zoom). In contrast, the particles in 1 M KCl tended to aggregate on the membrane surface during filtration (Figure 3-6b, 3x zoom).

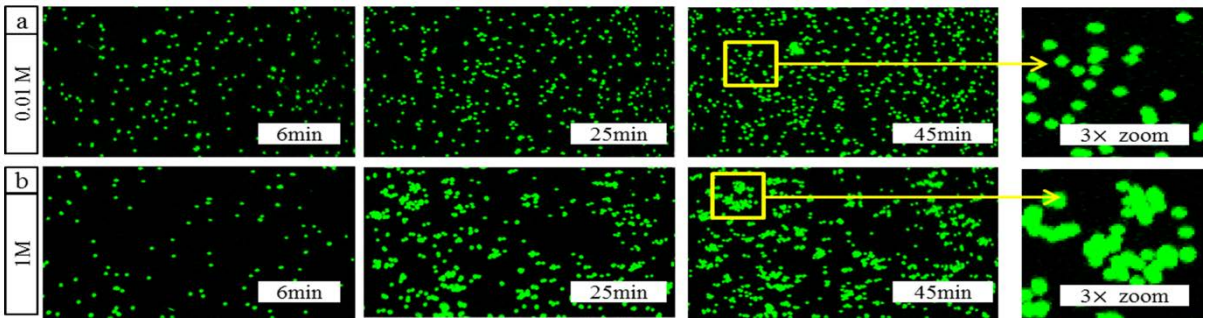

Figure 3-6 Images of the membrane surfaces at different times during filtration of latex suspensions. (a) 0.01 M KCl suspension. (b) 1 M KCl suspension. More deposition is observed as filtration time increases, and more aggregates are found with the presence of 1M KCl in

suspension. The dimensions were 100 μm by 50 μm for the temporal images, and 18 μm by 17 μm for the 3x magnified images.

The extent of aggregation of the particles deposited on the membrane surface was evaluated as a function of time. The fraction of area occupied by isolated particles, aggregates composed of two particles, and large aggregates composed of more than two particles is presented in Figure 3-7.

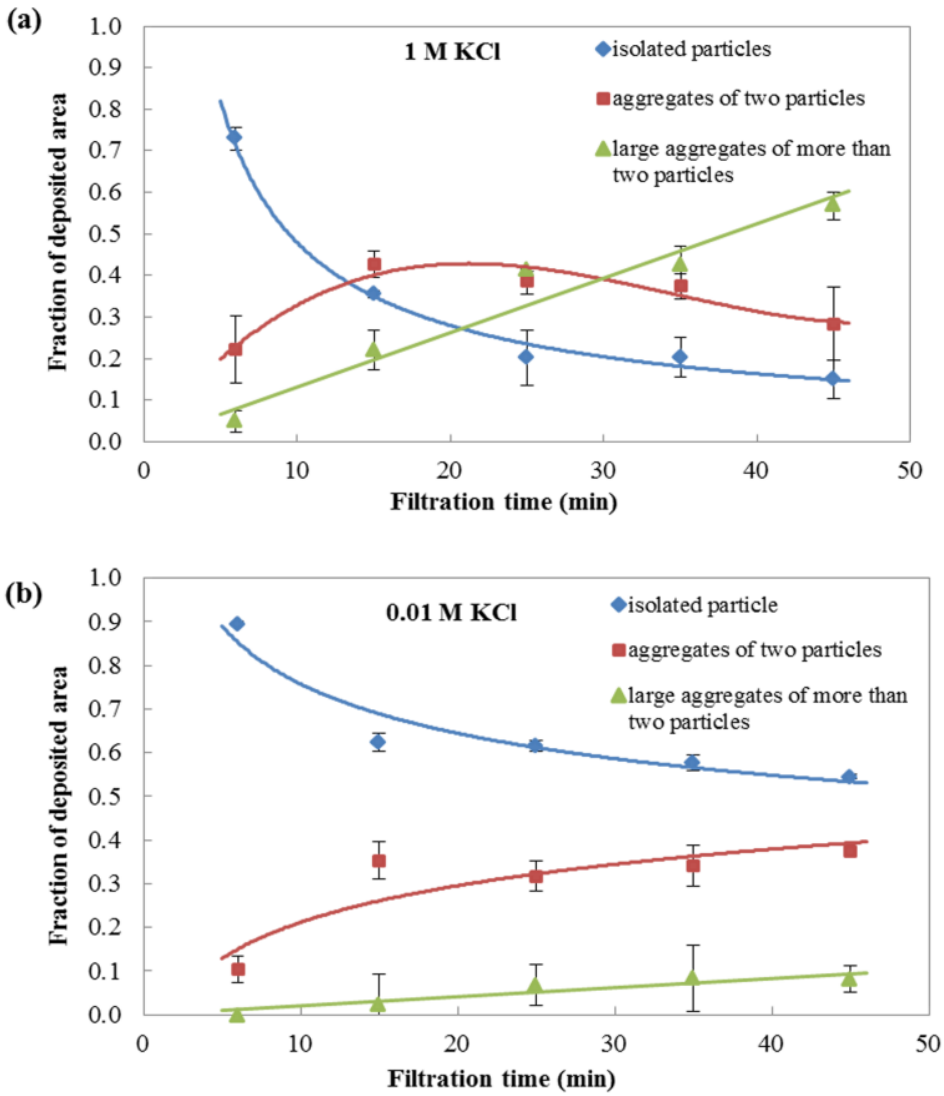

Figure 3-7 Percentage of the deposition layer occupied by isolated particles (blue diamonds), aggregates of two particles (red squares), and aggregates of more than two particles (green triangles) as a function of filtration time in (a) 0.01 M KCl and (b) 1M KCl suspensions. As the

filtration time increases, fraction of isolated particles decreases while fractions of aggregates and large aggregates increase for both conditions.

For latex suspensions in 0.01 M KCl, isolated particles dominated the deposited area during the whole filtration process, although the percentage decreased from 90% (6 minutes) to 55% (45 minutes). Aggregates composed of two particles increased from 10% (6 minutes) to 37% (45 minutes). Large aggregates composed of more than two particles were much less common, observed only after 15 minutes filtration and eventually representing 8% of the deposited area after 45 minutes. According to Pontié et al. 1997 [145] the zeta potential of the membrane surface should be about -5 mV at 0.01 M KCl, much less negative than the particles (-67 mV). This means the electrostatic repulsive forces between the membrane surface and the particles are less than those between the particles themselves. This provides some explanation for the initial deposition of individual particles onto the membrane, as particles are brought towards the membrane as a result of solute flux. The increase in the extent of aggregation in the deposited particles during filtration (Figure 3-7a) suggests that once deposited, the particles can act as seeds for further deposition. Presumably the subsequently deposited particles are shielded/sheltered hydrodynamically by the already adsorbed particles.

For latex suspensions in 1 M KCl, the initial deposition appeared to be primarily of individual particles (Figure 3-6b and Figure 3-7b) that then acted as seeds for the subsequent deposition of particles and aggregates. After 45 minutes filtration, large aggregates dominated the deposited area. The reason that initial deposition was of individual particles might be that individual particles are more likely to be brought onto the membrane surface by the drag force resulting from permeate flux, while aggregates are pulled away by the shear stress resulting from the crossflow.

To compare the rates of the particle deposition, plots of the fraction of membrane surface area covered by the particles are presented as a function of filtration time at both KCl concentrations (Figure 3-8). The amount of deposited particles increased during filtration at both KCl concentrations. After 6 minutes, there was more particle deposition at 0.01 M KCl than that at 1 M KCl (Figure 3-6and Figure 3-8), despite the less negative zeta potential of the particles in 1 M

KCl (noting that the zeta potential of PES membranes was reported to be similar at these two KCl concentrations). This is presumably due to the lower concentration of individual particles at 1 M KCl, which were seen to deposit prior to the addition of aggregates (Figure 3-6and Figure 3-7). For the subsequent 10 minutes of filtration, the area fraction for 1 M KCl remained lower but increased at a higher rate than 0.01 M KCl, reaching a value close to 0.01 M KCl at around 15 minutes. This can be explained by the delayed onset of the deposition of aggregates (existing or later developed) onto the membrane at 1 M KCl (Figure 3-7b). After 15 minutes of filtration a higher rate of deposition for the 1 M KCl compared to that for 0.01 M KCl suspension was observed due to the further deposition of particles and aggregates (Figure 3-7b).

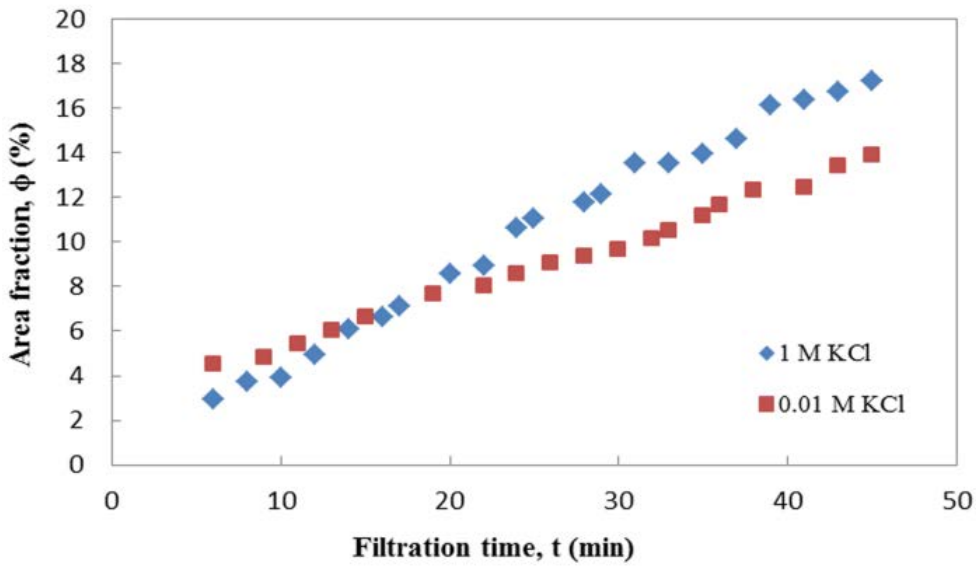

Figure 3-8 Covered area fraction φ as a function of filtration time t. Red markers stand for 0.01 M KCl suspension. Blue markers stand for 1 M KCl suspension.

3.4.2 Boundary layer profiles

Figure 3-9 shows time-sequenced three-dimensional (3D) images of the channel within the microfluidic filtration device. Due to the inverted filtration design, the top bright section shows the particle deposition layer on the membrane surface, below which was the microchannel. Note that 3D images were assembled by a z-stack of 2D images. The side view of latex particles resembled cones rather than spheroids due to stray light which was recorded during the z-stack acquisition. A distortion (approximately 10-fold) of particles was observed in the z depth. Only

monolayers were observed on the membrane surface for both KCl concentrations (see also Figure 3-10). These results suggested that any aggregates (initially deposited or later developed) oriented themselves in parallel rather than perpendicularly to the membrane surface. Particles in the bulk flow (middle section) were observed as stretches rather than spheroids due to the scanning rate not being able to catch up with the flow velocity. Some particles were found at the bottom surface of the channel, indicating particles could also deposit on the bottom wall during the filtration experiment.

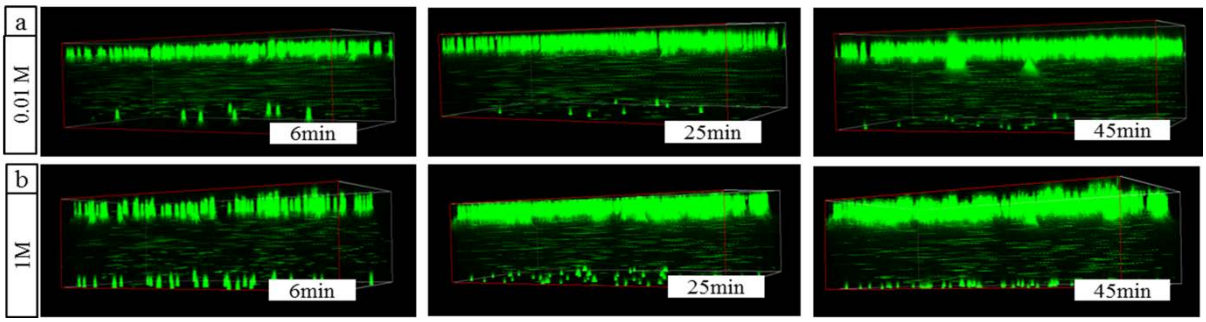

Figure 3-9 Three-dimensional images of the microfluidic filtration device at different time during filtration of latex suspensions. (a) 0.01 M KCl concentrated suspension. (b) 1 M KCl suspension.

Figure 3-10 presents the boundary layer profiles on the basis of area fraction as a function of filtration time and distance from the membrane surface (after correction of the optical distortion). As might be expected, for each specific filtration time, the area fraction decreased with increasing distance from the membrane surface. Also, the area fraction increased with filtration time (bottom curve to top curve) due to the net accumulation of deposited particles. Finally, consistent with Figure 3-9, only monolayers were formed regardless of the KCl concentration. Note that the obtained boundary layer profiles started from the membrane surface (z = 0), eliminating the previous restriction to observations of the boundary layer profiles that could only be made at least 20 μm away from the membrane surface [102, 105]. The data clearly show that a reduction in the electrokinetic potential on the particle surface (and interaction potential) increased the particle deposition and modified the structure of the deposit on the membrane.

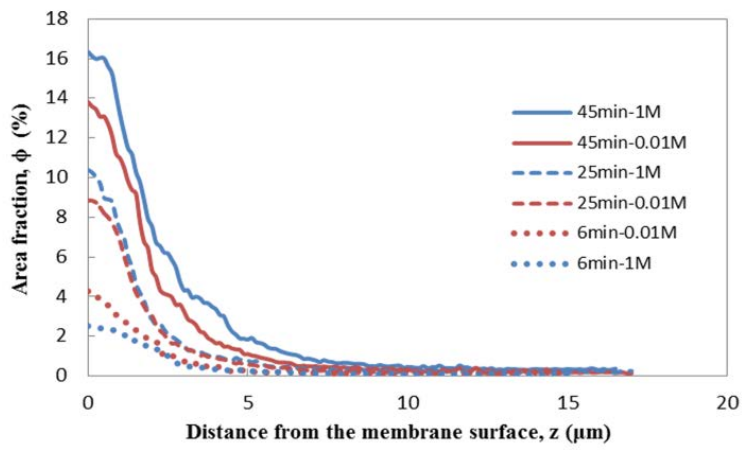

Figure 3-10 Boundary layer profiles. Covered area fraction φ as a function of the distance from the membrane surface z at different filtration time. Red lines stand for latex suspensions with 0.01 M KCl. Blue lines stand for latex suspensions with 1 M KCl. Dotted lines are obtained at 6 minutes, dashed lines are obtained at 25 minutes, and solid lines are obtained at 45 minutes.

3.5 Conclusions

A novel experimental membrane system, combining microfluidic technology, confocal laser scanning microscopy, and two-syringe pump flow control setup was developed. This system was used to successfully visualise and quantify the particle deposition process during cross-flow filtration of latex suspensions (particle diameter 0.4 μm) in 0.01 and 1M KCl solutions. Time-sequenced, high-resolution images of the membrane surface and 3D views of the micro channels have been obtained. In addition, the overall deposition behaviour has been characterized by the surface coverage and the deposit layer profile. Note that time-resolved deposit layer profiles at a distance of less than 20 μm from the membrane surface were obtained that provides a new level of experimental insight into the particle deposition mechanism validating models. Using the system reported here it is possible to perform further investigations into the impact of key parameters on particle deposition, which contributes to better understand the key mechanisms of membrane fouling and particle deposition. \

Chapter 4 Membrane-Particle and Particle-Particle Interactions as Influenced by Solution pH and Ionic Strength

Solution properties such as pH and ionic strength have significantly influence on membrane fouling by changing the surface zeta potential of the membrane and particles which thus varies the fundamental interactions between particles as well as between the membrane and particles. The aim of this chapter is to study the exact roles of pH and ionic strength on the membrane-particle and particle-particle interactions. Zeta potential of latex particle and PES membrane were measured, and the interaction energies of membrane-particle and particle-particle were determined for further studies in the following chapters.

4.1 Introduction

During membrane filtration the deposition of particles onto the membrane, or the association of particles with already deposited particles, will depend on energies/forces governing particle interactions and movement [136, 146]. In particular, the membrane-particle interaction energy $V_{m\text{-}p}$ will influence the deposition of particles directly onto the membrane surface, and the particle-particle interaction energy $V_{p\text{-}p}$ will affect the formation of particle aggregates (Figure 4-1). This chapter studies the influence of pH and ionic strength on the membrane-particle and particle-particle interaction energies, which will be further used for next two chapters. Interaction energies are determined by incorporating DLVO theory, Van der Waals attraction energy, and modified Hogg-Healy-Fuersteneau (HHF) formula.

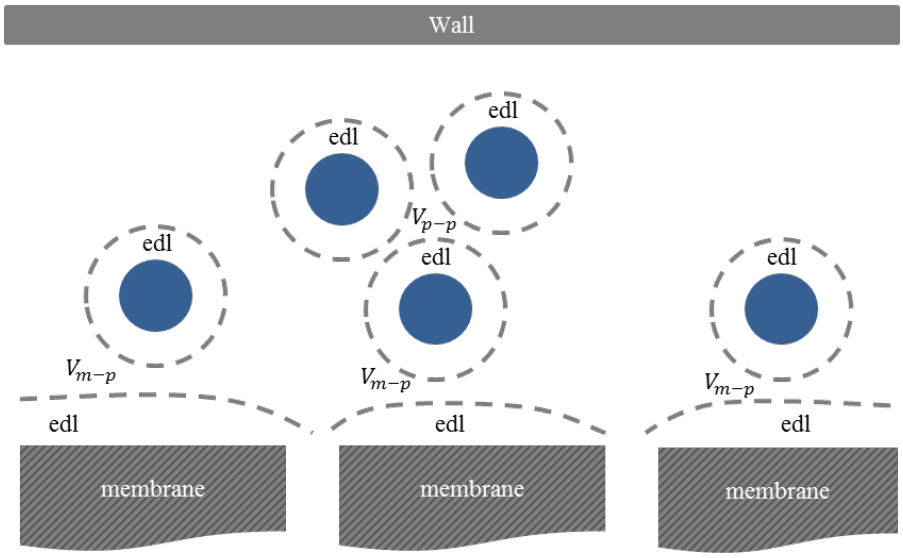

Figure 4-1 Diagrammatic representation of the interaction energies relevant to membrane-particle and particle-particle interactions during cross-flow filtration. $V_{m\text{-}p}$ = Interaction energy between membrane and particle; $V_{p\text{-}p}$ = Interaction energy between particle and particle; edl = electric double layer.

4.2 Interaction energies

The DLVO theory (named after Derjaguin, Landau, Verwey, and Overbeek), which is based on the superimposition of electrostatic interaction energy and van der Waals interaction energy, is normally used to determine the interaction energy between particles or surfaces. Typically, colloidal particles carry a negative charge, whereas membranes can be either negatively or positively charged depending on their chemical composition. When a particle approaches other particles or surfaces of a like charge, there is an electrostatic energy barrier that must be overcome to deposit or aggregate. Steric repulsion may also play a role, however this will not be considered in this study, in which smooth particles and surfaces are studied. If the particle and the membrane are oppositely charged, there will be an electrostatic attraction to promote the deposition. According to the DLVO theory, the total interaction energy (V_T) is expressed as the sum of electrostatic interaction energy (V_e) and van der Waals interaction energy (V_{vdW}).

$$V_T = V_e + V_{vdW} \tag{4-1}$$

The total interaction energy is a function of distance (i.e. particle-particle or particle-membrane separation). In order for aggregation to occur, the kinetic energy must be sufficient to exceed the energy barrier at its highest point. Therefore, the particle deposition process, which involves membrane-particle and particle-particle interactions, is dependent on both the magnitude of the electrostatic energy barrier and the dynamics of the collisions. This study examines the deposition process in relation to changes in electrostatics as influenced by pH and ionic strength and considers the effects of particle concentration and flow on the collision dynamics.

4.2.1 Electrostatic interaction energy

In this paper, we used the modified Hogg-Healy-Fuersteneau (HHF) formula reported by Sader et al. [147] to describe the electrostatic interactions between two dissimilar spheres (i.e. the particles, and the membrane surface, which can be considered to be a sphere of infinite radius). The well-known HHF formula is used when the Derjaguin approximation is applied to the two-sphere problem in the linear Debye-Hückel theory, which is valid only in the small κh regime. κ is the inverse of the Debye length λ (the thickness of electric double layer), and h is the distance of closest approach between the spheres. The modified HFF proposed by Sader et al. extends the region of validity to all κh. The electrostatic interaction energy V_e between dissimilar spheres in the modified HHF formula is shown below [147]:

$$V_e = \frac{\varepsilon}{4}\left(\frac{k_B T}{e}\right)^2 \frac{a_1 a_2}{S}\left[(\psi_1+\psi_2)^2 \ln\left(1+e^{-\kappa h}\right) + (\psi_1-\psi_2)^2 \ln\left(1-e^{-\kappa h}\right)\right] \quad (4\text{-}2)$$

k_B is Boltzmann's constant (1.38×10^{-23} J·K^{-1}), T is the absolute temperature (K), e is the proton charge (1.6×10^{-19} C), ε is the permittivity of the solution surrounding the spheres, which is the product of vacuum permittivity ε_0 (8.854×10^{-12} C·V^{-1}·m^{-1}) and dielectric constant Ke (80 for water), ψ_1 and ψ_2 are the reduced surface potentials [i.e., scaled by ($k_B T/e$)] on sphere 1 and 2, respectively, a_1 and a_2 are the radius (m) of sphere 1 and 2, respectively, and h is the distance (m) between the surfaces of two spheres, S is the distance (m) between the centres of two spheres. When the membrane is represented by a sphere with infinite radius of a_2 compared to the sphere

radius of a_1, the electrostatic interaction energy V_e between particle and membrane can be obtained from Eq.2.

In relation to particle-particle interactions, for two identical spheres, $a_1 = a_2 = a$, the modified HFF formula is derived from the nonlinear Poisson-Boltzmann (NLPB) equation as [147]:

$$V_e = \varepsilon \left(\frac{k_B T}{e}\right)^2 \psi^2(h) \frac{a^2}{S} \ln\left(1+e^{-\kappa h}\right) \tag{4-3}$$

in which

$$\psi\,(h) = 4e^{\kappa h/2} \tanh^{-1}\left[e^{-\kappa h/2} \tanh\left(\frac{\psi_s}{4}\right)\right] \tag{4-4}$$

ψ_s is the reduced surface potential of two identical spheres. The function ψ (h) in Eq.4 is an effective surface potential that varies gradually with separation h when the surface potential becomes large.

4.2.2 Van der Waals attraction energy

The well-known Hamaker expression for the van der Waals interaction energy between two spheres of radius a_1 and a_2 was given by [148]:

$$V_{vdW} = -\frac{A_H}{6}\left[\frac{2a_1a_2}{S^2-(a_1+a_2)^2} + \frac{2a_1a_2}{S^2-(a_1-a_2)^2} + ln\left(\frac{S^2-(a_1+a_2)^2}{S^2-(a_1-a_2)^2}\right)\right] \tag{4-5}$$

A_H is the Hamaker coefficient, a constant depending on the material properties (typical values are in the range of 10^{-19} - 10^{-21} J). For two identical particles, $a_1 = a_2 = a$, the energy function can be simplified to

$$V_{vdW} = -\frac{A_H}{6}\left[\frac{2a^2}{S^2-4a^2} + \frac{2a^2}{S^2} + ln\left(1-\frac{4a^2}{S^2}\right)\right] \tag{4-6}$$

For a sphere (radius a) and a flat membrane, the van der Waals interaction energy function was given by [146]:

$$V_{vdW} = -\frac{A_H a}{6h^*} \tag{4-7}$$

where h^* is defined as the separation distance (m) between the surface of the sphere and the membrane surface.

4.3 Materials and Methods

4.3.1 Materials

Polyethersulfone (PES) membranes (10 kDa, Koch membrane system Inc.) and fluorescent polystyrene latex particles (0.4 μm diameter, Thermo Scientific Inc.) were used in the measurement of zeta potentials. Potassium chloride (KCl, Chem Supply Inc.) was dissolved in MilliQ water to control the ionic strength of latex suspensions. Sodium hydroxide and hydrochloric acid (Sigma-Aldrich Co. LLC.) were used to adjust the solution pH.

4.3.2 Measurements of zeta potential of latex particles

A ZetaSizer Nano (Malvernn Instruments Ltd.) was used to measure the zeta potential and particle size of latex particles. To study the influence of pH, sodium hydroxide and hydrochloric acid were used to adjust pH to 3, 4, 5.6, and 8 (the pH of solutions before adjustment was 5.6 ± 0.2). All latex solutions were prepared by diluting original stock latex suspensions in 0.01M KCl concentrated solutions to 2×10^{-5} in volume fraction. To study the influence of ionic strength, latex solutions were prepared by diluting original stock latex suspensions to a volume fraction of 2×10^{-5} in KCl solutions of 0.01, 0.1, and 1M. To study the influence of feed concentration, latex solutions were prepared by diluting original stock latex suspensions to achieve volume fractions of 0.5, 2, and 8×10^{-5} in 0.01M KCl. All prepared latex solutions were put in the ultrasonic water bath before the zeta potential measurements.

4.3.3 Measurements of the zeta potential of membranes

The zeta potential of PES membranes was determined by a Zeta potential analyser (SurPass, Anton Paar GmbH) using a clamping cell. To prepare membrane samples, two pieces of identical flat membranes were cut appropriate to the flow channel geometry and then mounted opposite of

each other and separated by a spacer in the clamping cell, as shown in Figure 4-2 [149]. For a detailed flow diagram, refer to the literature reported by Salgin et al. [150]

After the clamping cell was mounted in the instrument, the system was filled and then rinsed with the targeted salt solutions. To study the influence of ionic strength, salt solutions were prepared in MilliQ water to concentrations of 0.005, 0.01, 0.05, 0.1, and 1M KCl (the pH of the prepared salt solutions was 5.6 ± 0.4). To study the influence of pH, an automatic pH titration was performed at room temperature over a pH range from 3.0 to 8.0 (0.1 M KOH or 0.1 M HCl were used for adjusting the pH of the solutions) with presence of 0.01M KCl. New membrane samples were mounted for each measurement cycle.

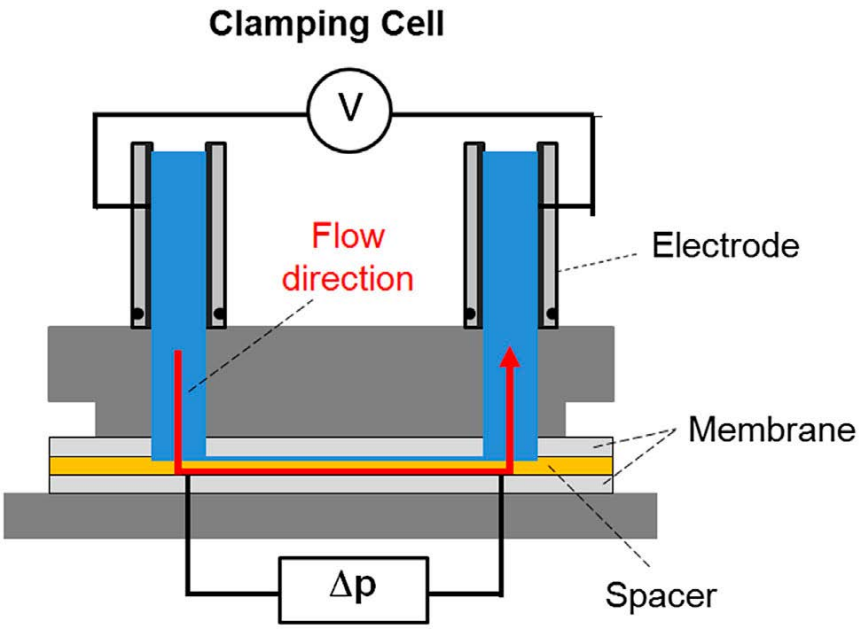

Figure 4-2 Schematic representation of the clamping cell of the SurPass instrument. The clamping cell comprising two layers of membrane and a flow channel in sandwich form. The downstream convection of ions via pressure-driven flow induces a streaming potential which can be related to the zeta potential of the membrane [149].

4.4 Results and Discussions

4.4.1 Zeta potential and particle size of the latex particles

The zeta potential of latex solutions was measured under various pH, ionic strengths and latex volume fractions (Figure 4-3). The zeta potentials of the latex particles were negative, and the magnitude of zeta potential showed an increasing trend as pH increased under all conditions tested. It can be seen that ionic strength had an important influence on the zeta potential of latex particles. In the presence of 0.01M KCl, the zeta potential of latex particles was significantly negative with a range of -50 to -80 mV, while in the presence of 1M KCl, latex particles were slightly negatively charged from -10 to -20 mV (Figure 4-3 d, e, and f). In addition, the zeta potential of latex particles became more sensitive to pH changes as ionic strength decreased. Latex volume fraction was found to have little effect on the zeta potential of latex particles (Figure 4-3a, b, and c).

The nominal size of the latex particles according to manufacturer specification was 0.4 μm in diameter. The actual particle size in various solution conditions was measured, to determine if any aggregates were present (Figure 4-4). In the presence of 0.01M KCl, the particle size was found to be independent of pH and feed volume fraction with an average diameter of 0.4 μm. However, as the KCl concentration increased to 1 M, the diameter of latex particles increased to around 0.8 μm (Figure 4-4d, e, and f).

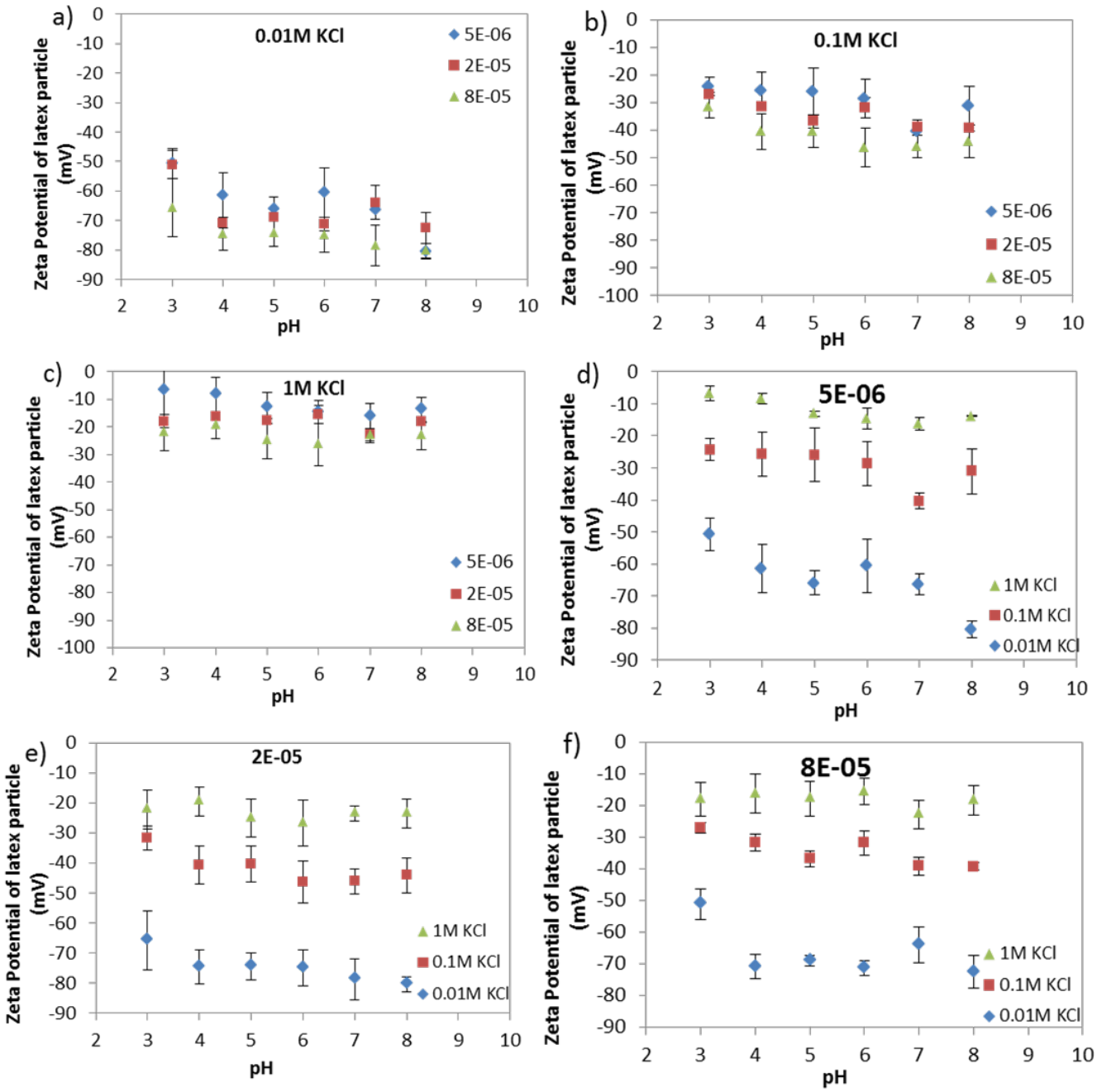

Figure 4-3 Zeta potential of latex particles as a function of pH, KCl concentration, and latex volume fraction. pH varies from 3 to 8. KCl concentration varies from 0.01 to 1 M, and the latex volume fraction varies from 5×10^{-6} to 8×10^{-5}. Latex particles are negatively charged for all tested conditions. The magnitude of the zeta potential increases as pH increases and as KCl concentration decreases. Latex volume fraction shows less influence on the zeta potential of latex particles.

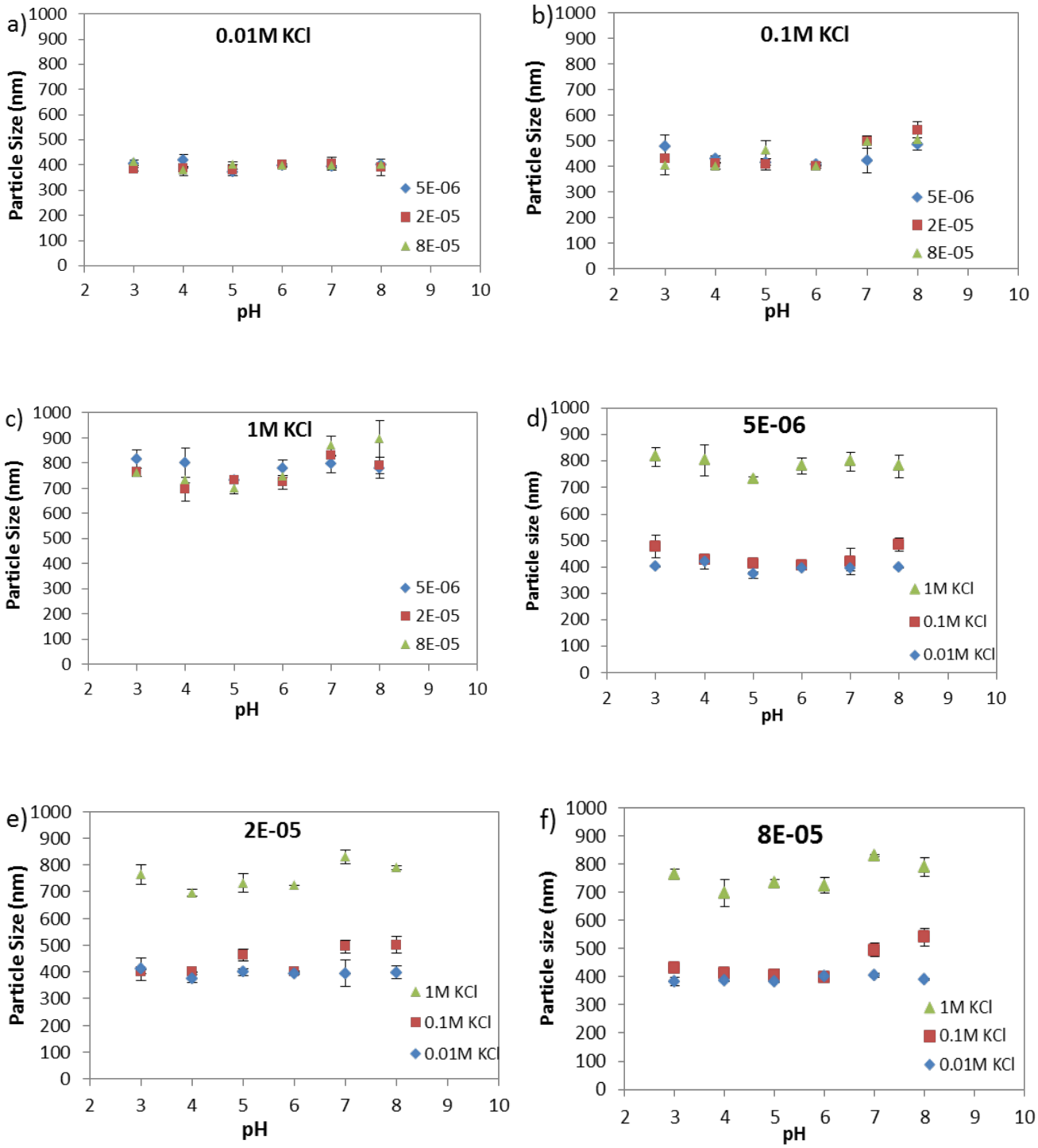

Figure 4-4 Apparent size of latex particles as a function of pH, KCl concentration and latex volume fraction. pH varies from 3 to 8, KCl concentration varies from 0.01 to 1 M, and latex volume fraction varies from $\mathbf{5} \times 10^{-6}$ to 8×10^{-5}. The size of latex particles are barely affected by pH, latex volume fraction and lower KCl concentration (0.01M and 0.1M). Aggregates are found at 1M KCl.

4.4.2 Membrane zeta potential

The zeta potential of the membrane surface under various pH conditions was measured in the presence of 0.01M KCl (Figure 5-4a). It shows that the membrane was positively charged, and the magnitude of the zeta potential decreased as pH increased from 3.0 to 8.0. Figure 4-5b plots the zeta potential of membranes as a function of KCl concentration. It can be seen that as ionic strength increased, the zeta potential decreased and actually converted from positive values into negative values (Figure 4-4b). It is not completely clear why this is the case, however similar results have been reported by Salgin et al. [150].

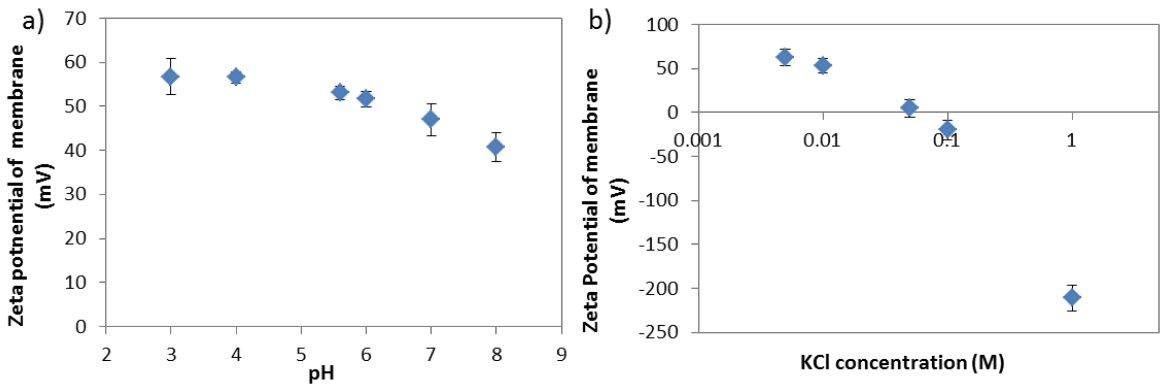

Figure 4-5 Zeta potential of the membrane surface a) as function of pH when the KCl concentration is 0.01M and b) as a function of KCl concentration at pH 5.6. The membrane surface is positively charged and zeta potential decreases as pH increases with the presence of 0.01M KCl in solution. As KCl concentration increased from 0.005 to 1 M, the charge of the membrane surface converts from being positive to being negative.

4.4.3 Interaction energies

Based on the measured zeta potential of latex particles and membranes, the particle-particle interaction energy (Figure 4-6a and b) and the membrane-particle interaction energy (Figure 4-6c and d) can be calculated using equations 4-1 to 4-7.To determine the membrane-particle interaction energy, the membrane was assumed to be a particle with infinite radius a_2 (it was assumed that $a_2 = 1000a_1$ in this work, where a_1 was the radius of latex particles). The Hamaker constant was chosen to be 1.5×10^{-20} J for the interaction of polystyrene particles and PES

membrane in an aqueous medium [151], while the Hamaker constant was assumed to be 5×10^{-21}J for polystyrene particles in an aqueous medium [72].

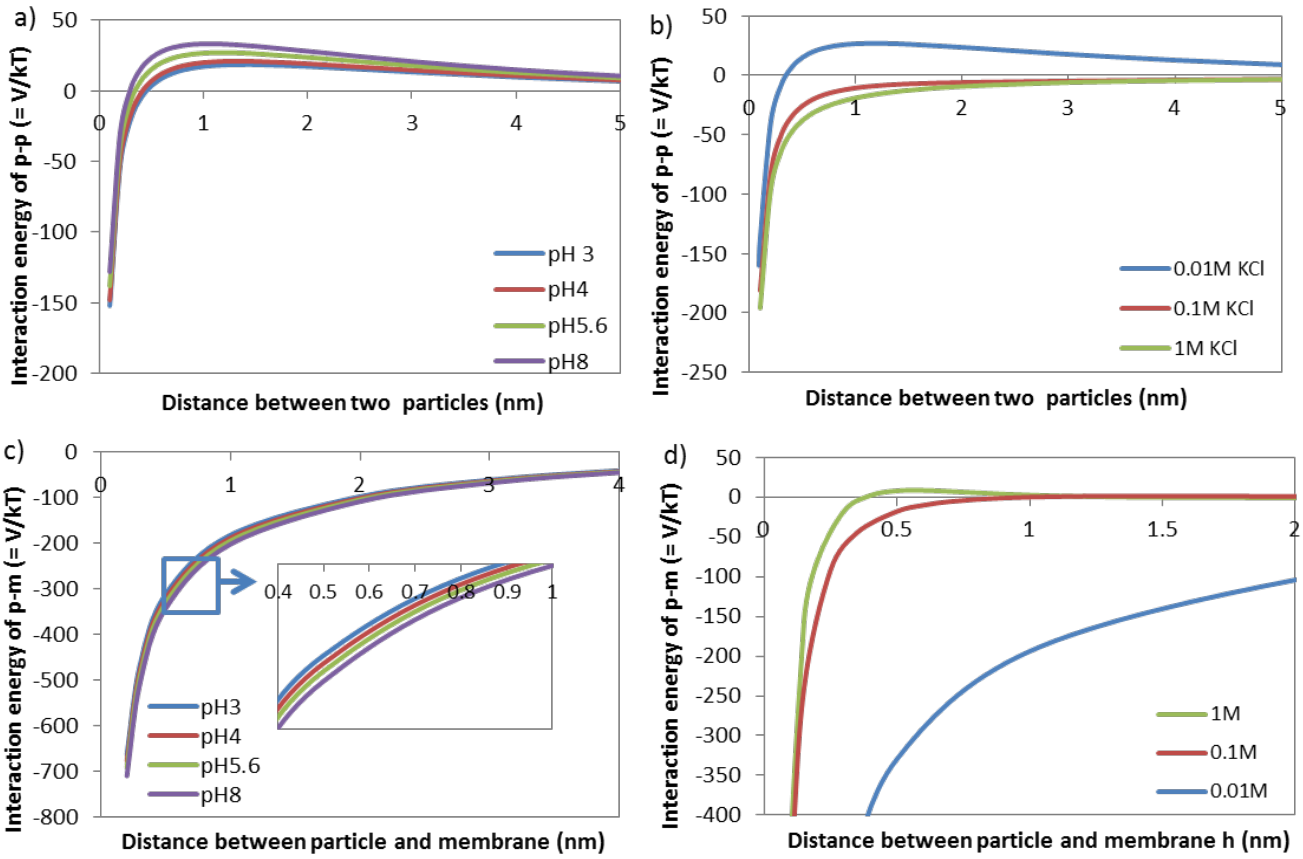

Figure 4-6 Interaction energies of particle-particle as a function of a) pH with the presence of 0.01M KCl and b) KCl concentration at pH 5.6. Interaction energies of particle-membrane as function of c) pH with the presence of 0.01M KCl and b) KCl concentration at pH 5.6. As pH increases, both the repulsion between particles and the attraction between the membrane and particles increase. As KCl concentration increases, the repulsion between particles converts to be attraction and the attraction between the membrane and particles converts to be repulsion.

According to the obtained results, in the presence of 0.01M KCl, a repulsive energy barrier was found between latex particles, which slightly increased as pH increased (Figure 4-6a). This presence of repulsive forces between the latex particles resists the formation of aggregates. This

can explain the previous measurements that showed the particle size was around 0.4 μm, directly corresponding to the nominal particle size at 0.01M KCl. As the KCl concentration was increased from 0.01M to 1M, the energy barrier disappeared, and attractive forces were present between the particles. This is again consistent with the measured particle size of 0.8 μm at 1 M KCl (Figure 4-4). The interaction energies between the membrane and particles were found to be negative in the presence of 0.01M KCl, which means there was attraction between them. This attractive energy slightly increased as pH increased (Figure 4-6c). However, as the KCl concentration increased, energy barriers between membrane and particles occurred at the separation distance of 0.5 nm with 1M KCl, and 1nm at 0.1M KCl. In these cases, repulsive forces between the membrane and the particles could help reduce the deposition of particles on the membrane surface, which will be further discussed in the next chapter.

4.5 Conclusions

pH and ionic strength have shown significant influence on the fundamental interactions of membrane-particle and particle-particle by varying their zeta potential. Latex particles were measured to be negatively charged over all pH and ionic strength. The PES membrane was positively charged in the presence of 0.01M KCl, while it was negatively charged as the concentration of KCl increased to be 0.1M and 1 M (pH of measured solutions was 5.6). As pH increased, latex particles were more negatively charged with the presence, which caused a greater energy barrier between particles. In the presence of 0.01M KCl, the attractive interaction energy between the membrane and particle slightly increased as pH increased. As ionic strength was increased to 0.1 M and 1M KCl, both latex particles and PES membranes were negatively charged. Energy barriers between the membrane and latex particles were obtained. Few reports of calculating the membrane-particle interactions can be found in the current literatures. However, this chapter developed a new approach and for the first time reported the membrane-particle interaction energy by adapting the modified Hogg-Healy-Fuersteneau formula.

Chapter 5 Detailed, Real-time Characterisation of Particle Deposition during Crossflow Filtration as Influenced by Solution Properties

This chapter investigated the detailed structures of the deposit layer on the PES membrane formed during crossflow filtration of 0.4 μm model latex particles. By using the microfluidic system developed in chapter 3, high-resolution and real-time images of the membrane surface were obtained as well as 3D views of the filtration channel. The structural differences of the deposit layer over a range of solution properties, including pH, ionic strength, and feed concentration were determined. Time dependent deposition behaviour has been characterised by surface coverage, deposition volume and normalised deposition volume. Experimental results were then interpreted by the interplay of membrane-particle interactions and particle-particle interactions studied in chapter 4.

This chapter is adapted from a published paper.

Hongzhan Di, Gregory J. O. Martin, Qiang Sun, Donglin Xie, Dave E. Dunstan* "Detailed, real-time characterization of particle deposition during crossflow filtration as influenced by solution properties". *Journal of Membrane Science*, *555*, 115-124.

5.1 Introduction

Membrane fouling due to particle deposition during filtration processes has been shown to be influenced by a wide range of factors such as solution and suspension properties (pH, ionic strength, and feed concentration), operating conditions (flow rate, permeate flux, and transmembrane pressure), particle size and properties, membrane types and properties, and filtration modes (i.e. dead-end or cross-flow) [24, 152]. The influence of these factors on the filtration performance has been reported based on several standard macroscopic characterisations of the filtration process, such as flux-time behaviour and pressure-time behaviour, understanding of which is helpful and essential for setting up certain filtration systems and improving filtration performance [42, 46, 72, 73, 153-155]. Although standard

macroscopic characterisations have successfully demonstrated the influence of variable conditions on flux, the fouling process that governs filtration performance can only be inferred. As reviewed in chapter 2, it has been possible to directly visualise the filtration cell using microscopy [74-78] and microfluidic technology [79-84] to study membrane fouling. By visualising the membrane surface and the deposit layer itself, fundamental information can be obtained for characterising the fouling process during membrane filtration, which complements the characterisation of filtration performance. However, to date it has not been possible to examine individual sub-micron sized particles owing to limitations in the experimental set up (see chapter 2). The development of an experimental combining microfluidics and confocal microscopy in chapter 3, enables a new level of detail to be obtained and the visualisation of individual submicron particles during membrane filtration.

In this work, the fouling process of 0.4 μm model polystyrene particles on a 10kDa ultrafiltration polyethersulfone membrane during cross-flow filtration is studied using this set-up. Time resolved information on the detailed structures and distributions of the deposit layer over a range of solution conditions (pH, ionic strength, and feed concentration) are reported. The results are interpreted using DLVO theory, Van der Waals attraction energy, and modified Hogg-Healy-Fuersteneau (HHF) formula combined with the interplay of membrane-particle interactions and particle-particle interactions to understand the overall deposition behaviour. The relative importance of solution conditions (pH, ionic strength, and feed concentration) on the fouling process is elucidated.

5.2 Materials and Methods

Polyethersulfone (PES) membranes (10 kDa, Koch membrane system Inc.) and fluorescent polystyrene latex particles (0.4 μm diameter, Thermo Scientific Inc.) were used in the filtration process. Potassium chloride (KCl, Chem Supply Inc.) was dissolved in MilliQ water to control the ionic strength of latex suspensions.

To investigate the effect of various solution conditions on the process of particle deposition, the same operating conditions (permeate flux of 25 L/h/m^2, cross-flow velocity of 20 m/h, and temperature of 298.15 K) were used for all experiments. For the study of the influence of pH, sodium hydroxide and

hydrochloric acid (Sigma-Aldrich Co. LLC.) were used to adjust pH to 3, 4, 5.6, and 8 (the pH of solutions before adjustment was 5.6 ± 0.2). All latex solutions were prepared by diluting original stock latex suspensions in 0.01M KCl concentrated solutions to 2×10^{-5} in volume fraction. To study the influence of ionic strength, latex solutions were prepared by diluting original stock latex suspensions to a volume fraction of 2×10^{-5} in KCl solutions of 0.01, 0.1, and 1M. To study the influence of feed concentration, latex solutions were prepared by diluting original stock latex suspensions to achieve volume fractions of 0.5, 2, and 8×10^{-5} in 0.01M KCl.

A ZetaSizer Nano (Malvern Instruments Ltd.) and a Zeta potential analyser (Anton Paar GmbH) were used to measure the zeta potential of latex particles and membranes respectively.

5.3 Results and discussions

5.3.1 Effect of pH

The detailed structures and distributions of the deposit layers formed at pH 3, 4, 5.6, and 8 were studied. The feed solutions used in these filtration experiments had a latex particle volume fraction of 2×10^{-5} and KCl concentration of 0.01M. Figures 5-1a, b, c, and d are images of the membrane surface, side view, and 3D view of the channel after 50 minutes of filtration at various pH values. It shows that as pH increased, more individual particles were found at the membrane surface, while the deposited particles were generally less aggregated. At pH 8, the deposition layer was uniform and only equivalent to a monolayer of particles in thickness. As pH decreased, thicker, heterogeneous deposition layers were formed that included particle aggregates that extended out from the membrane surface. Note that 3D images were assembled by a z-stack of 2D images. A distortion (approximately 10-fold) of particles was observed in the z depth (Figure 5-1, 5-4, and 5-6) due to the impact of light scattering and point spreading in the confocal microscopy system.

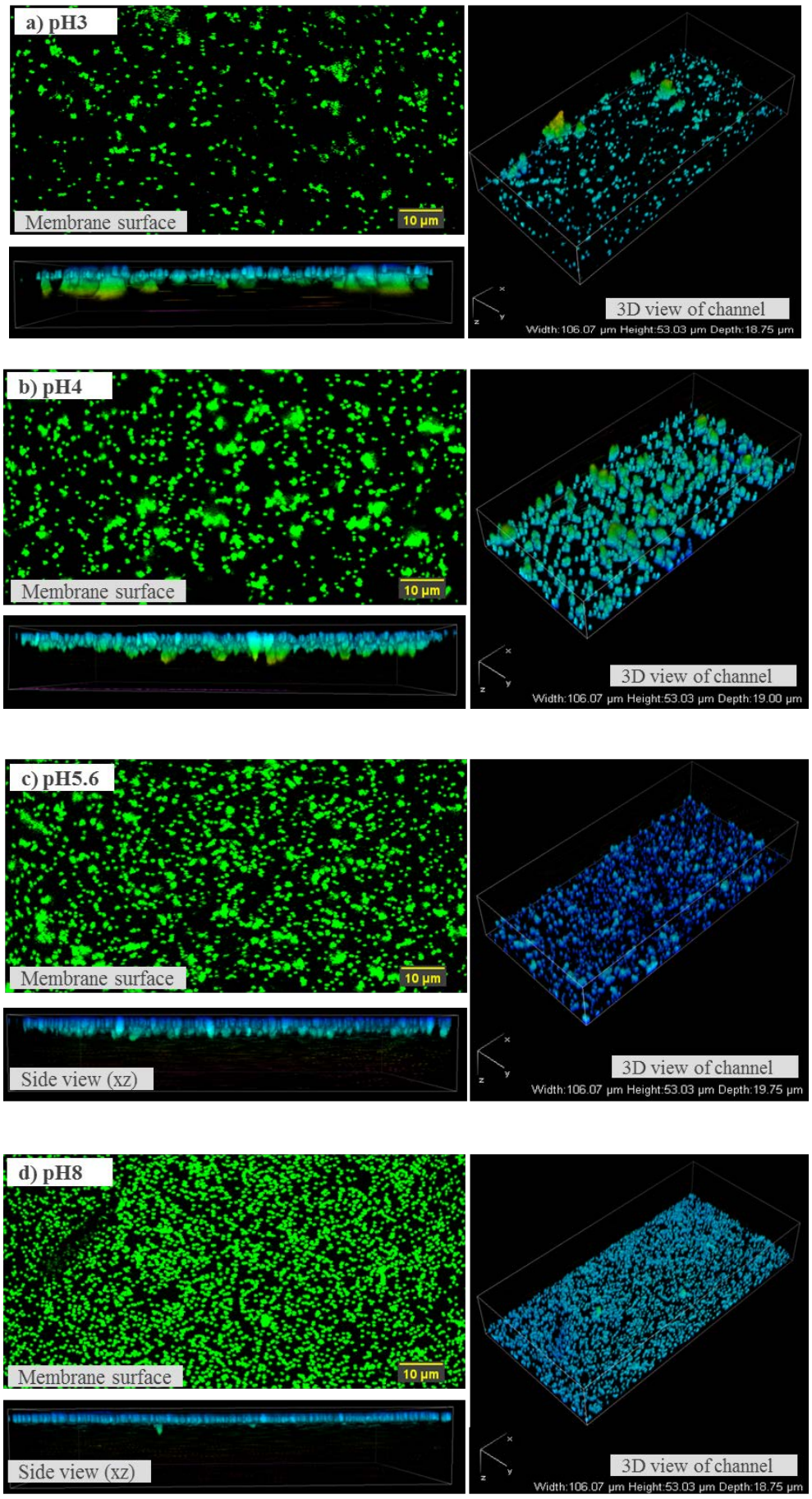
a) pH3
Membrane surface
10 µm
3D view of channel
Width:106.07 µm Height:53.03 µm Depth:18.75 µm
b) pH4
Membrane surface
10 µm
3D view of channel
Width:106.07 µm Height:53.03 µm Depth:19.00 µm
c) pH5.6
Membrane surface
10 µm
Side view (xz)
3D view of channel
Width:106.07 µm Height:53.03 µm Depth:19.75 µm
d) pH8
Membrane surface
10 µm
Side view (xz)
3D view of channel
Width:106.07 µm Height:53.03 µm Depth:18.75 µm

Figure 5-1 Images of the membrane surface, side view, and 3D view of the channel after 50 minutes filtration at a) pH 3, b) pH 4, c) pH 5.6, and d) pH 8. The field of view of the membrane is around 100 µm long and 50 µm wide, and the depth of the channel shown is around 20 µm. The KCl concentration was 0.01M and the volume fraction of latex particle was $\mathbf{2 \times 10^{-5}}$.

Figure 5-2a shows the surface coverage by deposited particles as a function of filtration time and pH. Figure 5-2b shows the volume of deposition per membrane area as a function of filtration time and pH. Both the surface coverage and volume of deposition were found to increase as filtration time increased. It was interesting to see that after 50 minutes of filtration, the highest value of surface coverage occurred at pH 8 (Figure 5-2a), while the highest values of deposition volume occurred at pH 5.6 (Figure 5-2b). This could be explained by considering that although a greater percentage of the membrane surface was covered at pH 8 than at pH 5.6, more aggregates were formed at pH 5.6 that occupy more volume away from the membrane surface (Figure 5-1).

To better understand these results, the proportion of deposited particles that were either individual, isolated particles or part of aggregates were determined and compared at pH 5.6 and pH 8 (Figure 5-2c). It can be seen that isolated particles remained the major deposition form at pH 8 during the whole filtration process. However, at pH 5.6, the majority of deposition switched from isolated particles to aggregates after 10 minutes filtration. Thus, the occurrence of the greatest deposition volume at pH 5.6 could be explained by the interplay of the deposition on the membrane surface and the formation of aggregates.

Figure 5-2d shows that the normalised deposition volume (cumulative volume of deposition normalised by the cumulative volume of solute towards the membrane) decreased as filtration time increased. The initial deposition behaviour was significantly affected by pH conditions, where the highest and lowest normalised deposition volume after 10 minutes of filtration occurred at pH 8 and pH 3 respectively. For long-term filtration, however, the differences caused by differences in pH became less significant.

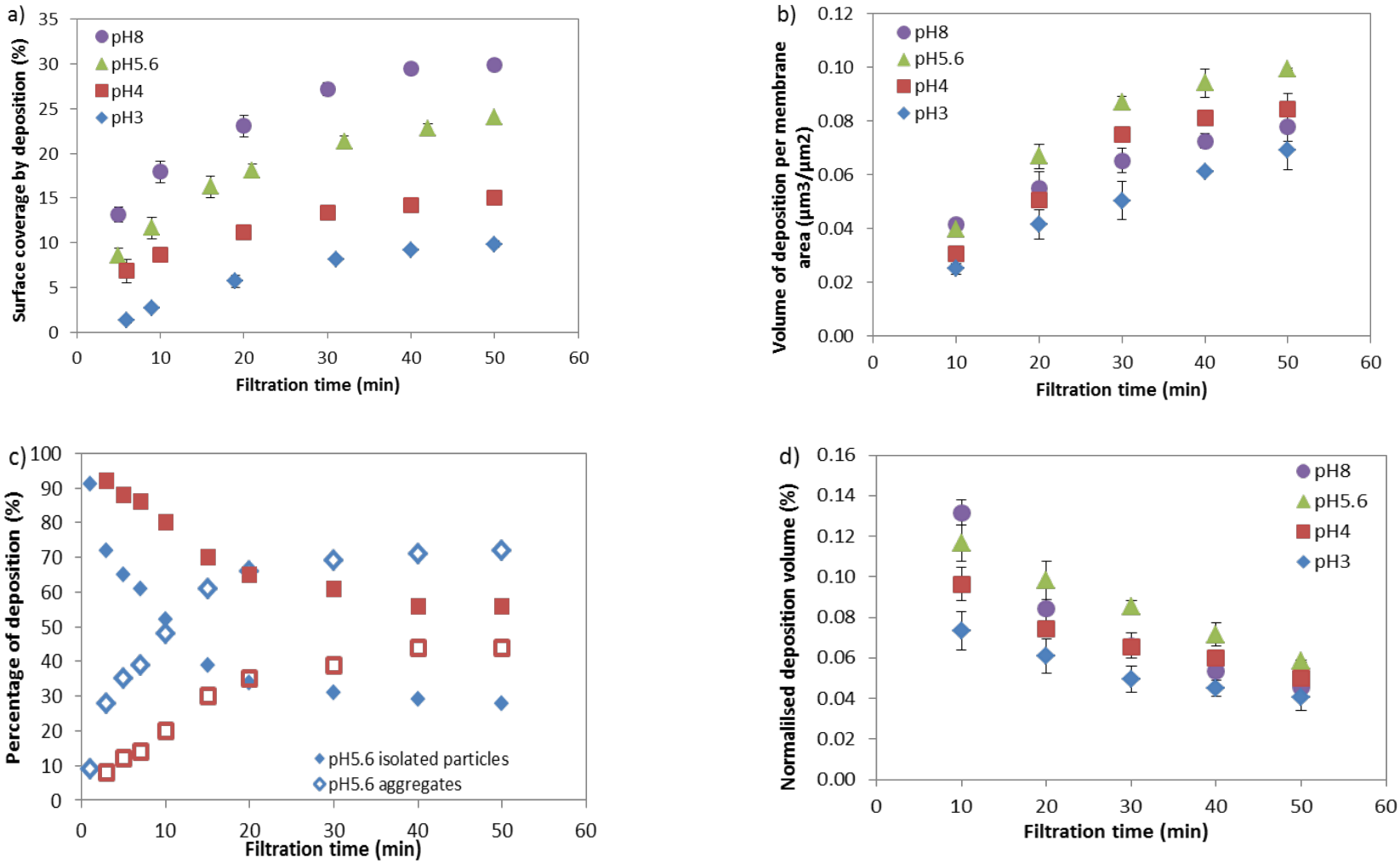

Figure 5-2 a) Surface coverage by deposition and b) volume of deposition per membrane area as a function of filtration time and pH values. c) Percentages of isolated particles and aggregates in the deposition at pH 5.6 (blue diamond symbols) and pH 8 (red square symbols) as a function of filtration time. d) Normalised deposition volume (cumulative volume of deposition normalised by cumulative volume of solute towards the membrane) as a function of filtration time and pH values. The KCl concentration was 0.01M and the volume fraction of latex particles was $\mathbf{2 \times 10^{-5}}$.

To investigate the fundamental mechanisms of particle deposition during membrane filtration, the membrane-particle interaction energy at a distance equal to the Debye length λ, and the particle-particle energy barrier were calculated as a function of pH (Figure 5-3). The membrane-particle interaction energy was determined using equations 1, 2 and 7, where the membrane was assumed to be a particle with infinite radius a_2 (it was assumed that $a_2 = 1000a_1$, where a_1 was the radius of latex particles). The Hamaker constant was chosen to be 1.5×10^{-20} J for the interaction of polystyrene particles and a PES membrane in an aqueous medium [151]. The Debye length λ was calculated to be 3 nm when the KCl concentration was 0.01M. The energy barrier between particles was determined using equations 1, 3 and 6. The Hamaker constant was assumed to be 5×10^{-21}J for polystyrene particles in an aqueous medium [72]. According to the results, as pH increased, the attractive energy between the particles and membrane surface (blue diamond symbols) as well as the particle-particle energy barrier (red square symbols) increased in magnitude.

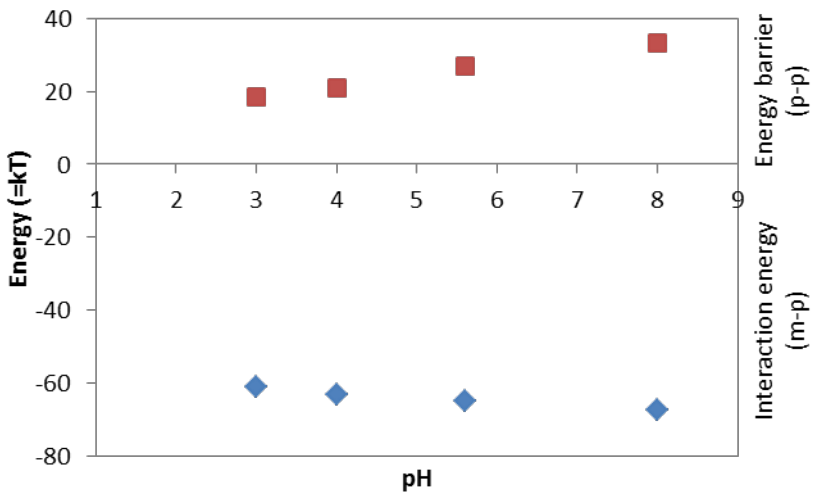

Figure 5-3 Interaction energies between the membrane and particles at a Debye length of 3 nm, and between particles as a function of pH. Red square symbols represent the energy barrier between particles (p-p). Blue diamond symbols represent the interaction energy between particles and the membrane (m-p). The KCl concentration was 0.01M and the volume fraction of latex particles was $\mathbf{2 \times 10^{-5}}$. As pH increases, both the repulsive energy between individual particles and attractive energy between the membrane and particles increase.

Combining the above results, it can be seen that the overall deposition behaviour was significantly influenced by both the deposition at the membrane surface and the formation of aggregates away from the membrane. The initial deposition behaviour (i.e. the first 10 minutes of filtration) was primarily governed by the membrane-particle interactions. Increasing the pH resulted in greater membrane-particle attraction energy (Figure 5-3), which caused more deposition at the membrane surface (Figure 5-1 and 5-2a). However, as filtration time increased, long-term deposition behaviour was dominated by the particle-particle interactions, where the already deposited particles acted as seed for the formation of aggregates. As the pH increased, the energy barrier between particles increased (Figure 5-3) meaning less aggregation occurred, which was consistent to the experimental observations (Figure 5-1).

In previous studies using BSA as model foulant [42, 136, 143, 156], greatest flux decline was observed at the isoelectric point (IEP), where the intermolecular electrostatic repulsion between foulant and deposited-foulant was at minimal and therefore the foulant aggregration was highest. Following that, it would be expected that the greatest particles deposition, which gives the lowest flux, should occur at the lower pH (pH 3 in this work) where the repulsion between the particles is at the minimal (more particles aggregation). Instead, the greatest amount of deposition was observed at pH 5.6. This can be explained by the interaction between the membrane and particles, which was not a consideration in the previous studies. In this work, we found that the initial membrane deposition is primarily governed by membrane-particle interactions, whereas the long-term deposition was mainly affected by particle-particle interactions. This is because after the membrane is initially saturated with particles, additional particles can only deposit via particle-particle interactions. Due to the low feed volume fraction used in this study, it is likely that the membrane was not fully covered and therefore the membrane-particle interactions dominated. Under this condition, the membrane and particles became more strongly attracted as the pH was increased, and therefore more particles deposition on the membrane can be expected. However, this was counteracted by the aggregation status of the particles as the particles were less likely to aggregate at higher pH, which decreased the deposition. Thus, a maximal deposition was observed

between pH 3 and 8 (pH 5.6). It is possible that for a given long filtration time, the membrane surface has been already covered by particles, and particles arriving at the membrane can only deposited on the already-deposited-particles. Thus, the influence of membrane-particle interactions can be significantly shielded by the particle-particle interactions, and the greatest amount of deposition could be found at pH 3. In addition, the feed volume fraction in this work is relatively low, which also extends the “given long filtration time”.

5.3.2 Effect of ionic strength

The effect of ionic strength was studied with different ionic concentrations (0.01M, 0.1M and 1M KCl) at pH 5.6. The volume fraction of latex particles was 2×10^{-5}. Figure 5-4 presents images of the membrane surface, side view and 3D view of the microfluidic filtration device after 50 minutes of filtration. The structures of the deposit layer and the deposit distribution were found to be considerably different at different ionic strengths. Compared to the more homogeneous deposit layer at 0.01M KCl (Figure 5-4a), the depositions observed at 0.1M and 1 M KCl (Figure 5-4b and c) were more heterogeneous. In addition, at 1M the total deposition was significantly lower than at 0.01M, although more aggregates were formed.

The change in surface coverage, volume of deposition per membrane area, and normalised deposition volume as a function of filtration time and ionic strength were plotted in Figure 5-5, all of which decreased as KCl concentration increased. Interestingly, the normalised deposition volume in the presence of 1M KCl was independent of filtration time and was considerably lower (close to zero) than at 0.01M KCl.

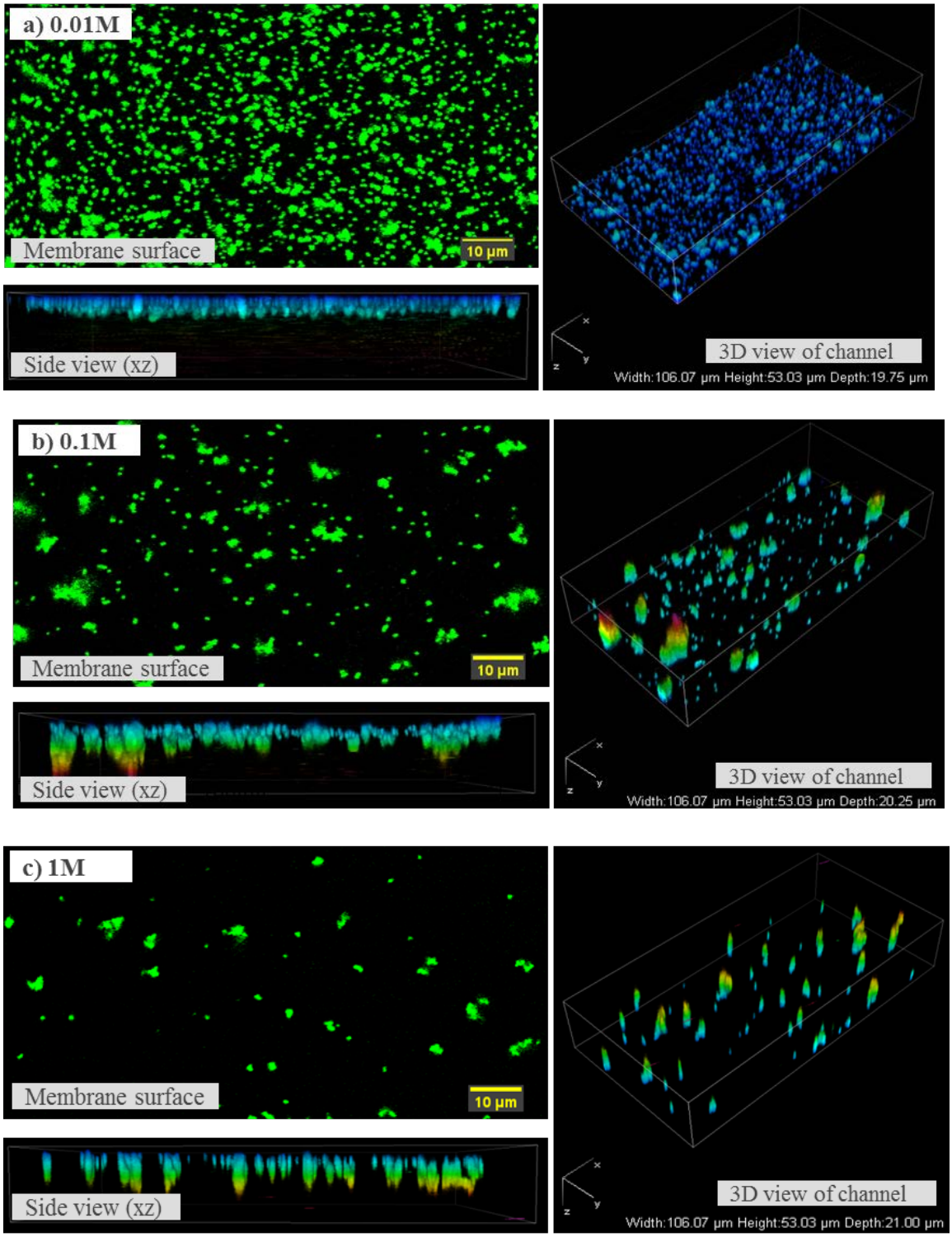

Figure 5-4 Images of the membrane surface, side view, and 3D view of channel after 50 minutes filtration when the KCl concentration was a) 0.01M, b) 0.1M, and c) 1M in the feed solution (Fig.5-4a is the same with Figure 5-1c). Less deposition and more aggregates are found at higher KCl concentration. The field of view of the membrane is around 100 µm long and 50 µm wide, and the depth of the channel shown is around 20 µm. The pH was 5.6 and the volume fraction of latex particle was $\mathbf{2 \times 10^{-5}}$.

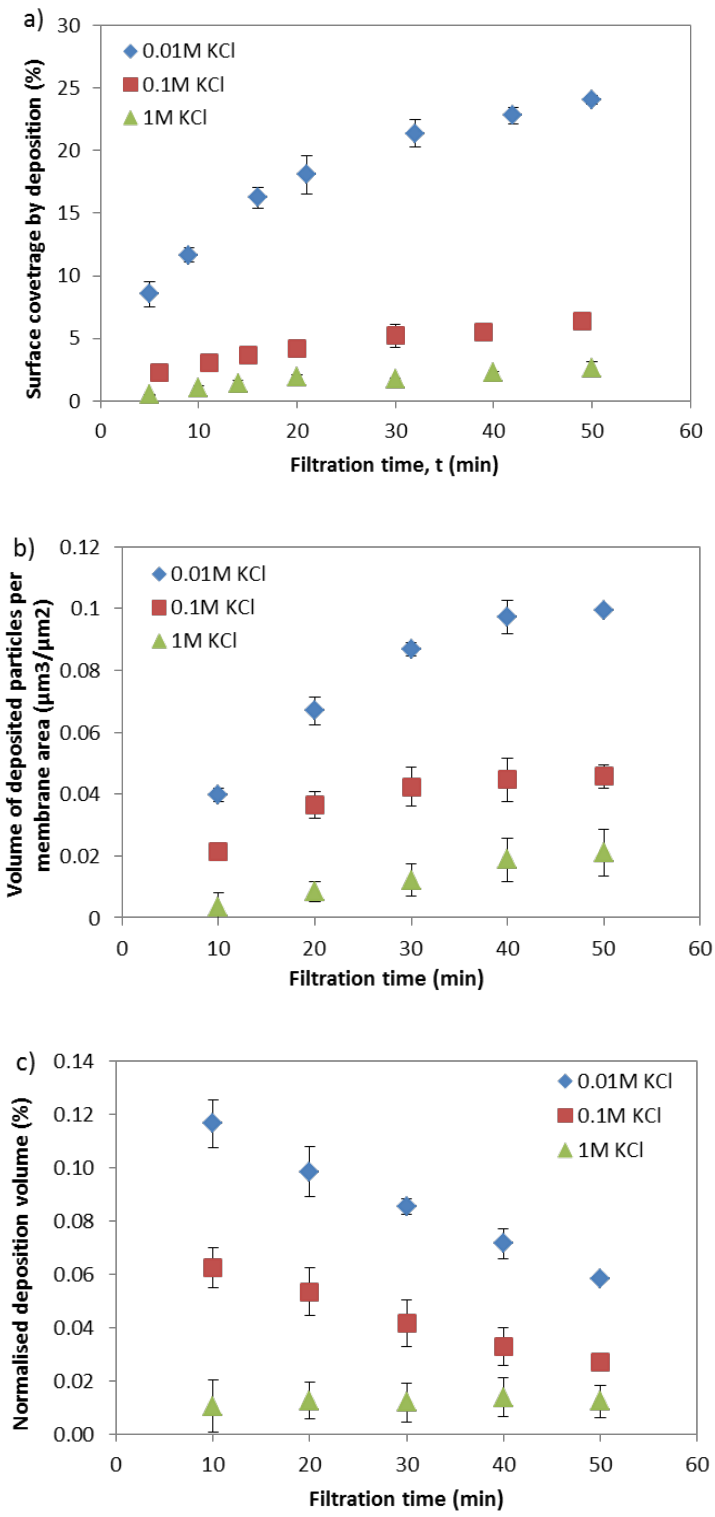

Figure 5-5 a) Surface coverage by deposition, b) volume of deposition per membrane area, and c) normalised deposition volume (cumulative volume of deposition normalised by cumulative volume of solute towards the membrane) as a function of filtration time and KCl concentration. The pH was 5.6 and the volume fraction of latex particle was $\mathbf{2 \times 10^{-5}}$. As filtration time increases, surface coverage and deposition volume increase, while normalized deposition volume

decreases. Increasing KCl concentration decreases surface coverage, deposition volume and normalised deposition volume.

Numerous studies of the effect of ionic strength on macroscopic flux measurements have been published. Some studies reported that more severe fouling occurred at higher ionic strength, due to the electric double layer compression (EDL) which allows the foulant getting close and attracting each other [43, 47, 140]. While other studies reported that less fouling was observed as ionic strength increased [39, 42, 48]. She et al. found greater permeate flux at higher ionic strength during filtration of BSA solutions at pH 5.8. The proposed reason was that the solubility of BSA increased as the salt concentration increased. The observed low BSA retention in their research corresponded to this explanation [42].

Most of these studies only considered membrane fouling as a function of particle-particle (foulant-foulant) interactions, while the membrane-particle interactions were omitted. In this work, we have shown that the deposit layer structures and deposition behaviours under various ionic strengths can be significantly affected by the interactions between the membrane and particles. In the presence of 0.01M KCl, the membrane was positively charged, and particles were negatively charged (Figure 4-5). The interaction between the membrane and particles was therefore attractive promoting particles to deposit on the membrane surface (Table 5-1). At KCl concentration of 0.1M and 1M, the membrane was slightly negatively charged and highly negatively charged respectively (Figure 4-5), thus resulting in repulsive electrostatic energy barriers that help resist particle deposition on the membrane surface. However, more particle aggregates were observed with 0.1M and 1M KCl, which could be explained by the reduction of repulsive electrostatic energy between particles as a function of increasing ionic strength (Table 5-1).

Table 5-1. Summary of the results obtained at various ionic strengths**.** The pH was 5.6 and the volume fraction of latex particles was $\mathbf{2 \times 10^{-5}}$.

KCl concentration (M)	Area fraction (%)	Overall volume ($\mu m^3/\mu m^2$)	Membrane-Particle		Particle-Particle
			Energy barrier (k_BT)	Critical velocity (m/s)	Energy barrier (k_BT)
0.01	12.5	34.0	Attractive	-	27
0.1	5.03	20.0	1.79	2.3×10^{-3}	Attractive
1	1.75	9.96	8.88	7.4×10^{-2}	Attractive

The particle-membrane energy barriers at 0.1 M and 1 M were approximately 2 k_BT and 9 k_BT respectively (Table 5-1). According to equation 8, the net hydrodynamic force was calculated to be 2.3×10^{-14} N, where the transmembrane velocity was 1.4×10^{-5} m/s as determined from the permeate flux. The corresponding hydrodynamic energies available to drag particles, at a distance of the Debye length away from the membrane surface, were 0.01 kT and 0.004 kT for 0.1M and 1M respectively. The barrier energies were greater than the hydrodynamic energies, consistent with the observation that particle deposition was relatively minimal. The critical transmembrane velocities (transmembrane fluid velocity at which the net hydrodynamic drag force is equal to the barrier force) were calculated to be 2.3×10^{-3} and 7.4×10^{-2} m/s for 0.1M and 1M respectively by dividing the barrier energy by the separation distance between the membrane and particles (Debye length was taken as the separation distance in this work). The experimental velocity 1.4×10^{-5} m/s was smaller than the critical velocities, helping to explain the minimal extent of particle deposition at the higher ionic strengths. The small amount of particle deposition that was observed on the membrane at 0.1 M and 1 M was likely due to the heterogeneity of both the membrane surface and the hydrodynamic conditions, which was also reported by Tang et al. [43].

5.3.3 Effect of feed concentration

The images of the membrane surface, side view, and 3D view of channel with different volume fractions of latex particles after 50 minutes filtration was shown in Figure 5-6. According to the images, it can be found that particles were deposited homogenously on the membrane surface for all conditions, and a greater amount of deposition was observed at higher concentrations as

expected. Figure 5-7 shows the deposition behaviours (surface coverage, volume of deposition per membrane area, and normalised deposition volume) as a function of filtration time and feed volume fraction. As the volume fraction of latex particles increased, a more rapid and extensive deposition was observed. This was likely due to the greater flux of latex particles convectively transported towards the membrane surface. In addition, a higher feed concentration increases the probability of collision between latex particles and the membrane surface. However, it might be expected that given filtration times were in proportion to the flux, the accumulated deposition may not be dependent on the feed concentration. This was indeed found to be the case, with similar values of normalised deposition volume under various feed volume fractions were obtained, indicating that the deposition behaviour was not strongly influenced by the feed volume fraction.

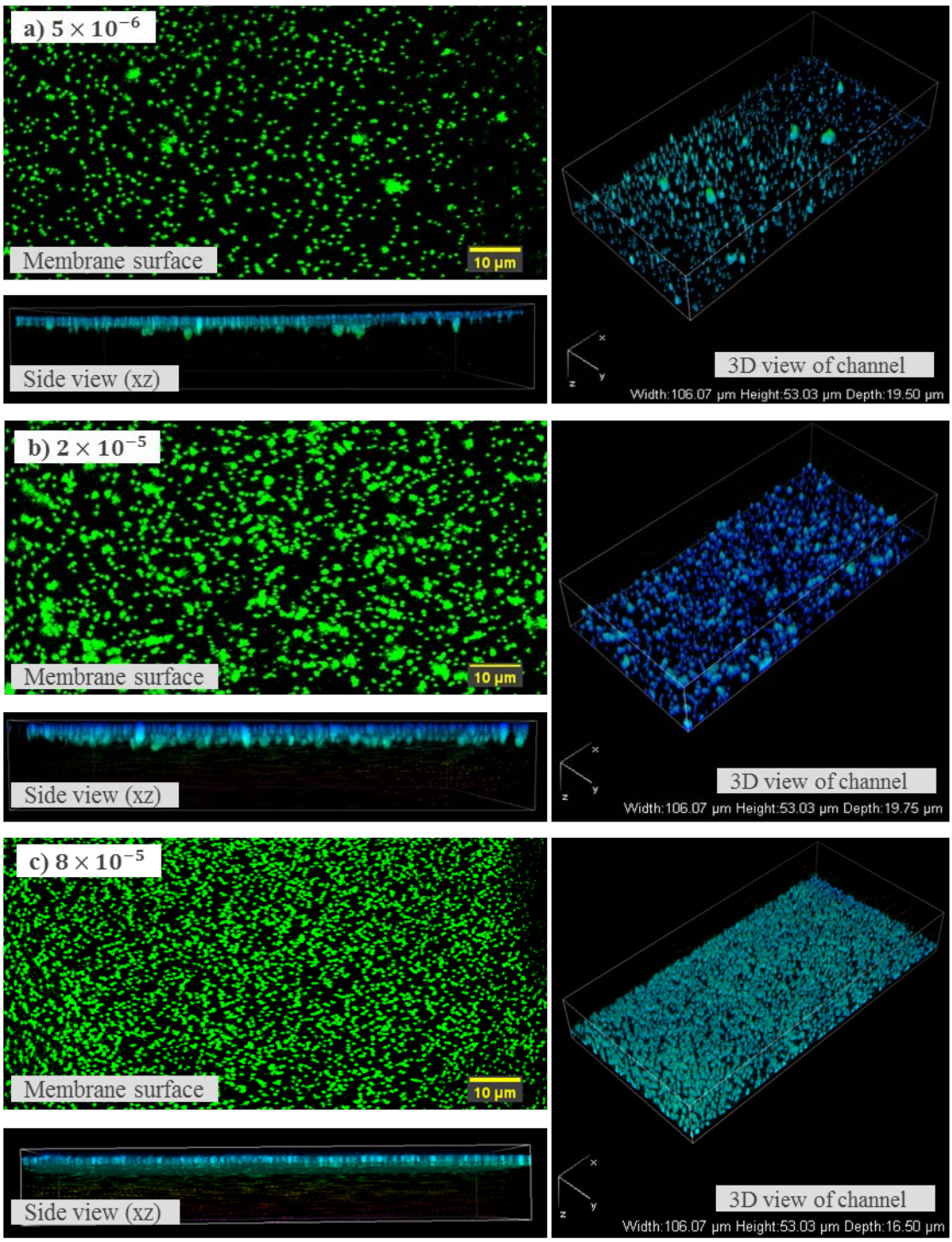

Figure 5-6 Images of the membrane surface, side view, and 3D view of channel after 50 minutes filtration with particle volume fraction of a) $\mathbf{5 \times 10^{-6}}$, b) $\mathbf{2 \times 10^{-5}}$, and c) $\mathbf{8 \times 0^{-5}}$ (Figure 5-6b is the same with Figure 5-1c). The field of view of the membrane is around 100 µm long and 50 µm wide, and the depth of the channel shown is around 20 µm. The pH was 5.6 and he KCl concentration was 0.01M.

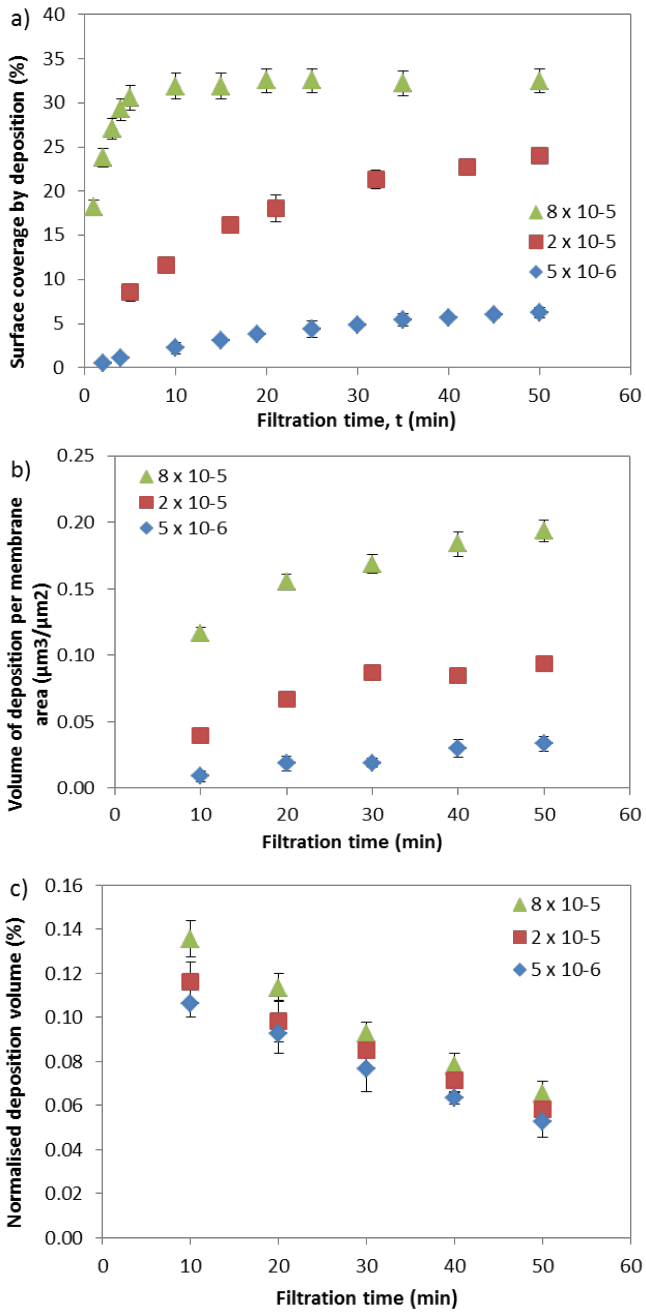

Figure 5-7 a) Surface coverage by deposition, b) volume of deposition per membrane area, and c) normalised deposition volume (cumulative volume of deposition normalised by cumulative volume of solute towards the membrane) as a function of filtration time and volume fraction of particles in the feed. The pH was 5.6 and KCl concentration was 0.01M. As filtration time increases, surface coverage and deposition volume increase, while normalised deposition volume decreases. Increasing volume fraction increases surface coverage and deposition volume while barely affects normalised deposition volume.

5.4 Summary for all conditions

The deposition process during membrane filtration can be influenced by a range of solution factors, including pH, ionic strength, and feed concentration. Overall, the results presented here, illustrate the importance of the interplay of membrane-particle interactions and particle-particle interactions in determining the deposition process. Deposition was found to increase at higher pH, greater feed concentrations, and lower ionic strengths. These results help explain why varying solution conditions can significantly influence the initial deposition process, while having less of an impact on long-term (steady state) deposition behaviour.

When the pH was varied, the greatest surface coverage by deposition was found to occur at pH 8. This was due to the membrane and particles having the highest attraction at this pH. However, the greatest volume of deposition occurred at pH 5.6, where more particle aggregates were formed due to the reduced repulsion between particles at this pH. This study revealed that the deposit layer structures were significantly different as a function of varied ionic strength. In the presence of 0.01M KCl, where the membrane was positively charged, and particles were negatively charged, a greater amount of deposition and a homogeneous deposit layer were obtained. While in the presence of 1M KCl, where both the membrane and particles were negatively charged, considerably less deposition was observed due to the repulsive energy resisting particle deposition onto the membrane surface. Deposition behaviour, as characterised by the normalised deposition volume, was found to be highly influenced by ionic strength, while barely influenced by the particle concentration of the feed.

5.5 Conclusions

The deposition process of 0.4 μm polystyrene particles on ultrafiltration membranes during cross-flow filtration was studied. Time-sequenced and high-resolution images of the membrane surface, side views and 3D views of the filtration channel were obtained using a microfluidic filtration system. The detailed structures of the deposit layer and deposition distribution over a range of pH, ionic strength, and feed concentration conditions were determined. The initial deposition kinetics was dominated by the particle-membrane interactions and particle-particle interactions. The long

term (steady state) deposition behaviour revealed that the normalised deposition volumes were largely independent of the solution conditions.

The overall deposition behaviours were characterised on the basis of time dependent surface coverage, deposition volume and normalised deposition volume. These detailed, time-resolved experimental data provide a solid foundation for the development and improvement of theoretic models describing membrane fouling. Future investigations can build on this knowledge with further examination into the effects of varying crossflow velocity and particle properties on membrane fouling.

Chapter 6 Effect of Operating Conditions on Particle Deposition and Development of an Empirical Correlation Describing the Dynamic Deposition Behaviour

In addition to being influenced by solution properties, membrane fouling is also significantly affected by operating conditions. Using the developed microfluidic filtration system, detailed examinations of membrane fouling under various permeate flux and crossflow velocity conditions were studied in this chapter. The probability of particle deposition during crossflow filtration was determined based on the hydrodynamic forces acting on the particles. Building on the experimental results obtained from chapter 4, chapter 5, and this chapter, an empirical correlation was developed for describing the dynamic deposition volume in terms of both interaction energies (influenced by solution properties) and hydrodynamic forces (influenced by operating conditions).

This chapter is adapted from a manuscript in preparation for submission to a membrane science journal. Hongzhan Di, Gregory J. O. Martin, Yong Wang, Dave E. Dunstan* "Effect of operating conditions on particle deposition and development of an empirical correlation describing the dynamic particle deposition".

6.1 Introduction

The previous chapter studied the influence of solution properties on membrane fouling. The current chapter focuses on the investigation of the key roles of operating conditions acting on the fouling process during crossflow filtration. Many theoretical approaches to predicting the rate of flux decline have been developed and verified for certain types of process feeds under certain conditions [157]. Amongst these, an empirical correlation has been developed to predict particle deposition probability as a function of hydrodynamics [158]. This empirical model was able to represent experimental macroscopic membrane performance data, however it has not yet been tested on individual particle deposition. In this work, the model of Stamatakis and Tien [158] was incorporated into the development of an empirical correlation for predicting the dynamic time-dependent deposition behaviours over a range of operating conditions that were characterised by deposition probability, and solution properties that were characterised by interaction energies.

6.2 Theory

In the current chapter, the focus is on the influence of hydrodynamic forces on particle deposition under various operation conditions. To help describe the relationship between filtration parameters and particles deposition, an semi-empirical model [158] is applied that relates the probability of particle deposition to hydrodynamic factors. Figure 6-1 shows a schematic diagram showing the forces acting on a single particle during crossflow membrane filtration, relevant to this model. Along the x-direction (main flow direction), there is a drag force F_x exerted on the particle, which is caused by the crossflow. Along the y-direction (permeate direction), there are three forces acting on the particles: F_{yP} (drag force caused by the permeate flow), F_{yL} (lateral lift force caused by the crossflow), and F_{yB} (buoyancy force of the particle). The net force acting on the particle along the y-direction, F_y, is:

$$F_y = F_{yP} - F_{yL} + F_{yB} \tag{6-1}$$

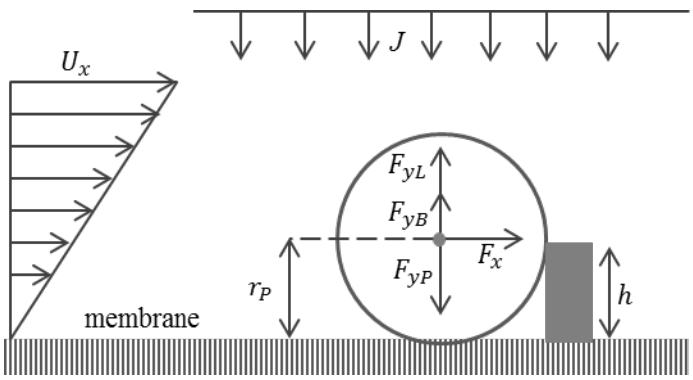

Figure 6-1 Image showing the forces acting upon a spherical particle in contact with a protrusion of height h. The particle is subjected to forces along the x-direction (main flow direction) and y-direction (permeate flow direction).

6.2.1 Hydrodynamic force determination

Along the x-direction, the drag force exerted on a particle in a shear flow field is expressed as follows [159],

$$F_x = 1.7009 \cdot 6\pi\eta r_P U_x \tag{6-2}$$

Where η is the fluid viscosity; r_P is the radius of the particle; The constant 1.7009 accounts for the effect of the surface on the drag force acting on a particle in contact with a plane [160]; U_x is the crossflow velocity,

$$U_x = \frac{6Q}{WH^3}\left[\frac{H^2}{4} - \left(\frac{H}{2} - r_P\right)^2\right] \tag{6-3}$$

where Q is the volumetric flow rate; W is the filtration channel width; H is the filtration channel height. Along y-direction, the drag force exerted on a particle caused by the permeate flow is proportional to the flux J (permeate velocity) according to the Stokes' Law:

$$F_{yP} = 6\pi\eta r_P J \tag{6-4}$$

The lateral lift force due to the shear flow has been reported to be calculated as follows [110]:

$$F_{yL} = 0.761\frac{{\tau_w}^{1.5}{r_P}^3\rho^{0.5}}{\eta} \tag{6-5}$$

Where ρ is the density of the fluid; τ_w is the wall shear stress, which can be calculated from the friction factor correlation f, or given as follows for laminar flow [158]:

$$f = \frac{2\tau_w}{\rho v^2} = \frac{24}{Re} \tag{6-6}$$

Where v is the mean velocity of the fluid; Re is the Reynolds number. For a flow in a rectangular channel, Re is generally given as,

$$Re = \frac{\rho v D_H}{\eta} \tag{6-7}$$

Where D_H is the hydraulic diameter, which can be obtained from the cross-sectional area A and wetted perimeter of channel walls P:

$$D_H = \frac{4A}{P} \tag{6-8}$$

The buoyancy force on the spherical particle is

$$F_{yB} = \frac{\pi}{6}(\rho_P - \rho) g {r_P}^3 \tag{6-9}$$

For the case that the particle density ρ_p is equal or similar to the liquid density ρ, the buoyancy force is vanishingly small and can be ignored.

6.2.2 Particle deposition probability

As shown in Figure 6-1, the model [158] assumes that a particle of radius r_P is transported to the vicinity of the membrane surface with a protrusion of finite height, h. The protrusion may be considered to be a previously deposited particle, or a protrusion due to roughness or heterogeneity of the membrane. The condition for the particle to deposit, or remain static at the membrane surface can be described as follows (assuming translational movement of the particle in response to the forces and ignoring factors such as friction, rotational movement, and 3-dimensional geometric interactions between the particle and protrusion) [158]:

$$F_y\sqrt{{r_P}^2 - (r_P - h)^2} \geq F_x(r_P - h)$$

or

$$h \geq r_P\left(1 - \frac{1}{\sqrt{(F_x/F_y)^2 + 1}}\right) \tag{6-10}$$

Consequently, a minimum protrusion height, h_{min}, above which deposition takes place, can be derived from the above relationship, namely,

$$h_{min} = r_P\left(1 - \frac{1}{\sqrt{(F_x/F_y)^2+1}}\right) \tag{6-11}$$

For a given particle transported to the membrane surface, the probability of being deposited at the membrane surface, equals the probability of there being a local protrusion with a height greater than or equal to h_{min}, P ($h \geq h_{min}$), in other words,

$$\gamma = P(h \geq h_{min}) = 1 - P(h \leq h_{min}) \tag{6-12}$$

where γ is the probability of a spherical particle being deposited at the membrane surface. For a population of particles transported to the membrane surface during crossflow filtration, γ may be taken as the fraction of the population of particles which become deposited. If one assumes that the protrusion height was a continuous random variable, which follows a uniform distribution over $0 \leq h \leq h_{max}$ (h_{max} is the maximum protrusion height), then,

$$P(h \leq h_{min}) = \frac{h_{min}}{h_{max}} \tag{6-13}$$

and it follows that Eq.6-14 can be derived [158],

$$\gamma = 1 - \left(1 - \frac{1}{\sqrt{(F_x/F_y)^2+1}}\right)\frac{r_P}{h_{max}} \tag{6-14}$$

The deposition probability γ would take a value of zero for no deposition (i.e. an individual particle will pass through the filtration channel without being deposited) and a value of one for complete deposition (deposition is assumed here to be permanent, so that once deposited the particle cannot be released).

If F_x = 0, there is no crossflow velocity and dead-end filtration occurs. As the particle would completely be deposited, then γ =1. If F_y = 0, there is no permeate flow. As the particle would flow along the channel with no deposition, then γ = 0. According to the above relationship (if F_y = 0, then γ = 0), the h_{max} should be equal to r_p. Therefore, Eq.13 can be simplified to,

$$\gamma = \frac{F_y}{\sqrt{{F_x}^2 + {F_y}^2}} \tag{6-15}$$

where F_x represents the drag force along x-direction (main flow direction), and F_y constitutes the net force along the y-direction (permeate flow direction).

6.3 Materials and Methods

The microfluidic filtration system developed in chapter 3 was used to operate filtration experiments. Polyethersulfone (PES) membranes (10 kDa, Koch membrane system Inc.) and model fluorescent polystyrene latex particles (0.4 μm, Thermo Scientific Inc.) were used in the filtration process. Potassium chloride (KCl, Chem Supply Inc.) was used to control ionic strength of latex suspensions. ZetaSizer Nano (Malvern Instruments Ltd.) was used to measure the zeta potential of latex particles.

To investigate the effect of various operation conditions on the process of particle deposition, the same solution conditions were used for all experiments. The latex solutions were prepared by diluting the original stock latex suspensions in 0.01M KCl concentrated solutions to 20ppm, and the measured pH was 5.6 ± 0.2 for all solutions.

6.4 Results

6.4.1 Effect of permeate flow rate

The deposit layer structures were studied at 12.5, 25, and 75 L/h/m^2 under constant crossflow velocity of 20 m/h during ultrafiltration. Figure 6-2 presents images of the membrane surface, side view and 3D view of the channel after 50 minutes of filtration. According to the images, a greater amount of deposition on the membrane surface was observed as the permeate flux increased, and more aggregates and a thicker deposit layer were evident. A distortion (approximately 10-fold) of particles was observed in the z depth for Figure 6-2 and Figure 6-4 due to the impact of light scattering and point spreading in the confocal microscopy system.

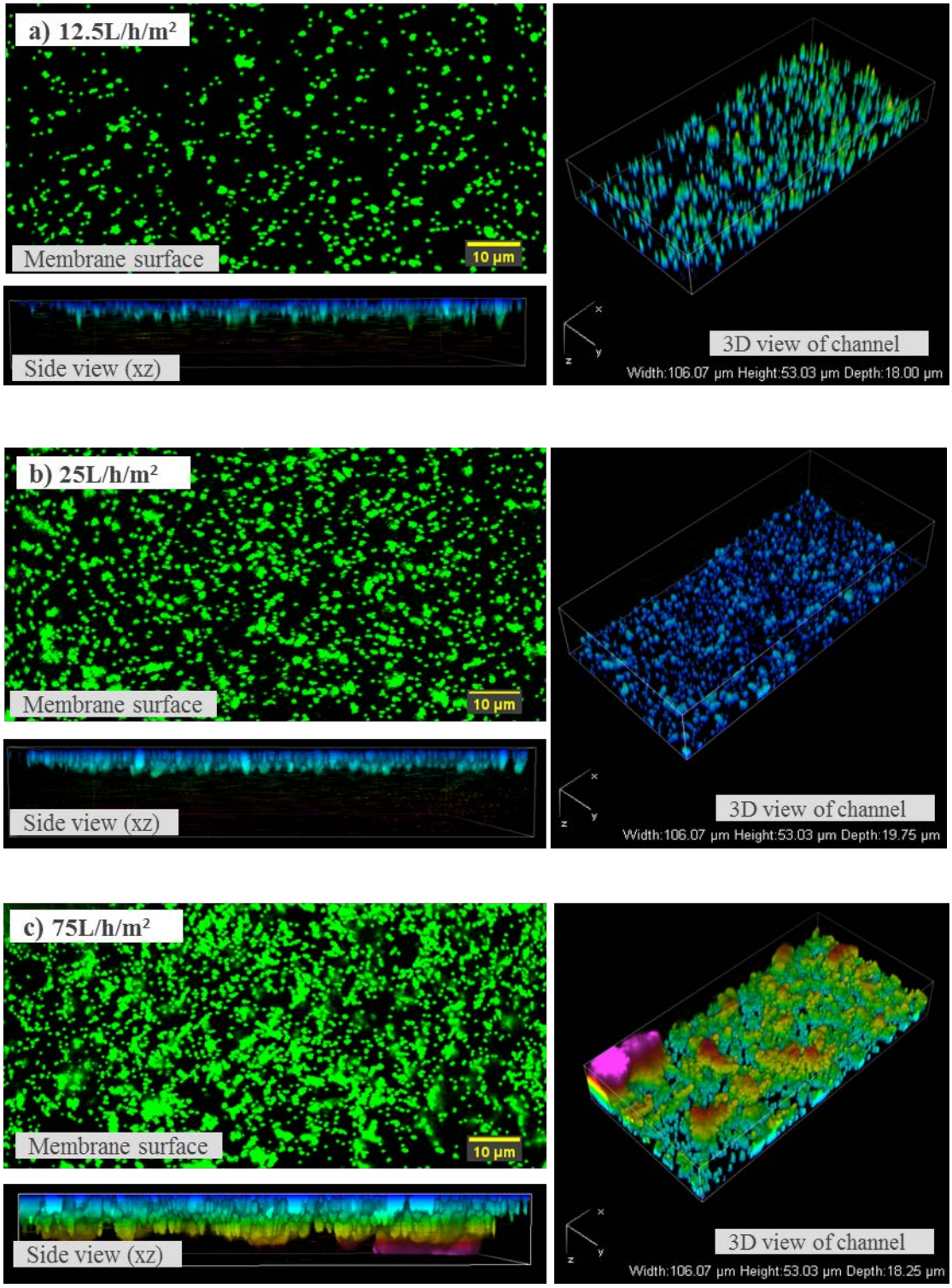

Figure 6-2 Images of the membrane surface, side view, and 3D view of channel after 50 minutes filtration with a permeate flux of a) 12.5 L/h/m^2, b) 25 L/h/m^2, and c) 75 L/h/m^2. The crossflow velocity is 20 m/h. The field of view of the membrane is around 100 µm long and 50 µm wide, and the depth of the channel shown in is around 20 µm. As permeate flux increases, more deposition is observed as well as more dense deposit layer.

Figure 6-3a and b show the surface coverage by deposition and the volume of deposition per membrane area as a function of filtration time and permeate flux. Both increased as permeate flux increased. The deposition behaviour of the latex particles on the membrane appears to be dependent on the permeate flux. Both the surface coverage and deposition volume increased as permeate flux increased, which can be explained by the higher hydrodynamic force along the permeate flow direction (F_{yP} in Figure 6-1) dragging particles towards the membrane surface and already deposited particles. Further, as the permeate flux increased, a greater number of particles will be convectively transported towards the membrane surface for any given filtration time, which increases the probability of collision between the particles and the membrane, and between free particles and previously-deposited-particles.

Comparing the influence of permeate flux on surface coverage and deposition volume, it can be found that by doubling the flux velocity from 12.5 to 25 L/h/m^2, the surface coverage was increased by over two fold (10% to 24% surface coverage after 50 minutes filtration time). A further three-fold increase in flux velocity (25L to 75L) only resulted in a 1.5-fold increase in surface coverage (~35% coverage) indicating a potential saturation effect (Figure 6-3a). However, an analysis based on the volume-basis revealed that there was actually a great than three-fold increase in particle deposition from 25 to 75 L/h/m^2 after 50 minutes of filtration (Figure 6-3b). These observations suggest that at high flux velocity, the surface available for particle deposition becomes limited, however, the latex particles were able to deposit on already deposited particles by forming aggregates and thicker deposit layers, which is consistent to the observations in Figure 6-2.

.

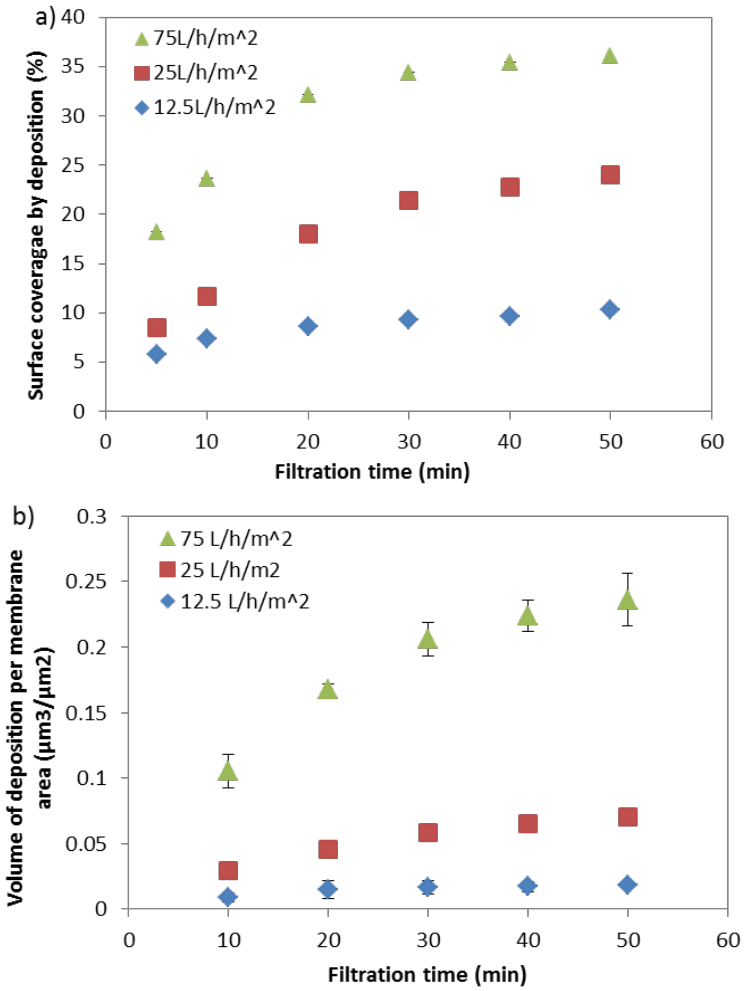

Figure 6-3 a) Surface coverage by deposition, and b) volume of deposition per membrane area as a function of filtration time and permeate flux. The crossflow velocity is 20 m/h. Both of surface coverage and deposition volume increase with increasing filtration time and increasing permeate flux.

6.4.2 Effect of cross-flow velocity

The images of the membrane surface, side view and 3D view of channel after 50 minutes filtration at different cross-flow velocities with a permeate flux of 25 L/h/m^2 are presented in Figure 6-4 (images at a crossflow velocity of 20 m/h are presented in Figure 6-2b). Overall, as crossflow velocity increased, less deposition was observed on the membrane surface. Certain spots of aggregates were observed for all crossflow velocities. It should be noted that the observed particles were visualised brighter and bigger in this set of experiments than that presented in the last section, which was due to a change in the setting of the confocal microscopy system where higher energy of the scan laser was used.

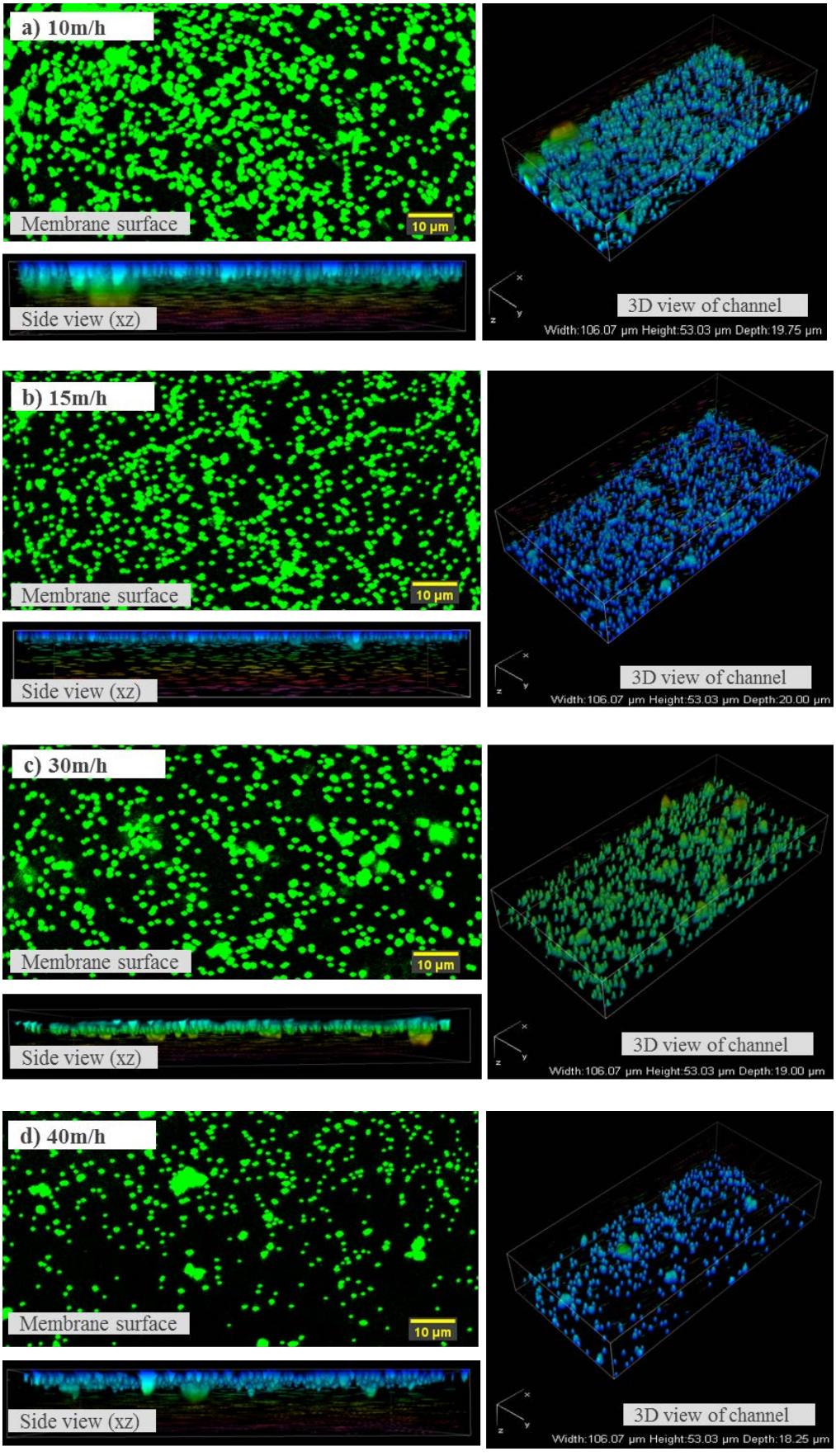
a) 10m/h
Membrane surface
10 µm
Side view (xz)
3D view of channel
Width:106.07 µm Height:53.03 µm Depth:19.75 µm
b) 15m/h
Membrane surface
10 µm
Side view (xz)
3D view of channel
Width:106.07 µm Height:53.03 µm Depth:20.00 µm
c) 30m/h
Membrane surface
10 µm
Side view (xz)
3D view of channel
Width:106.07 µm Height:53.03 µm Depth:19.00 µm
d) 40m/h
Membrane surface
10 µm
Side view (xz)
3D view of channel
Width:106.07 µm Height:53.03 µm Depth:18.25 µm

Figure 6-4 Images of the membrane surface, side view, and 3D view of channel after 50 minutes filtration at crossflow velocity of a) 10m/h, b) 15 m/h, and c) 30m/h, d) 40 m/h. Images at a crossflow velocity of 20 m/h is presented in Figure 6-2b. The permeate flux is 25 L/h/m^2. The field of view of the membrane is around 100 µm long and 50 µm wide, and the depth of the channel shown in is around 20 µm.

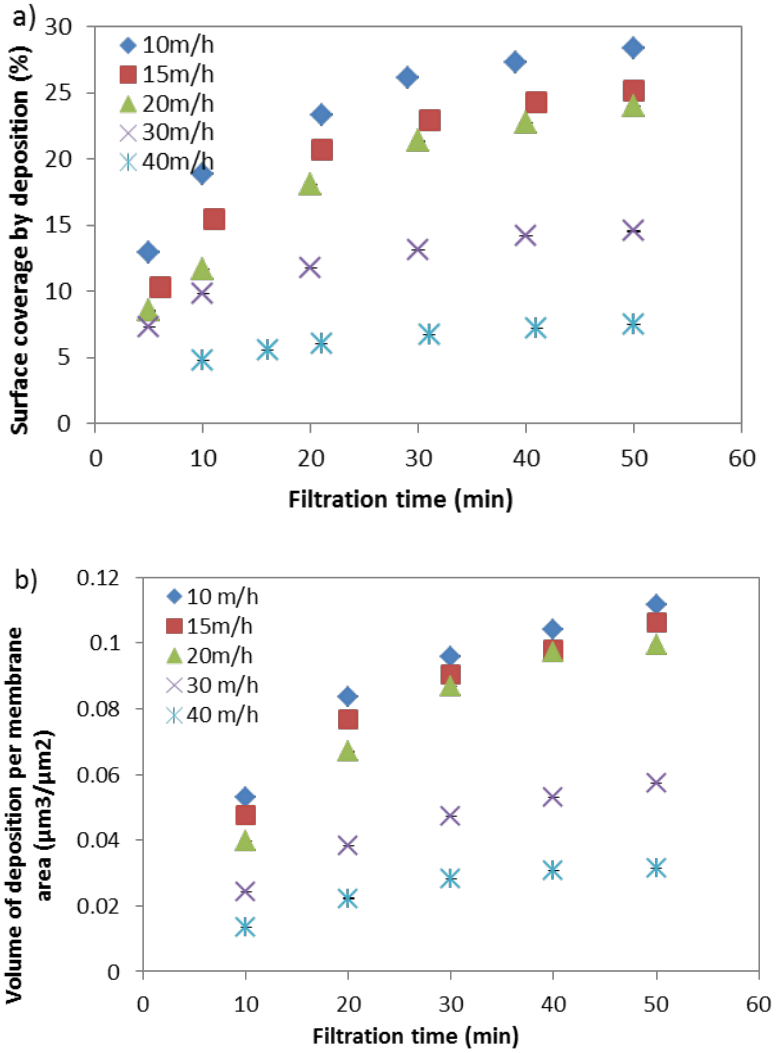

Figure 6-5 a) Surface coverage by deposition and b) deposition volume as a function of filtration time and crossflow velocity. Both surface coverage and deposition volume increase with increasing filtration time and decreasing crossflow velocity.

Figure 6-5 shows the surface coverage by deposition and volume of deposition per membrane area as a function of filtration time and crossflow velocity. Both the surface coverage and deposition volume decreased as the crossflow velocity increased. It was interesting to see that at

lower crossflow velocity, the deposition behaviours were quite similar, where slightly decreasing surface coverage and deposition volume were observed from 10 m/h to 20 m/h. However, over 20 m/h, the surface coverage and deposition volume significantly decreased as crossflow velocity increased.

To better understand the influence of velocity on the deposition process, values of surface coverage and deposition volume after 50 minutes of filtration were plotted as a function of crossflow velocity (Figure 6-6). It shows that surface coverage and deposition volume gradually decreased at lower crossflow velocities and rapidly decreased once the crossflow velocity was greater than 20 m/h. This result indicates that a lower-bound critical crossflow velocity occurs (between 15 and 20 m/h in the current work), above which, particle deposition on the membrane significantly decreases as the crossflow velocity increases. Below this threshold velocity, the induced shear force along the crossflow direction (F_x in Figure 6-1) is presumably insufficient to sweep particles away from the membrane. This contrasts with a previously observed upper-bound critical velocity, above which, further increases in velocity had little effect on the flux [161]. The critical velocity reported in their work was around 10 times the value found in the current study, which is beyond the highest crossflow velocity accessible in our experiments. Above this threshold, further increasing the crossflow velocity does not improve flux [161], and also therefore has little impact on particle deposition.

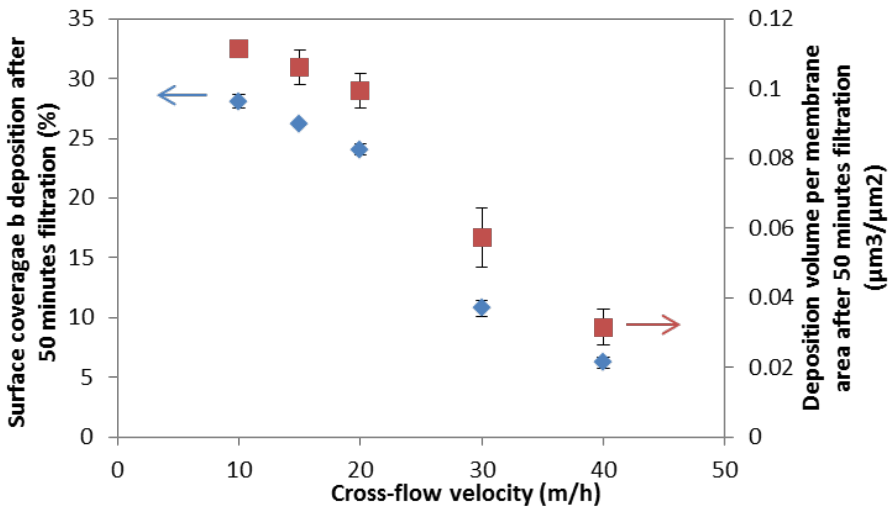

Figure 6-6 Surface coverage by deposition (blue diamond symbols) and volume of deposition per membrane area (red square symbols) after 50 minutes filtration as a function of crossflow velocity. The permeate flux is 25L/h/m^2.

The normalised deposition volume (cumulative volume of deposition normalised by the cumulative volume of solute towards the membrane) as a function of filtration time and crossflow velocity is presented in Figure 6-7. At 10 minutes of filtration, the cumulative deposition rate was highly affected by crossflow velocity, with the highest and lowest values occurring at crossflow velocity of 10 m/h and 40 m/h, respectively. While for long term filtration, the influence of crossflow velocity became less significant.

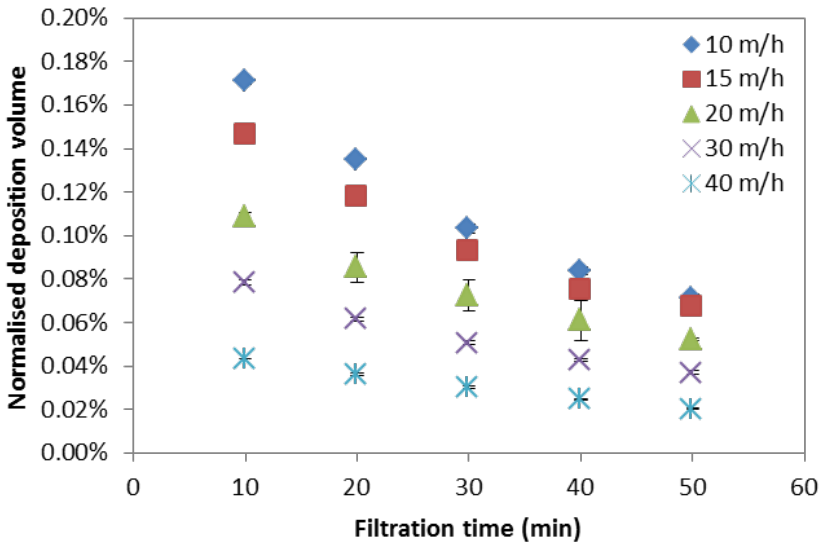

Figure 6-7 Normalised deposition volume (cumulative volume of deposition normalised by cumulative volume of solute towards the membrane) as a function of filtration time and crossflow velocity. The permeate flux is 25L/h/m^2.

6.4.3 Correlation for all conditions

As discussed in the previous sections, deposition behaviours of latex particles during crossflow filtration process are highly dependent on hydrodynamic conditions. Varying the permeate flux and crossflow velocity will change the deposition probability of particles by varying hydrodynamic forces acting on particles. In spite of hydrodynamic conditions, varying solution conditions such as pH and ionic strength also affects the deposition process by varying the interactions of membrane-particle and particle-particle [71]. Developing correlations for predicting the deposition behaviour is important for the design and setup of membrane filtration parameters. To our best knowledge, such correlations considering both hydrodynamic and solution factors have yet been reported in the literature.

On the basis of the obtained experimental results and analysis from this chapter and chapter 5, an empirical correlation (equation 6-16) for predicting particle deposition was developed. Here the overall effect of hydrodynamic conditions and solution conditions is correlated to the deposition volume per membrane area as a function of deposition probability, interaction energies and filtration time as follows:

$$\frac{Vol^*}{\phi_0 r_P} = k_1 \left(\frac{V_{m-p} - V_{p-p}}{V_{p-p}}\right)^{k_2} \gamma^{k_3} \left(\frac{t}{t_\infty}\right)^{k_4} \tag{6-16}$$

where *Vol** stands for the volume of deposition per membrane area (m^3/m^2); ϕ_0 is the volume fraction of particles in the feed; r_P is the radius of particles; V_{m-p} and V_{p-p} are the membrane-particle and particle-particle interaction energies, respectively (J) (see Chapter 4); γ is the deposition probability due to hydrodynamic forces (calculated from Equation 6-15); t is the filtration time (s) and t_∞ is the filtration time when deposition reaches the plateau state (s); k_1, k_2, k_3, and k_4 are dimensionless regressed parameters.

Using Equation 6-16, the calculated deposition volumes per membrane area are similar to the values obtained from the experimental data. The constants k_1 to k_4 in Equation 6-16 for all experimental data were regressed, and the results are presented in Table 6-1. The comparison of theoretical predictions and experimental data is shown in Figure 6-8. The deposition volume during crossflow filtration of latex particles in this study can be predicted with an overall average absolute relative deviation (AARD) of 31% for all hydrodynamic and solution conditions.

Table 6-1. Regressed Parameters in Equation 6- 16

k_1	k_2	k_3	k_4	AARD(%)
1.752	0.973	1.068	0.501	31.10

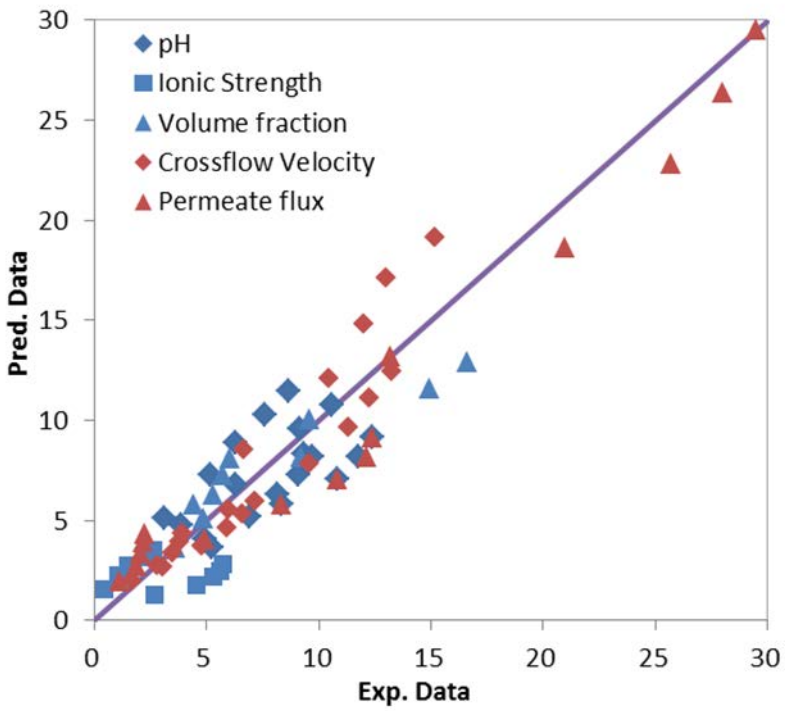

Figure 6-8 Comparison of the experimental data with the predictions using Equation 6-16. Blue symbols stands for solution conditions (pH, ionic strength, and volume fraction), and red symbols stands for hydrodynamic conditions (crossflow velocity and permeate flux). The overall average absolute relative deviation (AARD) is 31.10%.

6.5 Conclusions

The effects of operating conditions (permeate flux and cross flow velocity) on particle deposition during cross-flow ultrafiltration was investigated. A microfluidic filtration system was used to operate filtration processes at constant permeate flux and characterise particle deposition by direct visualisation. The permeate flux was found to significantly influence the deposition process. As permeate flux increased, the amount of deposition increased and the deposit layer was found to be denser and thicker. A critical crossflow velocity was observed when characterising the area fraction of membrane surface occupied by deposited particles. The amount of deposition on the membrane surface was barely affected when the crossflow velocity was lower than an apparent critical value, while it was reduced significantly as the crossflow velocity increased above this critical value. However, the total volume of deposition kept decreasing as the crossflow velocity

increased. This indicates that lower crossflow velocities can only sweep away the particles deposited in the outer layer, while higher velocities can help sweep away the deposited particles on the membrane surface as well as the outer deposit layer.

An empirical correlation has been developed for describing the volume of deposition per membrane area as a function of deposition probability, interaction energies and filtration time over a wide range of operating conditions and solution conditions. There was good agreement between the correlation predictions and actual experimental results with an average deviation (AARD) of 30%. The developed correlation for the first time offers the ability to predict the dynamic time-dependent deposition behaviours considering the overall effect of hydrodynamic and solution factors. This capability will be important for the design of membrane filtration process and will provide new accesses for understanding the mechanisms of membrane fouling.

Chapter 7 Conclusions and Future Perspectives

7.1 Conclusions

The research presented in this thesis is an interdisciplinary project incorporating membrane filtration, microfluidics and confocal microscopy system aimed to understanding the fundamental mechanism of membrane fouling. It has been found that the overall particle deposition behaviour during membrane filtration is governed by the interactions of membrane-particle and particle-particle, as well as the hydrodynamic forces exerted on particles. The fundamental interactions are influenced by solution properties, while the hydrodynamic forces are determined by the operating/flow conditions. The initial deposition behaviour is found to be significantly affected by membrane-particle interaction. However, the long-term deposition is mainly governed by particle-particle interactions.

Chapter 2 reviews the sate-of-art microstructural measurements of membrane fouling, and categorized these measurements by their capabilities. The limitations of current measurements were identified that established the increased capabilities and potential new applications of the new microfluidic system developed in **Chapter 3**, which offered ability to visualize the deposition process of 0.4 μm model particles on commercial membranes in high resolution and in real time. 3D views of the deposit layer can be obtained. **Chapter 4** determined the interaction energies of membrane-particle and particle-particle over a range of pH and ionic strength. The membrane-particle interaction energy has been for the first time reported by involving the modified Hogg-Healy-Fuersteneau (HHF) formula in the calculation, which is essential to the understanding of the fouling mechanisms.

The microstructural difference of the deposit layers formed on the membrane over a range of solution properties (**Chapter 5**) and operating conditions (**Chapter 6**) have been highlighted by direct visualizations and the dynamic deposition behaviours characterized by surface coverage, deposition volume and normalised deposition volume. From the obtained experimental results, both of membrane-particle and particle-particle interactions mainly varied with pH and ionic strength are essential for the overall deposition process. It can be concluded that membrane-

particle interaction influences short-term deposition while particle-particle has more impact on long-term deposition. In addition, the mechanisms of operating conditions influencing on the deposition process can be seen as varying hydrodynamic forces acting on particles in the feed flow characterized by the deposition probability.

An empirical correlation was developed in **Chapter 6**, which for the first time offers the ability to predict dynamic deposition behaviours considering the overall effects of solution properties (interactions) and operating conditions (hydrodynamics) on membrane fouling. Theoretical predictions have shown good agreement with obtained experimental results.

7.2 Future perspectives

Firstly, further investigations can build on this work using the novel experimental set up that was developed. This system could be used to provide more detailed examinations of other influencing factors, including particle properties such as particle size and type, and membrane properties such as pore size, surface chemistry, and morphology. In addition, membrane fouling studies under other filtration modes, such as dead-end filtration or filtration under constant pressure can also be studied in high detail using this system.

Secondly, a large number of experimental data describing the time-dependent deposition behaviours (direct images, surface coverage, and deposition volume) over a wide range of conditions have been acquired from this work. These experimental results can be further used in the validation and development of theoretical models or computational fluid dynamics models.

Further, the developed microfluidic system has successfully demonstrated its capability in examining membrane fouling from a microscopic view. The system can be modified to be employed in a range of other research fields and application, in which real-time monitoring, detailed microstructural characterisations, and direct measurements of particle-particle, particle-surface, and particle-solution interactions are important.

Reference

[1] L.J. Zeman, A.L. Zydney, Microfiltration and ultrafiltration: principles and applications, M. Dekker, 1996.
[2] A.Y. Tamime, Membrane processing: dairy and beverage applications, John Wiley & Sons, 2012.
[3] M.A. Shannon, P.W. Bohn, M. Elimelech, J.G. Georgiadis, B.J. Marinas, A.M. Mayes, Science and technology for water purification in the coming decades, Nature, 452 (2008) 301-310.
[4] G.M. Geise, H.S. Lee, D.J. Miller, B.D. Freeman, J.E. McGrath, D.R. Paul, Water purification by membranes: the role of polymer science, J. Polym. Sci., Part B: Polym. Phys., 48 (2010) 1685-1718.
[5] Y. Han, Z. Xu, C. Gao, Ultrathin graphene nanofiltration membrane for water purification, Adv. Funct. Mater., 23 (2013) 3693-3700.
[6] L. Van Dijk, G. Roncken, Membrane bioreactors for wastewater treatment: the state of the art and new developments, Water Sci. Technol., 35 (1997) 35-41.
[7] P.C. Vandevivere, R. Bianchi, W. Verstraete, Review: Treatment and reuse of wastewater from the textile wet‐processing industry: Review of emerging technologies, J. Chem. Technol. Biotechnol., 72 (1998) 289-302.
[8] B. Van der Bruggen, C. Vandecasteele, T. Van Gestel, W. Doyen, R. Leysen, A review of pressure‐driven membrane processes in wastewater treatment and drinking water production, Environ. Prog., 22 (2003) 46-56.
[9] B. Girard, L. Fukumoto, S. Sefa Koseoglu, Membrane processing of fruit juices and beverages: a review, Crit. Rev. Biotechnol., 20 (2000) 109-175.
[10] Y. Kourkoutas, A. Bekatorou, I.M. Banat, R. Marchant, A. Koutinas, Immobilization technologies and support materials suitable in alcohol beverages production: a review, Food Microbiol., 21 (2004) 377-397.
[11] A.K. Pabby, S.S. Rizvi, A.M.S. Requena, Handbook of membrane separations: chemical, pharmaceutical, food, and biotechnological applications, CRC press, 2015.
[12] K. Scott, R. Hughes, Industrial membrane separation technology, Springer Science & Business Media, 2012.
[13] A.W. Mohammad, C.Y. Ng, Y.P. Lim, G.H. Ng, Ultrafiltration in food processing industry: review on application, membrane fouling, and fouling control, Food and bioprocess technology, 5 (2012) 1143-1156.
[14] G. Daufin, J.-P. Escudier, H. Carrere, S. Berot, L. Fillaudeau, M. Decloux, Recent and emerging applications of membrane processes in the food and dairy industry, Food Bioprod. Process., 79 (2001) 89-102.
[15] R.W. Baker, Membrane technology and applications, John Wiley & Sons, Ltd, (2004) 96-103.
[16] F. Vaillant, P. Millan, G. O'Brien, M. Dornier, M. Decloux, M. Reynes, Crossflow microfiltration of passion fruit juice after partial enzymatic liquefaction, J. Food Eng., 42 (1999) 215-224.
[17] S.E. Walsh, S.P. Denyer, Filtration sterilization, Wiley Online Library, 2012.
[18] E. Renner, M. Abd-El-Salam, Application of ultrafiltration in the dairy industry, Elsevier Science Publishers Ltd., 1991.
[19] J. Radjenović, M. Petrović, F. Ventura, D. Barceló, Rejection of pharmaceuticals in nanofiltration and reverse osmosis membrane drinking water treatment, Water Res., 42 (2008) 3601-3610.
[20] J. Wei, C. Qiu, C.Y. Tang, R. Wang, A.G. Fane, Synthesis and characterization of flat-sheet thin film composite forward osmosis membranes, J. Membr. Sci., 372 (2011) 292-302.
[21] V. Gekas, Terminology for pressure-driven membrane operations, Desalination, 68 (1988) 77-92.

[22] A. Marshall, P. Munro, G. Trägårdh, The effect of protein fouling in microfiltration and ultrafiltration on permeate flux, protein retention and selectivity: a literature review, Desalination, 91 (1993) 65-108.
[23] L. Song, Flux decline in crossflow microfiltration and ultrafiltration: mechanisms and modeling of membrane fouling, J. Membr. Sci., 139 (1998) 183-200.
[24] W. Guo, H.-H. Ngo, J. Li, A mini-review on membrane fouling, Bioresour. Technol., 122 (2012) 27-34.
[25] A.S. Michaels, New separation technique for CPI, Chem. Eng. Prog., 64 (1968) 31-&.
[26] W.F. Blatt, A. Dravid, A.S. Michaels, L. Nelsen, Solute polarization and cake formation in membrane ultrafiltration: causes, consequences and control techniques, Membrane science and technology, 47 (1970).
[27] M.C. Porter, Concentration polarization with membrane ultrafiltration, Industrial & Engineering Chemistry Product Research and Development, 11 (1972) 234-248.
[28] L. Andrés, A. Pérez, A. Álvarez, J. Coca, Polarización de concentración en los procesos con membranas:(y III) aplicación a la electrodiálisis, Ingeniería química, (1992) 241-245.
[29] M. Elimelech, S. Bhattacharjee, A novel approach for modeling concentration polarization in crossflow membrane filtration based on the equivalence of osmotic pressure model and filtration theory, J. Membr. Sci., 145 (1998) 223-241.
[30] S.-W. Choi, J.-Y. Yoon, S. Haam, J.-K. Jung, J.-H. Kim, W.-S. Kim, Modeling of the permeate flux during microfiltration of BSA-adsorbed microspheres in a stirred cell, J. Colloid Interface Sci., 228 (2000) 270-278.
[31] J. De Bruijn, F. Salazar, R. Borquez, Membrane blocking in ultrafiltration: a new approach to fouling, Food Bioprod. Process., 83 (2005) 211-219.
[32] J. Hermia, Constant pressure blocking filtration law application to powder-law non-Newtonian fluid, Trans. Inst. Chem. Eng., 60 (1982) 183-187.
[33] C.-C. Ho, A.L. Zydney, A combined pore blockage and cake filtration model for protein fouling during microfiltration, J. Colloid Interface Sci., 232 (2000) 389-399.
[34] P. Hermans, Principles of the mathematical treatment of constant-pressure filtration, J. Soc. Chem. Ind., 55 (1936) 1-4.
[35] W. Bowen, J. Calvo, A. Hernandez, Steps of membrane blocking in flux decline during protein microfiltration, J. Membr. Sci., 101 (1995) 153-165.
[36] A. Affandy, E. Keshavarz-Moore, H.K. Versteeg, Application of filtration blocking models to describe fouling and transmission of large plasmids DNA in sterile filtration, J. Membr. Sci., 437 (2013) 150-159.
[37] A. Fane, C. Fell, A. Suki, The effect of pH and ionic environment on the ultrafiltration of protein solutions with retentive membranes, J. Membr. Sci., 16 (1983) 195-210.
[38] Y. Li, J. Lee, J. Lal, L. An, Q. Huang, Effects of pH on the interactions and conformation of bovine serum albumin: comparison between chemical force microscopy and small-angle neutron scattering, The Journal of Physical Chemistry B, 112 (2008) 3797-3806.
[39] R. Chan, V. Chen, The effects of electrolyte concentration and pH on protein aggregation and deposition: critical flux and constant flux membrane filtration, J. Membr. Sci., 185 (2001) 177-192.
[40] Y.P. Lim, A.W. Mohammad, Influence of pH and ionic strength during food protein ultrafiltration: elucidation of permeate flux behavior, fouling resistance, and mechanism, Sep. Sci. Technol., 47 (2012) 446-454.
[41] H. Mo, K.G. Tay, H.Y. Ng, Fouling of reverse osmosis membrane by protein (BSA): effects of pH, calcium, magnesium, ionic strength and temperature, J. Membr. Sci., 315 (2008) 28-35.
[42] Q. She, C.Y. Tang, Y.-N. Wang, Z. Zhang, The role of hydrodynamic conditions and solution chemistry on protein fouling during ultrafiltration, Desalination, 249 (2009) 1079-1087.
[43] C.Y. Tang, J.O. Leckie, Membrane independent limiting flux for RO and NF membranes fouled by humic acid, Environ. Sci. Technol., 41 (2007) 4767-4773.

[44] S.T. Kelly, A.L. Zydney, Mechanisms for BSA fouling during microfiltration, J. Membr. Sci., 107 (1995) 115-127.
[45] I.H. Huisman, P. Prádanos, A. Hernández, The effect of protein–protein and protein–membrane interactions on membrane fouling in ultrafiltration, J. Membr. Sci., 179 (2000) 79-90.
[46] Y.-N. Wang, C.Y. Tang, Protein fouling of nanofiltration, reverse osmosis, and ultrafiltration membranes—the role of hydrodynamic conditions, solution chemistry, and membrane properties, J. Membr. Sci., 376 (2011) 275-282.
[47] S.P. Palecek, A.L. Zydney, Hydraulic permeability of protein deposits formed during microfiltration: effect of solution pH and ionic strength, J. Membr. Sci., 95 (1994) 71-81.
[48] S. Salgın, Effects of Ionic Environments on Bovine Serum Albumin Fouling in a Cross - Flow Ultrafiltration System, Chemical engineering & technology, 30 (2007) 255-260.
[49] R.D. Cohen, R. Probstein, Colloidal fouling of reverse osmosis membranes, J. Colloid Interface Sci., 114 (1986) 194-207.
[50] R. Baker, A. Fane, C. Fell, B. Yoo, Factors affecting flux in crossflow filtration, Desalination, 53 (1985) 81-93.
[51] W.R. Bowen, Q. Gan, Properties of microfiltration membranes: flux loss during constant pressure permeation of bovine serum albumin, Biotechnol. Bioeng., 38 (1991) 688-696.
[52] R. Van Reis, A. Zydney, Membrane separations in biotechnology, Curr. Opin. Biotechnol., 12 (2001) 208-211.
[53] R.W. Baker, Membrane technology and applications, in, Wiley Chichester, 2004.
[54] J. Decarolis, S. Hong, J. Taylor, Fouling behavior of a pilot scale inside-out hollow fiber UF membrane during dead-end filtration of tertiary wastewater, J. Membr. Sci., 191 (2001) 165-178.
[55] S. Chang, A. Fane, T. Waite, Analysis of constant permeate flow filtration using dead-end hollow fiber membranes, J. Membr. Sci., 268 (2006) 132-141.
[56] W. Van de Ven, K. van't Sant, I. Pünt, A. Zwijnenburg, A. Kemperman, W. Van der Meer, M. Wessling, Hollow fiber dead-end ultrafiltration: Influence of ionic environment on filtration of alginates, J. Membr. Sci., 308 (2008) 218-229.
[57] G. Belfort, R.H. Davis, A.L. Zydney, The behavior of suspensions and macromolecular solutions in crossflow microfiltration, J. Membr. Sci., 96 (1994) 1-58.
[58] A.B. Koltuniewicz, R. Field, T. Arnot, Cross-flow and dead-end microfiltration of oily-water emulsion. Part I: Experimental study and analysis of flux decline, J. Membr. Sci., 102 (1995) 193-207.
[59] B. Tansel, J. Sager, T. Rector, J. Garland, R.F. Strayer, L. Levine, M. Roberts, M. Hummerick, J. Bauer, Significance of hydrated radius and hydration shells on ionic permeability during nanofiltration in dead end and cross flow modes, Sep. Purif. Technol., 51 (2006) 40-47.
[60] D.J. Miller, S. Kasemset, L. Wang, D.R. Paul, B.D. Freeman, Constant flux crossflow filtration evaluation of surface-modified fouling-resistant membranes, J. Membr. Sci., 452 (2014) 171-183.
[61] P. Gatenholm, C. Fell, A. Fane, Influence of the membrane structure on the composition of the deposit-layer during processing of microbial suspensions, Desalination, 70 (1988) 363-378.
[62] Y.-J. Zhao, K.-F. Wu, Z.-J. Wang, L. Zhao, S.-s. Li, Fouling and cleaning of membrane-a literature review, JOURNAL OF ENVIRONMENTAL SCIENCES-BEIJING-, 12 (2000) 241-251.
[63] A. Saxena, B.P. Tripathi, M. Kumar, V.K. Shahi, Membrane-based techniques for the separation and purification of proteins: an overview, Adv. Colloid Interface Sci., 145 (2009) 1-22.
[64] Q. Li, Z. Xu, I. Pinnau, Fouling of reverse osmosis membranes by biopolymers in wastewater secondary effluent: Role of membrane surface properties and initial permeate flux, J. Membr. Sci., 290 (2007) 173-181.
[65] S. Atchariyawut, C. Feng, R. Wang, R. Jiraratananon, D. Liang, Effect of membrane structure on mass-transfer in the membrane gas–liquid contacting process using microporous PVDF hollow fibers, J. Membr. Sci., 285 (2006) 272-281.

[66] P. van der Marel, A. Zwijnenburg, A. Kemperman, M. Wessling, H. Temmink, W. van der Meer, Influence of membrane properties on fouling in submerged membrane bioreactors, J. Membr. Sci., 348 (2010) 66-74.
[67] E.M. Vrijenhoek, S. Hong, M. Elimelech, Influence of membrane surface properties on initial rate of colloidal fouling of reverse osmosis and nanofiltration membranes, J. Membr. Sci., 188 (2001) 115-128.
[68] H. Deng, Z. Wang, W. Zhang, B. Hu, S. Zhang, Preparation and monovalent selective properties of multilayer polyelectrolyte modified cation - exchange membranes, J. Appl. Polym. Sci., 132 (2015).
[69] H. Deng, S. Zhao, Q. Meng, W. Zhang, B. Hu, A novel surface ion-imprinted cation-exchange membrane for selective separation of copper ion, Industrial & Engineering Chemistry Research, 53 (2014) 15230-15236.
[70] Y. Zhang, J. Sunarso, S. Liu, R. Wang, Current status and development of membranes for CO 2/CH 4 separation: a review, International Journal of Greenhouse Gas Control, 12 (2013) 84-107.
[71] H. Di, G.J. Martin, D.E. Dunstan, A microfluidic system for studying particle deposition during ultrafiltration, J. Membr. Sci., 532 (2017) 68-75.
[72] M.-S. Chun, G.-Y. Chung, J.-J. Kim, On the behavior of the electrostatic colloidal interaction in the membrane filtration of latex suspensions, J. Membr. Sci., 193 (2001) 97-109.
[73] G. Gesan-Guiziou, R. Wakeman, G. Daufin, Stability of latex crossflow filtration: cake properties and critical conditions of deposition, Chem. Eng. J., 85 (2002) 27-34.
[74] Y. Marselina, P. Le-Clech, R.M. Stuetz, V. Chen, Characterisation of membrane fouling deposition and removal by direct observation technique, J. Membr. Sci., 341 (2009) 163-171.
[75] Y. Marselina, P. Le-Clech, R. Stuetz, V. Chen, Detailed characterisation of fouling deposition and removal on a hollow fibre membrane by direct observation technique, Desalination, 231 (2008) 3-11.
[76] H. Li, A. Fane, H. Coster, S. Vigneswaran, Direct observation of particle deposition on the membrane surface during crossflow microfiltration, J. Membr. Sci., 149 (1998) 83-97.
[77] W.D. Mores, R.H. Davis, Direct visual observation of yeast deposition and removal during microfiltration, J. Membr. Sci., 189 (2001) 217-230.
[78] M. Ferrando, A. Rŏżek, M. Zator, F. Lopez, C. Güell, An approach to membrane fouling characterization by confocal scanning laser microscopy, J. Membr. Sci., 250 (2005) 283-293.
[79] J. Linkhorst, T. Beckmann, D. Go, A.J. Kuehne, M. Wessling, Microfluidic colloid filtration, Scientific reports, 6 (2016).
[80] H.M. Wyss, D.L. Blair, J.F. Morris, H.A. Stone, D.A. Weitz, Mechanism for clogging of microchannels, Physical review E, 74 (2006) 061402.
[81] P. Bacchin, A. Marty, P. Duru, M. Meireles, P. Aimar, Colloidal surface interactions and membrane fouling: investigations at pore scale, Adv. Colloid Interface Sci., 164 (2011) 2-11.
[82] S.S. Massenburg, E. Amstad, D.A. Weitz, Clogging in parallelized tapered microfluidic channels, Microfluid. Nanofluid., 20 (2016) 1-5.
[83] I.S. Ngene, R.G. Lammertink, M. Wessling, W.G. Van der Meer, Visual characterization of fouling with bidisperse solution, J. Membr. Sci., 368 (2011) 110-115.
[84] I.S. Ngene, R.G. Lammertink, M. Wessling, W. van der Meer, A microfluidic membrane chip for in situ fouling characterization, J. Membr. Sci., 346 (2010) 202-207.
[85] J. De Jong, R. Lammertink, M. Wessling, Membranes and microfluidics: a review, Lab on a Chip, 6 (2006) 1125-1139.
[86] J.C. Chen, Q. Li, M. Elimelech, In situ monitoring techniques for concentration polarization and fouling phenomena in membrane filtration, Adv. Colloid Interface Sci., 107 (2004) 83-108.
[87] V. Chen, H. Li, A. Fane, Non-invasive observation of synthetic membrane processes–a review of methods, J. Membr. Sci., 241 (2004) 23-44.
[88] V. Vilker, C. Colton, K. Smith, Concentration polarization in protein ultrafiltration, AIChE J., 27 (1981) 632-645.

[89] C.R. Ethier, D.C. Lin, Refractometric measurement of polarized layer structure: studies of hyaluronic acid ultrafiltration, J. Membr. Sci., 68 (1992) 249-261.
[90] L.M. Gowman, C.R. Ethier, Concentration and concentration gradient measurements in an ultrafiltration concentration polarization layer Part I: A laser-based refractometric experimental technique, J. Membr. Sci., 131 (1997) 95-105.
[91] L.M. Gowman, C.R. Ethier, Concentration and concentration gradient measurements in an ultrafiltration concentration polarization layer Part II: Application to hyaluronan, J. Membr. Sci., 131 (1997) 107-123.
[92] R. Mc Donogh, H. Bauser, N. Stroh, U. Grauschopf, Experimental in situ measurement of concentration polarisation during ultra-and micro-filtration of bovine serum albumin and Dextran Blue solutions, J. Membr. Sci., 104 (1995) 51-63.
[93] R. McDonogh, H. Bauser, N. Stroh, H. Chmiel, Separation efficiency of membranes in biotechnology: an experimental and mathematical study of flux control, Chem. Eng. Sci., 47 (1992) 271-279.
[94] J. Fernández-Sempere, F. Ruiz-Beviá, R. Salcedo-Dıaz, Measurements by holographic interferometry of concentration profiles in dead-end ultrafiltration of polyethylene glycol solutions, J. Membr. Sci., 229 (2004) 187-197.
[95] M.J. Fernandez-Torres, F. Ruiz-Bevia, J. Fernandez-Sempere, M. Lopez-Leiva, Visualization of the UF polarized layer by holographic interferometry, American Institute of Chemical Engineers. AIChE Journal, 44 (1998) 1765.
[96] J. Fernández-Sempere, F. Ruiz-Beviá, R. Salcedo-Díaz, P. García-Algado, Diffusion studies in polarized reverse osmosis processes by holographic interferometry, Optics and Lasers in Engineering, 46 (2008) 877-887.
[97] J. Fernández-Sempere, F. Ruiz-Beviá, P. García-Algado, R. Salcedo-Díaz, Visualization and modelling of the polarization layer and a reversible adsorption process in PEG-10000 dead-end ultrafiltration, J. Membr. Sci., 342 (2009) 279-290.
[98] J. Fernández-Sempere, F. Ruiz-Beviá, P. García-Algado, R. Salcedo-Díaz, Experimental study of concentration polarization in a crossflow reverse osmosis system using Digital Holographic Interferometry, Desalination, 257 (2010) 36-45.
[99] J. Fernández-Sempere, F. Ruiz-Beviá, R. Salcedo-Díaz, P. García-Algado, M. García-Rodríguez, Digital holographic interferometry visualization of PEG-10000 accumulation on an acetate cellulose membrane: assessment of polarization layer and adsorption phenomenon, Desalination and Water Treatment, 42 (2012) 49-56.
[100] C. David, F. Pignon, T. Narayanan, M. Sztucki, G. Gésan-Guiziou, A. Magnin, Spatial and temporal in situ evolution of the concentration profile during casein micelle ultrafiltration probed by small-angle X-ray scattering, Langmuir, 24 (2008) 4523-4529.
[101] F. Pignon, M. Abyan, C. David, A. Magnin, M. Sztucki, In situ characterization by SAXS of concentration polarization layers during cross-flow ultrafiltration of laponite dispersions, Langmuir, 28 (2011) 1083-1094.
[102] Y. Jin, N. Hengl, S. Baup, F. Pignon, N. Gondrexon, A. Magnin, M. Sztucki, T. Narayanan, L. Michot, B. Cabane, Effects of ultrasound on colloidal organization at nanometer length scale during cross-flow ultrafiltration probed by in-situ SAXS, J. Membr. Sci., 453 (2014) 624-635.
[103] Y. Jin, N. Hengl, S. Baup, F. Pignon, N. Gondrexon, M. Sztucki, G. Gésan-Guiziou, A. Magnin, M. Abyan, M. Karrouch, Effects of ultrasound on cross-flow ultrafiltration of skim milk: Characterization from macro-scale to nano-scale, J. Membr. Sci., 470 (2014) 205-218.
[104] G.S. Settles, Schlieren and shadowgraph techniques: visualizing phenomena in transparent media, Springer Science & Business Media, 2012.
[105] A. Bouchoux, P. Qu, P. Bacchin, G.v. Gésan-Guiziou, A general approach for predicting the filtration of soft and permeable colloids: the milk example, Langmuir, 30 (2013) 22-34.

[106] S. Yao, A. Fane, J. Pope, An investigation of the fluidity of concentration polarisation layers in crossflow membrane filtration of an oil-water emulsion using chemical shift selective flow imaging, Magn. Reson. Imaging, 15 (1997) 235-242.
[107] S. Yao, M. Costello, A. Fane, J. Pope, Non-invasive observation of flow profiles and polarisation layers in hollow fibre membrane filtration modules using NMR micro-imaging, J. Membr. Sci., 99 (1995) 207-216.
[108] J. Pope, S. Yao, A. Fane, Quantitative measurements of the concentration polarisation layer thickness in membrane filtration of oil-water emulsions using NMR micro-imaging, J. Membr. Sci., 118 (1996) 247-257.
[109] D. Airey, S. Yao, J. Wu, V. Chen, A. Fane, J. Pope, An investigation of concentration polarization phenomena in membrane filtration of colloidal silica suspensions by NMR micro-imaging, J. Membr. Sci., 145 (1998) 145-158.
[110] J. Altmann, S. Ripperger, Particle deposition and layer formation at the crossflow microfiltration, J. Membr. Sci., 124 (1997) 119-128.
[111] J. Mendret, C. Guigui, P. Schmitz, C. Cabassud, P. Duru, An optical method for in situ characterization of fouling during filtration, AlChE J., 53 (2007) 2265-2274.
[112] M. Hamachi, M. Mietton-Peuchot, Experimental investigations of cake characteristics in crossflow microfiltration, Chem. Eng. Sci., 54 (1999) 4023-4030.
[113] K.-L. Tung, S. Wang, W.-M. Lu, C.-H. Pan, In situ measurement of cake thickness distribution by a photointerrupt sensor, J. Membr. Sci., 190 (2001) 57-67.
[114] J. Li, D. Hallbauer, R. Sanderson, Direct monitoring of membrane fouling and cleaning during ultrafiltration using a non-invasive ultrasonic technique, J. Membr. Sci., 215 (2003) 33-52.
[115] J. Li, R. Sanderson, In situ measurement of particle deposition and its removal in microfiltration by ultrasonic time-domain reflectometry, Desalination, 146 (2002) 169-175.
[116] J. Li, R. Sanderson, G. Chai, D. Hallbauer, Development of an ultrasonic technique for in situ investigating the properties of deposited protein during crossflow ultrafiltration, J. Colloid Interface Sci., 284 (2005) 228-238.
[117] J. Li, R. Sanderson, D. Hallbauer, V. Hallbauer-Zadorozhnaya, Measurement and modelling of organic fouling deposition in ultrafiltration by ultrasonic transfer signals and reflections, Desalination, 146 (2002) 177-185.
[118] C.A. Romero, R.H. Davis, Experimental verification of the shear-induced hydrodynamic diffusion model of crossflow microfiltration, J. Membr. Sci., 62 (1991) 249-273.
[119] M. Mackley, N. Sherman, Cross-flow cake filtration mechanisms and kinetics, Chem. Eng. Sci., 47 (1992) 3067-3084.
[120] R. Wakeman, Visualization of cake formation in cross-flow microfiltration, Chemical engineering research & design, 72 (1994) 530-540.
[121] R.R. Ernst, G. Bodenhausen, A. Wokaun, Principles of nuclear magnetic resonance in one and two dimensions, Clarendon Press Oxford, 1987.
[122] Z.-P. Liang, P.C. Lauterbur, Principles of magnetic resonance imaging, SPIE Optical Engineering Press, 2000.
[123] S.W. Young, Nuclear magnetic resonance imaging: basic principles, (1985).
[124] A.P. Mairal, A.R. Greenberg, W.B. Krantz, L.J. Bond, Real-time measurement of inorganic fouling of RO desalination membranes using ultrasonic time-domain reflectometry, J. Membr. Sci., 159 (1999) 185-196.
[125] V.E. Reinsch, A.R. Greenberg, S.S. Kelley, R. Peterson, L.J. Bond, A new technique for the simultaneous, real-time measurement of membrane compaction and performance during exposure to high-pressure gas, J. Membr. Sci., 171 (2000) 217-228.
[126] H. Li, A. Fane, H. Coster, S. Vigneswaran, An assessment of depolarisation models of crossflow microfiltration by direct observation through the membrane, J. Membr. Sci., 172 (2000) 135-147.

[127] H. Li, A. Fane, H. Coster, S. Vigneswaran, Observation of deposition and removal behaviour of submicron bacteria on the membrane surface during crossflow microfiltration, J. Membr. Sci., 217 (2003) 29-41.
[128] C. Charcosset, A. Cherfi, J.-C. Bernengo, Characterization of microporous membrane morphology using confocal scanning laser microscopy, Chem. Eng. Sci., 55 (2000) 5351-5358.
[129] C. Sun, L. Fiksdal, A. Hanssen-Bauer, M.B. Rye, T. Leiknes, Characterization of membrane biofouling at different operating conditions (flux) in drinking water treatment using confocal laser scanning microscopy (CLSM) and image analysis, J. Membr. Sci., 382 (2011) 194-201.
[130] S. West, H. Horn, W. Hijnen, C. Castillo, M. Wagner, Confocal laser scanning microscopy as a tool to validate the efficiency of membrane cleaning procedures to remove biofilms, Sep. Purif. Technol., 122 (2014) 402-411.
[131] B. Yuan, X. Wang, C. Tang, X. Li, G. Yu, In situ observation of the growth of biofouling layer in osmotic membrane bioreactors by multiple fluorescence labeling and confocal laser scanning microscopy, Water Res., 75 (2015) 188-200.
[132] G. Brans, A. van Dinther, B. Odum, C. Schroën, R. Boom, Transmission and fractionation of micro-sized particle suspensions, J. Membr. Sci., 290 (2007) 230-240.
[133] T. Van De Laar, S. Ten Klooster, K. Schroën, J. Sprakel, Transition-state theory predicts clogging at the microscale, Scientific Reports, 6 (2016).
[134] P. Hodgson, V. Pillay, A. Fane, Visual study of crossflow microfiltration with inorganic membranes: resistance of biomass and particulate cake, in: Proceedings of the Sixth World Filtration Congress, Nagoya, 1993, pp. 607-610.
[135] C.Y. Tang, Y.-N. Kwon, J.O. Leckie, Fouling of reverse osmosis and nanofiltration membranes by humic acid—effects of solution composition and hydrodynamic conditions, J. Membr. Sci., 290 (2007) 86-94.
[136] S.P. Palecek, A.L. Zydney, Intermolecular electrostatic interactions and their effect on flux and protein deposition during protein filtration, Biotechnol. Progr., 10 (1994) 207-213.
[137] S. Hong, M. Elimelech, Chemical and physical aspects of natural organic matter (NOM) fouling of nanofiltration membranes, J. Membr. Sci., 132 (1997) 159-181.
[138] M. Goosen, S. Sablani, H. Al‐Hinai, S. Al‐Obeidani, R. Al‐Belushi, D. Jackson, Fouling of reverse osmosis and ultrafiltration membranes: a critical review, Sep. Sci. Technol., 39 (2005) 2261-2297.
[139] A. Seidel, M. Elimelech, Coupling between chemical and physical interactions in natural organic matter (NOM) fouling of nanofiltration membranes: implications for fouling control, J. Membr. Sci., 203 (2002) 245-255.
[140] W.S. Ang, M. Elimelech, Protein (BSA) fouling of reverse osmosis membranes: implications for wastewater reclamation, J. Membr. Sci., 296 (2007) 83-92.
[141] P. Heinemann, J. Howell, R. Bryan, Microfiltration of protein solutions: effect of fouling on rejection, Desalination, 68 (1988) 243-250.
[142] X. Zhu, M. Elimelech, Colloidal fouling of reverse osmosis membranes: measurements and fouling mechanisms, Environ. Sci. Technol., 31 (1997) 3654-3662.
[143] C.Y. Tang, Y.-N. Kwon, J.O. Leckie, The role of foulant–foulant electrostatic interaction on limiting flux for RO and NF membranes during humic acid fouling—theoretical basis, experimental evidence, and AFM interaction force measurement, J. Membr. Sci., 326 (2009) 526-532.
[144] J. Schindelin, I. Arganda-Carreras, E. Frise, V. Kaynig, M. Longair, T. Pietzsch, S. Preibisch, C. Rueden, S. Saalfeld, B. Schmid, Fiji: an open-source platform for biological-image analysis, Nat. Methods, 9 (2012) 676-682.
[145] M. Pontié, X. Chasseray, D. Lemordant, J. Lainé, The streaming potential method for the characterization of ultrafiltration organic membranes and the control of cleaning treatments, J. Membr. Sci., 129 (1997) 125-133.
[146] J.N. Israelachvili, Intermolecular and surface forces, Academic press, 2011.

[147] J.E. Sader, S.L. Carnie, D.Y. Chan, Accurate analytic formulas for the double-layer interaction between spheres, J. Colloid Interface Sci., 171 (1995) 46-54.
[148] H. Hamaker, The London—van der Waals attraction between spherical particles, physica, 4 (1937) 1058-1072.
[149] S. Salgın, U. Salgın, N. Tuzlalı, Determination of correct zeta potential of polyether sulfone membranes using CLC and AGC: ionic environment effect, Desalination and Water Treatment, 57 (2016) 26031-26040.
[150] S. Salgin, U. Salgin, N. Soyer, Streaming potential measurements of polyethersulfone ultrafiltration membranes to determine salt effects on membrane zeta potential, Int. J. Electrochem. Sci, 8 (2013) 4073-4084.
[151] A. Abdelrasoul, H. Doan, A. Lohi, Fouling in membrane filtration and remediation methods, Mass transfer-advances in sustainable energy and environment oriented numerical modeling, 195 (2013).
[152] X. Yang, R. Wang, A.G. Fane, C.Y. Tang, I. Wenten, Membrane module design and dynamic shear-induced techniques to enhance liquid separation by hollow fiber modules: a review, Desalination and Water Treatment, 51 (2013) 3604-3627.
[153] W.J. Lewis, T. Mattsson, Y.J. Chew, M.R. Bird, Investigation of cake fouling and pore blocking phenomena using fluid dynamic gauging and critical flux models, J. Membr. Sci., 533 (2017) 38-47.
[154] T. Mattsson, W.J. Lewis, Y.J. Chew, M.R. Bird, In situ investigation of soft cake fouling layers using fluid dynamic gauging, Food Bioprod. Process., 93 (2015) 205-210.
[155] Q. She, R. Wang, A.G. Fane, C.Y. Tang, Membrane fouling in osmotically driven membrane processes: a review, J. Membr. Sci., 499 (2016) 201-233.
[156] H. Mo, K.G. Tay, H.Y. Ng, Fouling of reverse osmosis membrane by protein (BSA): effects of pH, calcium, magnesium, ionic strength and temperature, J. Membr. Sci., 315 (2008) 28-35.
[157] W.R. Bowen, F. Jenner, Theoretical descriptions of membrane filtration of colloids and fine particles: an assessment and review, Adv. Colloid Interface Sci., 56 (1995) 141-200.
[158] K. Stamatakis, C. Tien, A simple model of cross‐flow filtration based on particle adhesion, AIChE J., 39 (1993) 1292-1302.
[159] W.R. Bowen, H.N. Yousef, J.I. Calvo, Dynamic crossflow ultrafiltration of colloids: a deposition probability cake filtration approach, Sep. Purif. Technol., 24 (2001) 297-308.
[160] M. O'neill, A sphere in contact with a plane wall in a slow linear shear flow, Chem. Eng. Sci., 23 (1968) 1293-1298.
[161] B. Lian, Y. Wang, P. Le-Clech, V. Chen, G. Leslie, A numerical approach to module design for crossflow vacuum membrane distillation systems, J. Membr. Sci., 510 (2016) 489-496.